UNIVERSITÀ DEGLI STUDI DI TRIESTE

XXVIII CICLO DEL DOTTORATO DI RICERCA IN FISICA

Simulations and experimental assessment of dosimetric evaluations for breast imaging studies with Synchrotron Radiation

Settore scientifico-disciplinare: **FIS/07 FISICA APPLICATA**

DOTTORANDO
CHRISTIAN FEDON

COORDINATORE
PROF. PAOLO CAMERINI

SUPERVISORE DI TESI
PROF.SSA RENATA LONGO

CO-SUPERVISORE DI TESI
DR. GIULIANA TROMBA

ANNO ACCADEMICO 2014 / 2015

UNIVERSITÀ DEGLI STUDI DI TRIESTE

XXVIII Cycles - PhD School in Physics

Simulations and experimental assessment of dosimetric evaluations for breast imaging studies with Synchrotron Radiation

Candidate:
Christian FEDON

Supervisor:
Prof.ssa **Renata LONGO**
Co-Supervisor:
Dr. **Giuliana TROMBA**

Academic Year 2015-2016

Contents

Abstract

L'insorgenza di tumori è uno dei principali problemi che riguardano la salute pubblica a livello mondiale (Siegel *et al.*, 2014). In particolare nella popolazione femminile, il cancro al seno è il tumore più diffuso (Malvezzi *et al.*, 2014).
Grazie all'introduzione dei programmi di screening, a partire dalla metà degli anni '80, si è registrata una sensibile diminuzione della mortalità dovuta a carcinomi mammari (Malvezzi *et al.*, 2014).
Lo sviluppo tecnologico ha inoltre permesso al radiologo di ottenere immagini del seno non solo 2D (come sono quelle ottenute con la Mammografia Digitale, DM) ma bensì 3D: tali tecniche sono la Breast Tomosintesi (BT) (Sechopoulos (2013a) e Sechopoulos (2013b)) e la Breast Computed Tomography (BCT) (Glick, 2007). L'immagine 3D offre infatti al radiologio la possibilità di una diagnosi più accurata poichè supera in buona parte il problema della sovrapposizione dei tessuti (problema che invece rimane nelle immagini mammografiche 2D).
Per migliorare la diagnosi precoce del tumore al seno, si è svolto a Trieste (a partire dal 2006) uno studio clinico che utilizza la luce di sincrotrone come sorgente di raggi x per eseguire l'esame mammografico (Castelli and et al., 2011).
Il sincrotrone Elettra (situato sull'altopiano carsico di Basovizza, Trieste) ospita infatti una facility per l'esecuzione dell'esame mammagrafico lungo la linea di luce SYRMEP (SYnchrotron Radiation for MEdical Physics).
I risultati dello studio (basati su di un campione di 71 pazienti di età compresa tra i 41 - 82 anni) hanno evidenziato sia una riduzione delle dosi ricevute dalle pazienti (di circa il 42% rispetto all'esame ospedaliero) sia una migliore capacità diagnostica (Castelli and et al. (2011) e Longo *et al.* (2014)). Tali risultati vanno interpretati sulla base delle proprietà della luce di sincrotrone:

i grazie alla diffrazione di Bragg, il fascio di sincrotrone viene monocromatizzato eliminando tutta la componente di basse energie che invece è presente nello spettro di raggi x del tubo mammografico ospedaliero;

ii l'alta coerenza spaziale della sorgente permette di sfruttare le proprietà ondulatorie della luce, in particolare gli effetti di fase (Phase Contrast), che permettono una migliore visibilità morfologica dei bordi delle strutture interne al seno.

A partire dal 2013 è attivo il progetto SYRMA-CT (finanziato dall'Istituto Nazionale di Fisica Nucleare) che ha come principale obbiettivo quello di attuare il primo studio clinico di

Breast Computed Tomography con luce di sincrotone.
Il progetto SYRMA-CT (SYnchrotron Radiation for MAmmograpy - Computed Tomography) si inserisce nel trend globale di passaggio dalle immagini 2D a quelle 3D e ingloba al suo interno l'esperienza maturata durante la sperimentazione clinica del programma di Mammografia con la Radizione di Sincrotrone (MSR). SYRMA-CT riunisce al suo interno elementi innovativi quali l'utilizzo di un detector single photon counting (PIXIRAD (Bellazzini *et al.*, 2013)), lo stato dell'arte degli algoritmi di ricostruzione per le immagini tomografiche e prevede importanti upgrade della linea di luce per la parte di dosimetria.
Il calcolo della dose rilasciata alla paziente durante l'esame assume infatti un aspetto di fondamentale importanza: il maggiore ostacolo nella transizione della BCT nella pratica clinica è infatti la possibilità di eseguire l'esame a dosi che siano comparabili con le due proiezioni della mammografia tradizionale (i.e. 2.5 mGy per proiezione) (Kalender *et al.*, 2012).
Il calcolo della dose in BCT è ottenuto moltiplicando l'Air Kerma misurato all'isocentro (con camere ad ionizzazione) per opportuni coefficienti (DgN_{ct}, Normalized Glandular Dose) funzione dell'energia, diametro e ghiandolarità del seno.
Scopo del presente lavoro di dottorato è quello di estendere la grandezza utilizzata per il calcolo della dose in breast-CT (i.e. Mean Glandular Dose, MGD) alla particolare situazione dell'esame con luce di sincrotrone. L'esame prevede infatti una situazione di irraggiamento parziale dell'organo (da 3 cm fino ad un massimo di 5 cm) e l'utilizzo di una sorgente monocromatica.
Nel corso del lavoro di tesi è stato sviluppato un codice di simulazione Monte Carlo basato sul toolkit GEANT4 che permette di calcolare i coefficienti necessari per la stima della dose (DgN_{ct}).
Il codice è stato validato confrontandolo sia con la letteratura che con specifiche misure sperimentali (Fedon *et al.* (2015) e Mettivier *et al.* (2016)) alla linea di luce SYRMEP.
Le misure sperimentali hanno coinvolto l'utilizzo di dosimetri a termoluminescenza (TLD) (Emiro *et al.*, 2015), pellicole radiocromiche (GAF) (Di Lillo *et al.*, 2015) e camere ad ionizzazione di tipo *pencil* per il calcolo del Computed Tomography Dose Index (CTDI). L'utilizzo e la conoscenza di tali dosimetri è stata approfondita con un periodo di studio presso il Diagnostic Medical Physics Laboratory at the Department of Radiology and Imaging Sciences of the Emory University School of Medicine, Atlanta, Georgia (USA).
Due grandezze (che estendono il concetto di MGD) per la stima della dose sono state proposte (Mettivier *et al.*, 2016): MGD_t (che tiene conto della dose dovuta alla radiazione diffusa all'esterno della zona irraggiata) e MGD_v (che considera solo la dose nella regione irraggiata dell'organo).
Le grandezze proposte per calcolo della dose sono state utilizzate per acquisire delle immagini a dosi comparabili con quelle delle due proiezioni della mammografia (Longo and et al., 2016): questi primi risultati dimostrano che l'esame clinico, nelle condizioni particolare di SYRMA-CT, possa essere eseguito.
Il codice sviluppato è inoltre utilizzato per l'ottimizzazione dei parametri di scansione che saranno alla base del protocollo d'esame da sottoporre al comitato etico.
Sono in fase di studio le distribuzioni di dose che tengono conto delle diverse modalità di irraggiamento possibili (quali spiral-CT, irraggiamento di tipo *step and go*, etc.) nonchè la possibilità di stimare la dose ghiandolare media *post-exam* utilizzando le immagini stesse della paziente per un'accurata modellizzazione dell'organo.

Chapter 1

Introduction

This chapter introduces the reader to the scientific background in which the PhD research has been developed. The PhD research was performed within the SYRMA-CT (SYnchrotron Radiation for MAmmography - Computed Tomography) project, funded by Istituto Nazionale di Fisica Nucleare (INFN), and, in particular, within the dosimetry work package, coordinated by Dr. Giovanni Mettivier (from INFN, sezione di Napoli).
The SYRMA-CT project is a consequence of the first clinical experience in Mammography with Synchrotron Radiation: the results of this first clinical study showed the potential of synchrotron radiation applied to mammography, both in term of dose reduction and diagnostic power (Castelli and et al. (2011) and Longo *et al.* (2014)).
The SYRMA-CT project reflects the worldwide clinical trend of transition from 2D to 3D imaging for reducing some related issues as the tissues superimposition.
The aims of this PhD work and the thesis structure are presented, paying attention to the scientific knowledge that will be achieved within this PhD research.

1 Mammographic exams

Digital Mammography (DM) is the standard method for the early detection of the breast cancer. However, this technique is reported to have a sensitivity of 60% - 90% (e.g. the percentage of sick people correctly identified as such) and a specificity of 80% - 95% (e.g. the percentage of healthy people correctly identified as not having the condition). Moreover, an inherent problem with DM is that the linear attenuation coefficient of breast cancer is very similar to that of healthy glandular tissue (Chen and et al., 2010): this implies further clinical exams for an unequivocal diagnosis. The second-level tests can be not invasive as UltraSonography (US) and Magnetic Resonance Imaging (MRI) or invasive as biopsies.
Mammography with Synchrotron Radiation (MSR) has been proposed as a second-level exam since 2006 (Castelli and et al., 2011): this is a innovative x-ray imaging technique which combines dose reduction (due to the monochromatic synchrotron beam) and the exploitation of phase effects (due to the high spatial coherence of Synchrotron Radiation (SR)).
This first clinical study has been performed at Elettra, the Italian synchrotron light source in Trieste (Italy), where a dedicated beamline (SYRMEP, SYnchrotron Radiation for MEdical

Physics) has been specifically designed for medical applications.
The results of the clinical study show that the images obtained by the Phase-Contrast Imaging (PCI) techniques can lead to a more accurate diagnosis (Castelli and et al. (2011), Quai *et al.* (2013)) and have the capabilities of detecting subtle differences between breast materials, leading to an improvement of the diagnostic performances (Longo *et al.*, 2014).
Recently, Digital Breast Tomosynthesis (DBT) (Skaane and et al., 2013) and Breast Computer Tomography (BCT) (Glick, 2007) have been proposed to overcome issues related to tissue overlapping in the 2D imaging.
The transition from planar to 3D imaging is carried on with DBT (Sechopoulos (2013a) and Sechopoulos (2013b)) and BCT (Prionas *et al.* (2010), Connell *et al.* (2014) and Zhao *et al.* (2015)).
The SYRMA-CT collaboration has the aim to set-up the first clinical study for the BCT with SR (BCT-SR): the project will combine high quality images and low delivered dose.

2 Breast dosimetry

Mammography exams involve the use of ionizing radiation, therefore, a suitable parameter that quantifies the radiation dose delivered to the highly radiosensible component of the breast was introduced.
The first parameter proposed for estimating the radiation dose during a mammographic exam was the Mean Glandular Dose (MGD) introduced by Hammerstein (Hammerstein *et al.*, 1979). The definition of the MGD assumes that the whole breast is exposed to the x-ray beam (Dance (1990), Wu *et al.* (1994), Boone (1999), Boone (2002), Boone *et al.* (2004), Dance *et al.* (2000), Dance *et al.* (2009), Dance *et al.* (2014)). However, according to the SYRMA-CT setup, a whole breast exam might not be performed: the reduced SR beam size (typically of 3 mm) cannot cover the whole breast so multiple turns and vertical shifting of the patient support are required. Thus, in order to limit the total scan time, only a partial breast irradiation could be performed (from 3 cm to 5 cm) and an extension of the MGD parameter should be defined. No studies of a partial breast irradiation are present in the literature, so dedicated dosimetry tools are needed for the SYRMA-CT exam.

3 PhD research aims and thesis structure

The main aim of the PhD research is to develop methods for the evaluation of the dose delivered to patients during the SR-BCT exams. Due to the partial breast irradiation, no previous studies are presented in the literature as in the clinical mammographic exams the whole breast is always exposed. Thus, a suitable Monte Carlo code has been developed for calculating the coefficients which allow the dose to be evaluated. The toolkit GEANT4 is the MC software used in this research.
An upgrade of the dosimetric safety system present on the SYRMEP beamline to meet the requirements of the SR-BCT exams is needed (as the ionizing chambers, which allow the measurement of the air-kerma during the exam, has to be calibrated to higher energy).

This thesis has the following structure:

- In the *SYRMA-CT Project* chapter a description of the main novel elements of the project will be given, paying attention to the scientific relevance of this project and to the dosimetric aspects that it implies;
- *SYRMEP Synchrotron Beamline* chapter presents an overview of the synchrotron beamline at ELETTRA, the italian synchrotron in Trieste. The main parts of the beamline are described focusing the attention on the dosimetric and safety system;
- *Breast Dosimetry* chapter summarizes the state of the art for the dose evaluation in the breast exams: starting form the digital mammography, the evolution of the dose index for the latest technologies (as Digital Breast Tomosynthesis and Cone Beam Breast Computed Tomography) is discussed;
- *Clinical Breast Dosimetry* chapter analyzes the preliminary results obtained at the Department of Radiology and Imaging Science of the Emory University School of Medicine, in Atlanta, Georgia (USA). This chapter describes a complementary activity performed within the clinical breast dosimetry field and presents the characterization of some dosimetry devices (as ThermoLuminescence Dosimeters, Radiochromic films and Metal Oxide Semiconductor Field Effect Transistor). A pre-existent Monte Carlo code (based on GEANT4) was modified for validation purposes and with the aim of implementing a voxelized breast phantom;
- The *Monte Carlo Simulation* chapter thoroughly describes the choices implemented in the code developed during this PhD research. A careful validation both with the main literature and experimental measurements is presented;
- In the *Results* chapters the results of the application of the Monte Carlo code to the peculiar requirements of the SYRMA-CT project are shown: two dosimetric quantities are proposed and the implications are deeply discussed;
- In the *Conclusions* chapter the purposes achieved within this PhD work are summarized and the future perspectives of this work are presented.

Chapter 2

The SYRMA-CT Project

This chapter presents to the readers an overview of the SYRMA-CT (SYnchrotron Radiation for MAmmography - Computed Tomography) project which includes the work performed within this PhD.
The SYRMA-CT project is introduced as a consequence of the first experience in Phase-Contrast Mammography with Synchrotron Radiation.
The innovative elements that characterize the project are presented and discussed in detail.

1 Phase-Contrast Mammography with Synchrotron Radiation

The use of Synchrotron Radiation (SR) for medical applications is well documented in the literature (Brahme (2014) and Bravin *et al.* (2014)). The x-rays generated from the synchrotrons are monochromatic, tunable in energy, with a laminar shape and have sufficient spatial coherence to allow the exploitation of phase effects (Fitzgerard, 2000).
The simplest phase-contrast approach is to place the detector not immediately behind the sample (as it is done in the most conventional x-ray imaging applications) but to a distance that will allow an interference pattern to develop. This technique is the so-called free-space propagation: the phase modulation of the transmitted beam is transformed into an amplitude modulation and the contrast is generated from the wave interference (Snigirev *et al.*, 1995).
The potential of using the SR to improve the image quality in mammography was investigated with *in-vitro* studies by several authors (Arfelli and et al. (1998), Ingal *et al.* (1998), Takeda *et al.* (1998), Arfelli and et al. (2000), Pisano and et al. (2000)): the results of these investigations proved that a transition from *in vitro* to *in vivo* studies could be achieved.
The first clinical program involving the SR applied to a mammographic exam was launched in 2006 (Castelli and et al., 2007) at Elettra, the synchrotron radiation facility in Trieste, Italy.
Phase-Contrast Mammography with Synchrotron Radiation (MSR) has been performed since 2006 (Castelli and et al., 2011): 71 female patients (age range 41-82 years) underwent MSR after reporting breast abnormalities unresolved at the conventional Digital Mammography (DM) and UltraSonography (US).
The first analysis (limited to 49 patients) performed both a qualitative and a diagnostic assessment (Castelli and et al., 2011) suggesting that MSR could be used to clarify cases of questionable or suspicious breast abnormalities.

The qualitative assessment was extended to the whole population study by Longo *et al.* (2014) which confirmed that phase-contrast MSR depicts normal structures and abnormal findings with higher image quality compared to DM.
Diagnostic performance and dose assessment of the whole cohort were analyzed by a further study: the application of a tunable monochromatic beam (in the energetic range 17 keV - 22 keV) allows a substantial reduction of the Entrance Skin Air Kerma (ESAK) and Mean Glandular Dose (MGD) (average of 40%) compared to what delivered in the clinical mammography; moreover, the phase-contrast MSR demonstrated better diagnostic accuracy (with promising results for dense breasts (Fedon *et al.*, 2014).

2 Phase-Contrast Breast Computed Tomography with Synchrotron Radiation

An inherent problem with DM is the superimposition of tissue that can lead to a wrong diagnosis. New 3D imaging techniques have been proposed for overcoming this issue.
The transition from the planar acquisition (with DM) to 3D imaging is moving to the clinical practice with the Digital Breast Tomosynthesis (Sechopoulos (2013a), Sechopoulos (2013b)).
Dedicated Breast Computed Tomography (BCT) is another 3D imaging technique under investigation: BCT displays 3D images of the internal structures of the breast. BCT could potentially improve the diagnostic accuracy (Connell *et al.*, 2014), however, the main constrain in the development of this technique is the limitation of the delivered dose (Kalender *et al.* (2012), Vedantham *et al.* (2013)).
The challenge in x-ray breast imaging is to match high image quality and acceptable dose delivered.
The use of SR for tomographic imaging has been the subject of specific investigations in different SR light source facilities: the SYRMEP beamline of Elettra synchrotron in Trieste, Italy (Pani and et al. (2004), Rigon and et al. (2011)) or the ID17 beamline of the European Synchrotron Radiation Facility in Grenoble, France (Zhao and et al., 2012).
Combining the results obtained with the first MSR clinical study (Castelli and et al. (2011), Longo *et al.* (2014)) with the need of improving diagnostic accuracy with the 3D imaging, the SYRMA-CT project was proposed. The aim of the SYRMA-CT collaboration is to set up the first clinical trial of Phase-Contrast Breast Computed Tomography with Synchrotron Radiation (BCT-SR) at the SYRMEP beamline of Elettra synchrotron facility (Trieste, Italy).
The project is founded by Istituto Nazionale di Fisica Nucleare (INFN, the Italian National Institute for Nuclear Physics) and involves several other institutions as research institutions, academic institutions and hospital institutions of the italian national area.
In order to combine high image quality and low delivered dose, several innovative elements have been merged: a novel single photon counting detector, the state-of-the-art CT algorithms and a suitable dosimetric assessment.

2.1 PIXIRAD Photon counting detector

The use of photon counting detectors in a medical environment has been proposed for many years (Taguchi and Iwanczyk, 2013). PIXIRAD is a high-efficiency photon-counting direct-conversion x-ray imaging detector (Bellazzini *et al.*, 2013). The sensor (ACRORAD Co., Ltd.) is a Schottky type diode array with electron collection on the pixel, made of a crystalline Cadmium Telluride (CdTe) substrate with an area of 30.96 mm x 24.98 mm and a thickness of 0.65 mm. The use of CdTe has some suitable properties (Takahashi and Watanabe, 2001) as a high atomic number (Z_{Cd} = 48, Z_{Te} = 52), which gives a high quantum efficiency in the 10-500 keV range, and a large band-gap (E_{gap}), which allows the detector to operate at room temperature.
The basic block has a hybrid architecture in which the sensor and readout electronics are manufactured and processed separately and then coupled with the flip-chip bump-bonding technique. The pixels are arranged on a honeycomb matrix with a pitch of 60 μm. Each pixel incorporates an hexagonal electrode (top metal layer) connected to a charge amplifier, which feeds two discriminators, and two 15 bit counters. The detector is produced by PIXIRAD Imaging counters s.r.l., a spin-off company of INFN.
In the SYRMA-CT project a multi-block module is used, which is based on a 8-unit system (PIXIRAD-8) for a global active area of 250 mm x 25 mm. Hence, raw images have 4608 x 476 pixels (see Fig. 2.1).

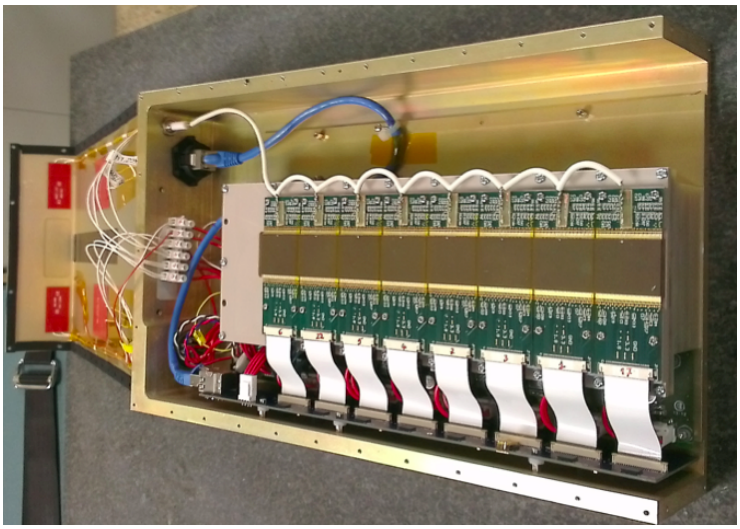

Figure 2.1: PIXIRAD-8 CdTe unit: count rate > 30 GHz, high efficiency in the energetic range of SYRMA-CT (30 - 40 keV), "noiseless" (a low threshold of 2 keV), readout at 30 frames/s.

Due to the modular structure of the device, a dead space of 60 μm between adjacent blocks is present. The detector performances have also been tested at the SYRMEP beamline for establishing the energy resolution and for verifying the linearity at the photon rates expected for the BCT-SR (Vincenzi *et al.*, 2015).

2.2 Reconstruction algorithms

The reconstruction algorithms can be divided into two categories:

- Analytic
- Iterative

The main analytic reconstruction techniques are the Filterd Back Projection (FBP) and the Discrete Fourier Transform (DFT) method (Kak and Slaney, 1988). These methods require low computational time (compared to the iterative techniques) and have been successfully applied to the medical CT reconstructions.
The main iterative technique (Beister *et al.*, 2012) is the Algebraic Reconstruction Technique (ART) (Gordon *et al.*, 1970) with its variations (e.g. Simultaneous Algebraic Reconstruction Technique, SART (van der Sluis and van der Vorst, 1984), or Simultaneous Iterative Reconstruction Technique, SIRT (van der Sluis and van der Vorst, 1990)). The computational time required for the iterative reconstructions is higher than the analytic methods.
In the SART algorithm, the iterative corrections are made angle-by-angle and applied simultaneously to all rays of the projection; a single iteration is considered to be completed when all projections have been used.
The aim in the SYRMA-CT project is to preserve not only the x-ray absorption but also the edge enhancement due to the phase effects.
In a preliminary stage of the project these main algorithms were tested in several modalities (Pacile and et al., 2015); whilst the first results of SYRMA-CT are presented in Longo and et al. (2016) . The FBP was used as a gold standard to evaluate the performance of the SART algorithm with a reduced number of projections.
In order to exploit the phase information carried out by the projections, a phase retrieval filter following the Homogeneous Transport of Intensity (TIE-Hom) Algorithm (Paganin *et al.*, 2002) was applied.

2.3 Dosimetric assessment

The SYRMA-CT project requires a specific dosimetric assessment for its peculiar irradiation modality.
At the SYRMEP beamline of Elettra Laboratory there is a dedicated facility for the clinical mammography exam (Fig. 2.2). During the exam the patient lies on a support (Fig. 2.2, right side) with the breast hanging from a hole located in the support; during the scan the patient bed is vertically moved while the image is recorded.


Figure 2.2: Main entrance of the mammography facility (left side). Patient support (right side).

In a CT exam the support needs to rotate and, due to the fix height of the synchrotron radiation beam (typically 3 mm), also to vertically shift. In order to preserve the patient comfort, the total time scanning needs to be as short as reasonably achievable, thus, only a portion of the breast is imaged.
This partial irradiation modality, never done before, requires a specific dosimetric assessment that allow the patient dose to be evaluated.
The delivered dose can be evaluated by measuring the Entrance Skin Air Kerma (ESAK) with the calibrated ionization chamber on the SYRMEP beamline (for details see chapter three), and the so-called Normalized Glandular Dose (DgN) coefficients, which can be only estimated by Monte Carlo simulations.

Chapter 3

SYRMEP Synchrotron Beamline

The chapter describes the SYRMEP (SYnchrotron Radiation for MEdical Physics) beamline of the ELETTRA Italian synchrotron light source (Trieste, Italy).
The main parts of the beamline are described focusing the attention on the dosimetric and safety system.

1 Characteristics of ELETTRA and SYRMEP beamline

ELETTRA is a synchrotron light source facility with a storage ring of 259.2 m of circumference located in Trieste, Italy (Fig.3.1).

Figure 3.1: ELETTRA Synchrotron in Trieste, Italy.

Two electron energies are available: 2.0 GeV and 2.4 GeV. The ring operates in top-up mode, which consists in a continuous electrons injection to keep the current constant in time and to provide higher brightness and particle beam stability.
The electron beam is generated from a ceramic disc heated at high temperatures; the electrons are guided by a high electric field (up to 100 kV) to a 12 m LINAC accelerator.
The LINAC accelerates the electrons to the final energy of 100 MeV by operating a 3 GHz. The electrons are then transferred to the Booster (i.e. a small synchrotron with 118 m of circumference) which can accelerate a maximum current of 6 mA from 100 MeV to 2.5 GeV.
At this point, the electrons are transferred to the storage ring; the energy lost by emitting Synchrotron Radiation (SR) is compensated by radiofrequency cavities which operate at 500

MHz.
In total, 432 electron bunches, separated by 2 ns, can circulate in the ring and the entire system is under vacuum in order to avoid collisions with gas molecules.
ELETTRA has 26 beamlines which offer the users the possibility to exploit the most important x-ray based techniques in the area of spectroscopy, spectromicroscopy, diffraction, scattering and lithography (Fig.3.2).

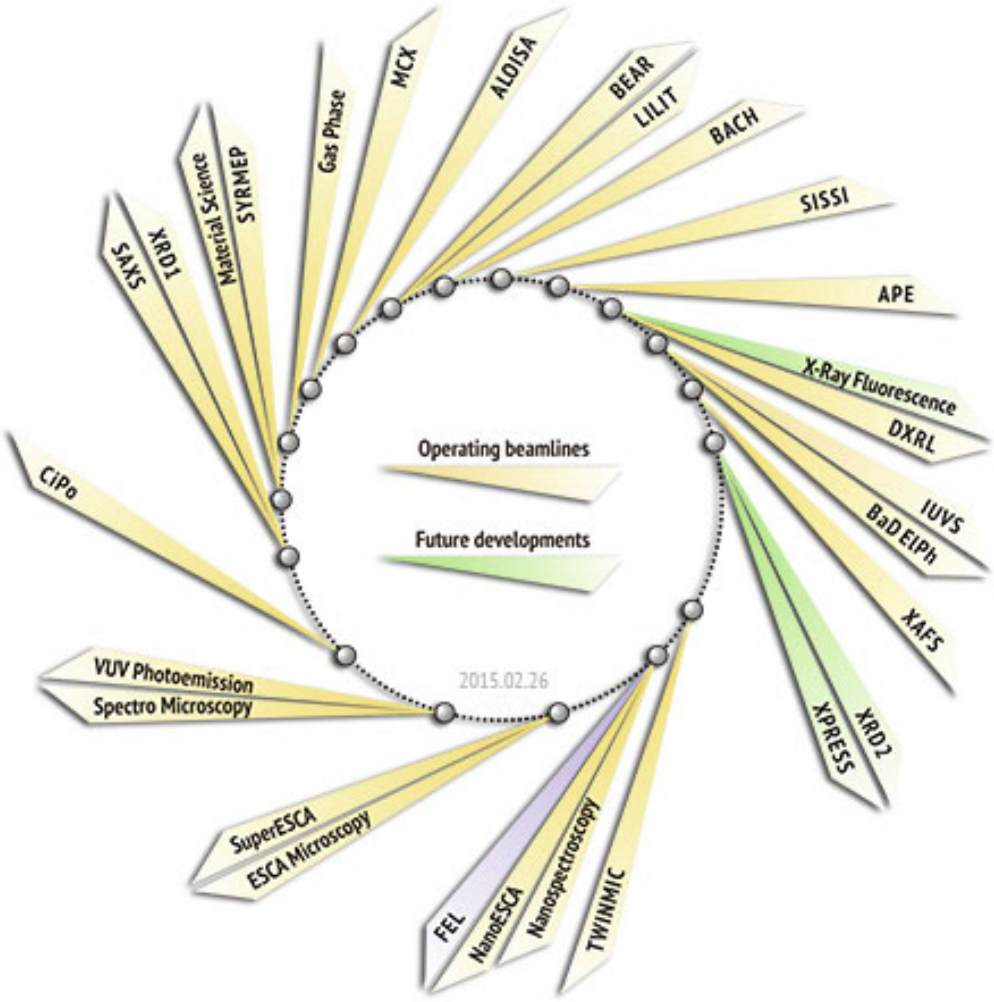

Figure 3.2: Scheme of ELETTRA beamlines (https://www.elettra.trieste.it/lightsources/elettra/beamlines.html).

SYRMEP (SYnchrotron Radiation for MEdical Physics) beamline was designed by ELETTRA in cooperation with the University of Trieste for researching in medical physics. The advantages of using monochromatic SR for medical applications have been widely described in the past years (Lewis, 1997).
The white beam, coming from a bending magnet, is monochromatized by a silicon (111) double crystal working in Bragg configuration. The emerging beam is parallel to the incident one with a vertical displacement of 20 mm (Fig. 3.3).

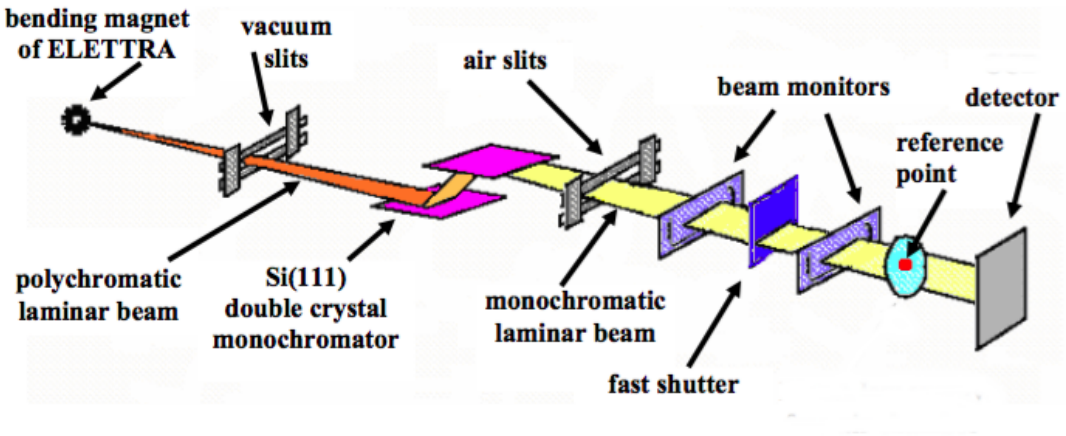

Figure 3.3: Schematic diagram of SYRMEP beamline: the polychromatic beam comes from a bending magnet and then it is monochromatized by a Si (111) double crystal. The emerging monochromatic beam is sent to the experimental hutch and to the patient room, see Fig. (3.4).

The beamline can be divided into three main parts, as shown in Fig.(3.4): the optics hutch, the experimental hutch and the patient room.

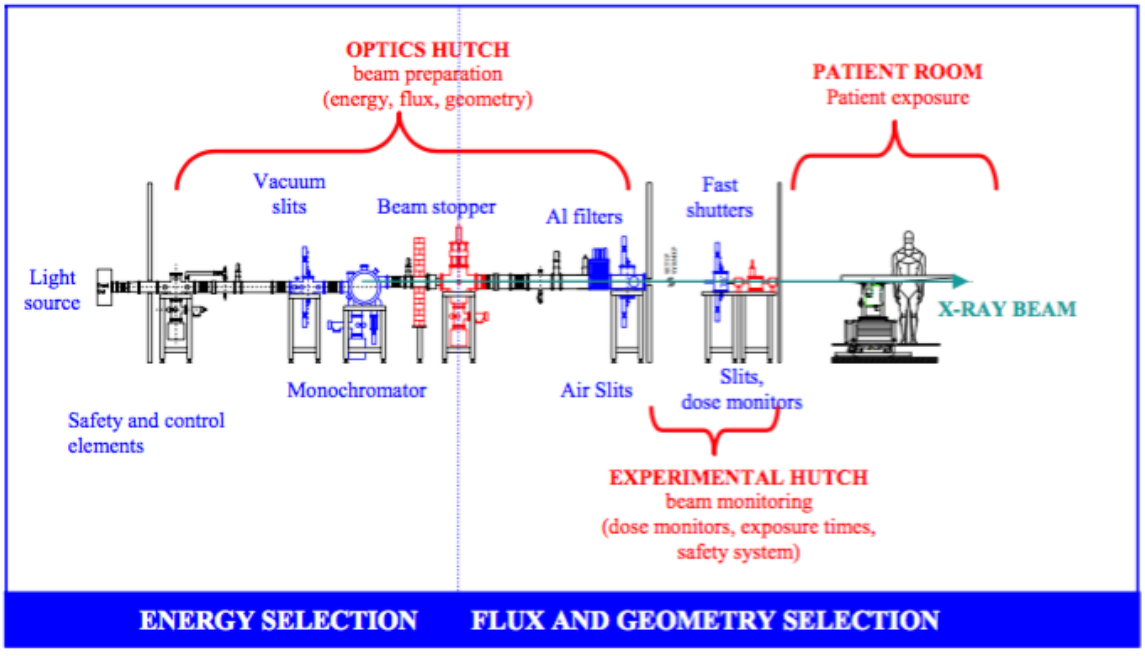

Figure 3.4: Layout of the SYRMEP beamline. The three main parts in which the beamline can be divided are shown: the optics hutch (with all the beam preparation devices), the experimental hutch (where the majority of the experiments takes place) and the patient room (where there is the patient facility).

1. *The optics hutch.* The first section is separated from the rest of the storage ring by a Beryllium window. The size of the polychromatic beam emerging from the bending magnet is defined by a vacuum slit system. The monochromator is placed after the

vacuum slit. The ultimate beam shape can be defined by an air-slit system in order to reduce scatter radiation. A series of thin Aluminum filters (with different thicknesses) are installed after the monochromator and are used to vary the beam intensity. The presence of a 10 cm thickness Tungsten bar (beam stopper) assures the stop of the beam, including the gas bremsstrahlung radiation produced by the interaction of electron beam with the residual gas in the vacuum chamber.

2. *The experimental hutch.* The experimental room is the second section of the beamline and it is located 23 m far from the source. Here the beam is no longer in vacuum but in air. A customized ionization chamber is used for monitoring the beam flux. The patient dosimeter system and the safety shutter are also located in this room.

3. *The patient room.* The end station of the SYRMEP beamline is the patient facility, dedicated to mammography studies; it is composed by the patient exam room and the radiology room. The beam vertical dimensions are defined by a fixed Lead aperture of 3 mm. At the breast position (reference point in Fig. 3.3) the beam cross-section is about 3.4 mm x 210 mm.

The beam fluence rate as a function of the energy is shown in Fig.(3.5): the data are referred to an energy of 2.0 GeV (blue) and 2.4 GeV (red) at the maximum electron beam current (respectively of 300 mA and 180 mA).

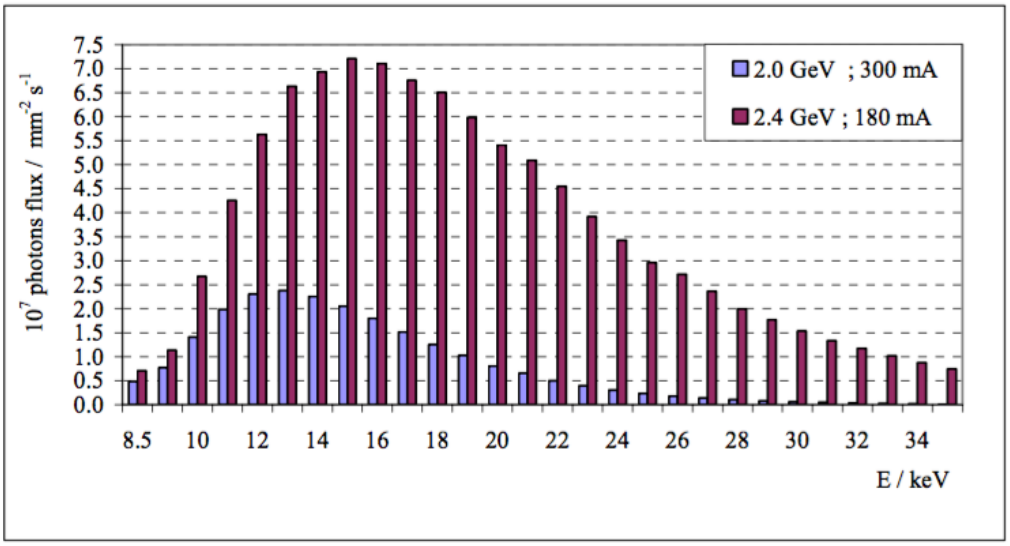

Figure 3.5: Photon flux as a function of the photons energy at the patient reference point for the two ELETTRA working modalities: 2.0 GeV (blue color) and 2.4 GeV (red color).

The relevant characteristics of the SYRMEP beamline are summarized in Fig. (3.6).

Characteristic	Value
Light source	
Type	Bending magnet
Critical energy (at 2.0 GeV)	3.21 keV
Critical energy (at 2.4 GeV)	5.59 keV
Source size	100 μm x 1100 μm
Horizontal angular acceptance (beam divergence)	7 mrad
X-ray beam at reference point	
Energy Resolution	$\Delta E/E = 2*10^{-3}$
Typical photons fluxes at 15 keV	2×10^8 /mm^{-2} s^{-1} (at 2 GeV, 300 mA) 7×10^8 /mm^{-2} s^{-1} (at 2.4 GeV, 180 mA)
Beam Size	120 mm x 4 mm
Source-to-sample distance	about 30 m (26.5 m in vacuum)

Figure 3.6: Relevant characteristics of the light source and the x-ray beams for the SYRMEP beamline: the energy ranges from 8 keV up to 40 keV.

2 Dosimetry and safety system

The aim of the dosimetry system is to measured the Entrance Skin Air Kerma (ESAK) delivered to the patient while the aim of the safety system is to guarantee the security of the whole procedure. Fig. (3.7) shows the system: two high precision ionization chambers (IOC-A and IOC-B) are on the beamline for monitoring the beam and 3 shutters are present for the exam interruption in case of emergency or alarm (SH_G is a fast guillotine shutter for emergency while SH_A and SH_B are imaging shutters). The main design concept is the redundancy of elements: all the devices have to be doubled and differentiated (if possible) in order to avoid any issue.

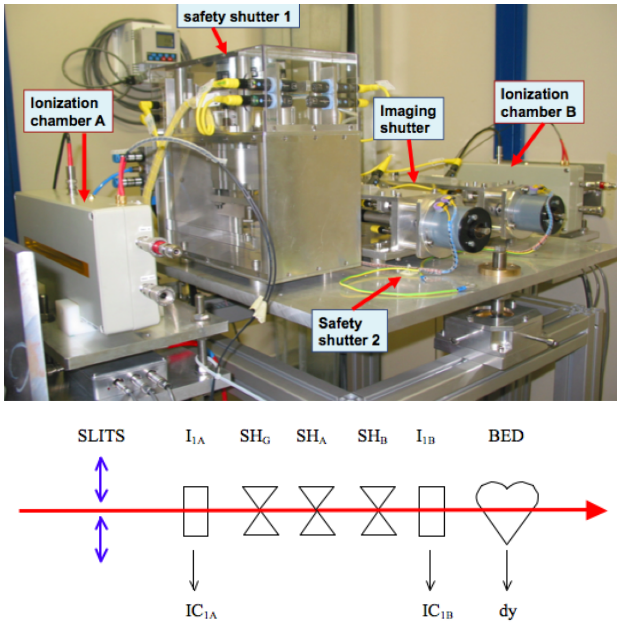

Figure 3.7: The dosimetry and safety system at the SYRMEP beamline.

2.1 Ionization chamber

The two ionization chambers (named IOC-A and IOC-B) were designed and constructed at the ELETTRA laboratories specifically for a laminar beam geometry. The chambers (Fig. 3.8) have a thin entrance and exit windows (made by Mylar foils, 50 μm, and covered on each side by 50 *nm* of Aluminum) suited for the SR beam shape and dimension. The sensitive volume is constituted by two regions (12.5 mm thick) delimited by two HV electrodes and separated by a central electrode (whose dimensions are 250 mm x 50 mm). All the components are inside an Aluminum box (32 x 16 x 6.5 cm^3).

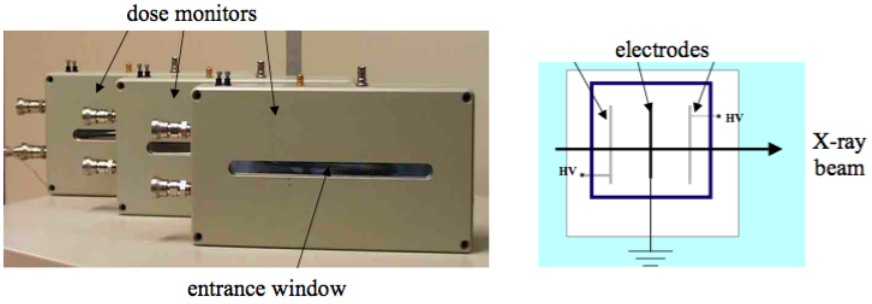

Figure 3.8: Ionization chambers (IOC-A/B) for dose monitoring at the SYRMEP beamline. The direction of the incidence beam is perpendicular to the electrodes chamber (see diagram on the right side).

Short and long-term stability of the ionization chambers have been accurately verified (Bovi and et al., 2006) by the Istituto Nazionale di Metrologia delle Radiazioni Ionizzanti (INMRI, National Institute of Metrology for the Ionizing Radiation) of the Ente Nazionale per l'Energia e l'Ambiente (ENEA, National agency for Energy and Environment).
Absolute measurements of air kerma were made by the national standard free-air chamber for low energy x-rays; this chamber was located at the reference point (see Fig. 3.3) below the patient support where the patient breast is positioned (Fig. 3.9).

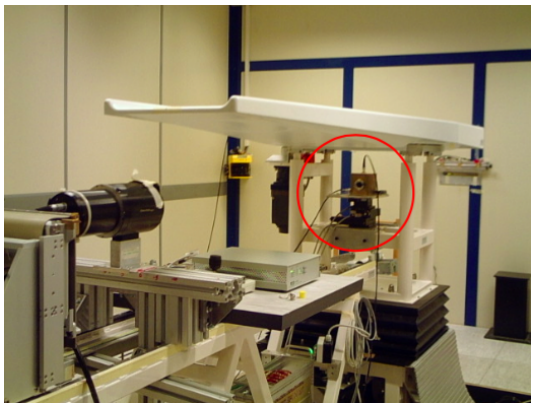

Figure 3.9: Position of the national standard free-air chamber for low energy x-rays (red circle) at the reference point, inside the patient room.

The measured air kerma rate is given by the following equation:

$$\dot{K} = \frac{I}{\rho_{air} V} \frac{W_{air}}{e} \frac{1}{1 - g_{air}} \prod_i k_i \tag{3.1}$$

where ρ_{air} is the air density under reference conditions, V is the chamber volume, I is the ionization current, W_{air} is the mean energy expended by an electron of charge e to produce an ion pair in air, g_{air} is the fraction of the initial electron energy lost by bremsstrahlung production in air, and $\prod_i k_i$ is the product of the correction factors to be applied to the standard. A list of correction factors and the values used for the physical constants pair and for $\frac{W_{air}}{e}$ are given in (Burns *et al.*).
The values of the calibration coefficients for the ionization chambers IOC-1 and IOC-2 are shown in Fig. (3.10).

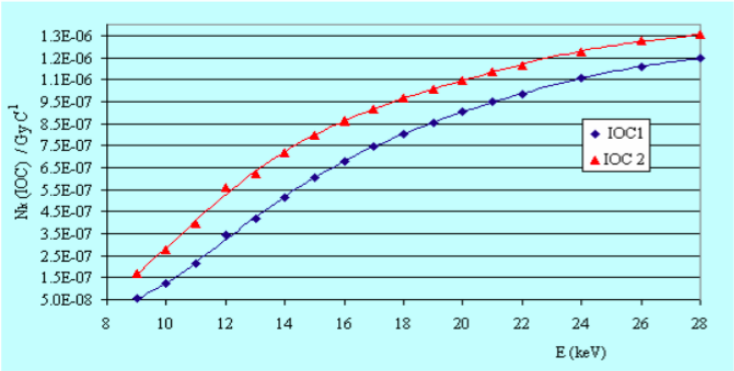

Figure 3.10: Calibration coefficients for IOC 1 (blue squares) and IOC 2 (red triangles), normalized to the reference environmental condition (temperature of 293.15 K, pressure of 1013.25 Pa and 50% of relative humidity).

The measurements were performed with the aim to focus the attention on the energy interval suitable for the mammography exam (i.e. 17 - 22 keV); in the case of the breast-CT the calibration will be extended up to 40 keV in order to perform the clinical exam in the range 30-38 keV.

2.2 Safety and imaging shutters

The safety shutters present on the SYRMEP beamline are a guillotine shutter (SH_G) and two fast shutters (SH_A and SH_B), see Fig. (3.7). These three shutters are the main devices for the exam interruption in case of any issue.
The fast guillotine shutter (SH_G) allows a sudden interruption of the beam irradiation placing a high Z mass element on the beam direction. As IOC-A is placed before all shutters, the dose rate can be evaluated before the patient irradiation. Thus, only if the measured dose (by IOC-A) is lower than the maximum ESAK the shutters SH_A and SH_B will be opened.
The two imaging shutters (SH_A and SH_B) allow a patient irradiation only if all the safety conditions are matching: beam stability, no people (except the patient) inside the patient room, positive emergency safety controls, etc. The cylindrical shape which they are made, allows a fast opening/closing movement procedure.

Chapter 4

Breast Dosimetry

In this chapter the main quantities used in the breast dosimetry are presented.
Particular attention is paid on showing how the Synchrotron Radiation Breast Computed Tomography exam combines together the dosimetric quantities used in Mammography and in Computed Tomography.

1 Dosimetric assessment in Mammography

The evaluation of the dose delivered during an x-ray exam is the key point for understanding the benefits of the exam. Every x-ray examination has a small but significant risk of radiation induced carcinogenesis.
In an x-ray mammography examination the target is the female breast: the standard female breast is defined, according to the recent publication (Commission, 2006), as semi-circular and consists of a 4 cm central region made of a mixture of adipose and glandular tissue, surrounded by a 0.5 cm of adipose layer. Fig. (4.1) show the breast model with the dimension according to (Dance, 1990). The adipose tissue is not considered to be at risk of induced carcinogenesis while the glandular component is highly radiosensitive.

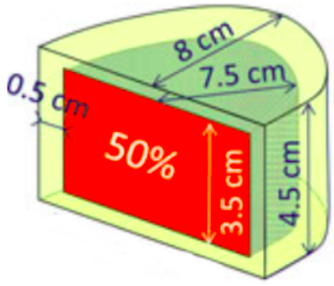

Figure 4.1: Semi-circular breast model with the dimensions as reported in (Dance, 1990). The figure is extracted from (Geeraert *et al.*, 2015).

The clinical exam uses a polychromatic x-ray beam emitted from an x-ray tube in the set up shown in Fig. (4.2).

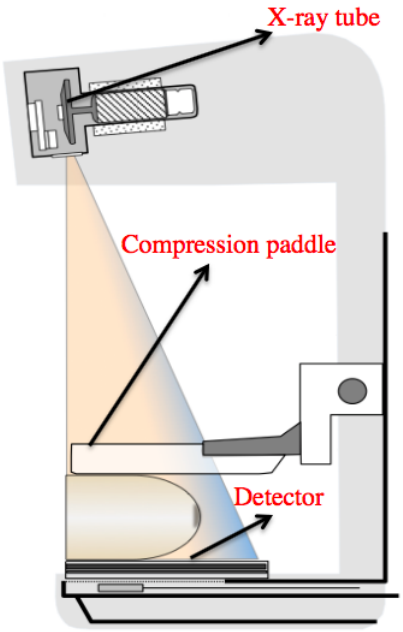

Figure 4.2: Clinical mammography set up: the x-ray are emitted from an x-ray tube towards the breast. The breast is compressed by a compression paddle and the image is recorded by a detector (courtesy of J.M. Boone presentation).

The standard exam consists of two projections: Cranio-Caudal (CC) projection and Medio-Lateral Oblique (MLO) projection. Examples are shown in Fig. (4.3).

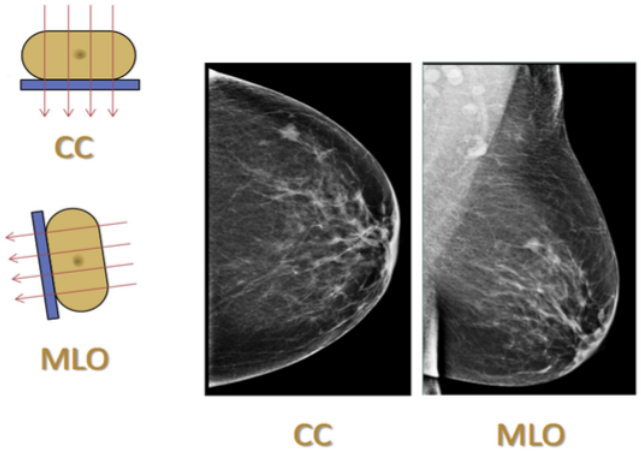

Figure 4.3: The two views of standard mammographic exam: Cranio-Caudal (CC) projection and Medio-Lateral Oblique (MLO) projection (courtesy of J.M. Boone presentation).

The work of Hammerstein *et al.* (1979) has been the first to suggest that the mean dose to the glandular tissues within the breast is a suitable dosimetric quantity. Since that, the evaluation of the Mean Glandular Dose (MGD) has been investigated by many authors (Kulkarni and Supe (1984), Wu *et al.* (1991), Wu *et al.* (1994), Boone (1999), Boone (2002)).
The works of Dance (Dance (1990), Dance *et al.* (2000),Dance *et al.* (2009), Dance *et al.*

(2014)) proposed the evaluation of the MGD following the formula:

$$MGD = K_{air} \cdot g \cdot c \cdot s \tag{4.1}$$

where K_{air} is the entrance skin air kerma (ESAK) and g, c, s are factors that take into account respectively the air kerma to average glandular dose conversion (as a function of breast thickness and the HVL value), the glandularity and the x-ray spectrum. All these coefficients cannot be estimated with direct measurements and their calculation is only based on computational methods. Thus, the Monte Carlo (MC) techniques became the key-instruments to overcome the issue of MGD evaluation.
Great efforts were paid to improve the MC code for better estimating these coefficients as shown by the recent works of many authors (e.g. Dance *et al.* (2014)).
In 1999 John Boone (Boone, 1999) introduced the DgN coefficient (normalized glandular dose) for estimating the MGD for a polychromatic spectrum and for monoenergetic beams (Boone, 2002). The DgN coefficients (normalized to the entrance surface exposure) take into account the different breast glandularity throughout the so called G-factor parameter defined as

$$G = \frac{f_g \left(\frac{\mu_{en}}{\rho}\right)_g}{\left[f_g \left(\frac{\mu_{en}}{\rho}\right)_g + (1 - f_g)\left(\frac{\mu_{en}}{\rho}\right)_a\right]} \tag{4.2}$$

where the mass energy absorption coefficients (μ_{en}/ρ) are referred with an a subscript for adipose tissue and with a g subscript for glandular tissue, while f_g is the glandular fraction, by weight, of the breast tissue ($f_g = 1$ for glandular, $f_g = 0.5$ for 50% glandular, etc.). The G-factor should be applied interaction-by-interaction (as described by Wilkinson and Heggie (2001)), however, not all authors agree with this method, as noticed in (Fedon *et al.*, 2015).

2 Dosimetric assessment in Computed Tomography

The dose in x-ray computed tomography (CT) first received appropriate attention since the introduction of CT in the 1970s. The first quantity proposed for characterizing the CT scanner exposure output was the definition of the Computed Tomography Dose Index (CTDI). The CTDI concepts are well documented and have recently been re-evaluated (AAPM (2010), IEC (2010), IAEA (2011)). The CTDI is a measure of the CT scanner radiation output usually quoted in units of mGy/100 mAs. The concept of CTDI was proposed and established in the USA by the Food and Drug Administration in the late 1970s (Shope *et al.*, 1981).
The measurement is made by two polymethylmethacrylate cylinders of 15 cm length and a diameter of 16 cm (head phantom) and 32 cm (body phantom). Each phantom has one central hole and four peripheral holes in which a 100 mm long ionization chamber is inserted, Fig. (4.4).

The CTDI is determined as

$$CTDI_{\infty} = \frac{1}{nT} \int_{-\infty}^{+\infty} D(z) dz \tag{4.3}$$

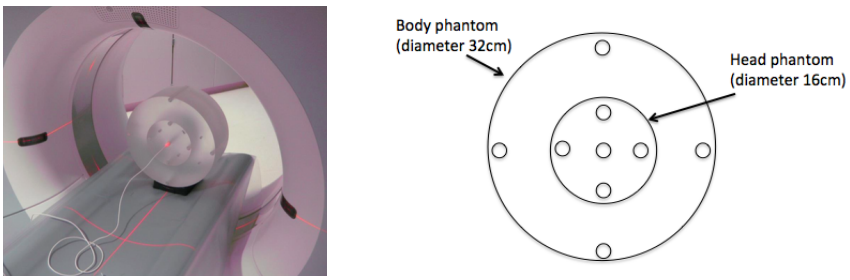

Figure 4.4: The phantoms used for the CTDI measurements made of PMMA with 16 and 32 cm diameter. The holes are the places where the ionization chamber is inserted.

where T is the section thickness, n refers to the number of sections (or slices) and D(z) is the dose distribution along the z-axis. The meaning of the formula in Eq. (4.3) is explained in Fig. (4.5): ideally the CTDI should be measured for $-\infty$ to $+\infty$ for taking into account the tails of the dose distribution along the z-axis.

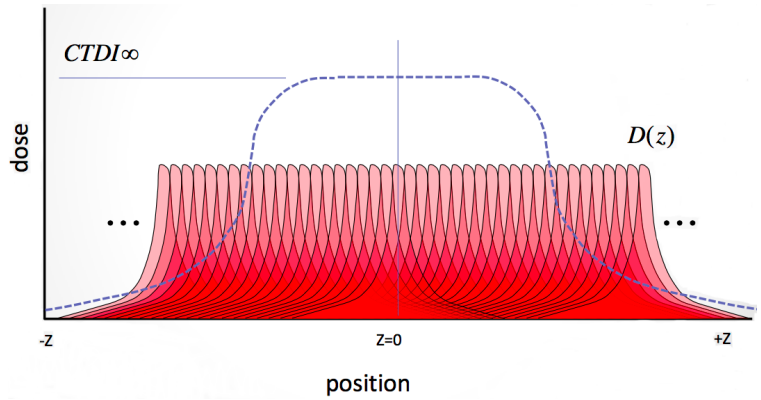

Figure 4.5: The single slice dose is shown with the red curves while the CTDI value is expressed by the blue dotted line: ideally the CTDI should be measured for $-\infty$ to $+\infty$ for taking into account the tails of the dose distribution along the z-axis.

However, as the CTDI is measured using a ionization chamber 100 mm long, Eq. (4.3) becomes

$$CTDI_{100,x} = \frac{1}{nT}\int_{-50mm}^{+50mm} D(z)dz \tag{4.4}$$

where the integral is calculated along the length of the ionization chamber and the subscript x refers to the measurement position which can be central (c), peripheral (p) or in air (central in the field of measurement without phantom). This situation is shown in Fig. (4.6).

To take into account the non-homogeneity of dose distribution, a weighted CTDI was introduced according to the following equation:

$$CTDI_w = \frac{1}{3}CTDI_{100,c} + \frac{2}{3}CTDI_{100,p} \tag{4.5}$$

Doses estimates are intended to provide values in mGy, for this purpose the $CTDI_w$ is multiplied by the mAs product Q used in the exam, which is divided by the pitch factor p used

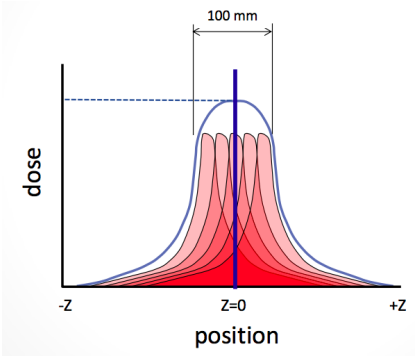

Figure 4.6: The dose distribution used for measuring the $CTDI_{100}$.

in a spiral CT acquisition. This leads to the $CTDI_{vol}$ expressed as:

$$CTDI_{vol} = CTDI_w \cdot \frac{Q}{p} \tag{4.6}$$

However, $CTDI_{vol}$ neither takes into account the patient-size nor the length of the scanned volume. Thus, the dose-length product (DLP) was introduced

$$DLP = CTDI_{vol} \cdot R \tag{4.7}$$

where R is the scan range (**?**).
The quantity DLP does not provide a dose value (as its unit is $mGy \cdot cm$). Nevertheless, it is a useful quantity to compare the dose levels and it serves as a surrogate for patient dose. For these reasons, it became accepted through the establishment of diagnostic dose levels (DRL) (Commission (1999) and Kalender (2014)) . Both $CTDI_{vol}$ in mGy and DLP in $mGy \cdot cm$ only provide a rough estimate of the patient dose levels involved (Kalender, 2014).

3 Dosimetric assessment in Breast Computed Tomography

The use of modern and advanced imaging techniques requires a new definition of the Normalized Glandular Dose (DgN) coefficients which allows the MGD to be estimated.
The new imaging modality of the Breast Computed Tomography (BCT) requires the definition of the DgN_{CT} as introduced by (Boone *et al.*, 2004) and (Sechopoulos *et al.*, 2010).
The DgN_{CT} is defined as the ratio of the glandular dose in the breast to the air kerma at the isocentre.

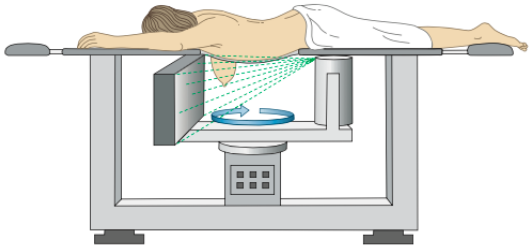

Figure 4.7: Typical Breast-CT scanner.

In a BCT examination the patient lies prone on a table-support and the x-ray tube rotates under the chest wall while the image is acquired, Fig. (4.7).
Values of DgN_{CT} (in terms of mGy/mGy) range from 0.95 (for a breast with a diameter of 8 cm at the chest wall) to 0.78 (for a 18 cm diameter) (Boone *et al.*, 2004).
In Sechopoulos *et al.* (2010) a characterization of a BCT clinical prototype (Koning Corporation, West Henrietta, NY) is given: the MGD can vary from 5.6 mGy to 17.5 mGy. In the same paper the ratio between the MGD delivered by the BCT unit and the MGD for two-view mammography (as function of compressed breast thickness, through an empirical relationship between breast diameter, measured at the chest wall, and compressed breast (Boone *et al.*, 2005)) is reported: the glandular dose ratio between the BCT prototype and the two-view mammography ranges from 1.4 (thicker breast) to 8 (2 cm compressed breast).
The request for a MGD lower (or at least comparable) than the two-view mammography one is between the main constrains of BCT (Kalender *et al.*, 2012): it is generally understood that the dose may have to be increased with a valid indication of patient benefit, however, it appears that the limit of the two-view mammography could safely be assumed as a very high benefit-to-risk ratio.

4 Dosimetric assessment for the SYRMA-CT project

In the SYRMA-CT project, the dosimetric assessment requires a particular attention. The patient lies in a prone position on the patient support (as in a BCT exam, Fig. (4.8)) but, in the case of the synchrotron radiation (SR) exam, the bed support is moved during the acquisition.

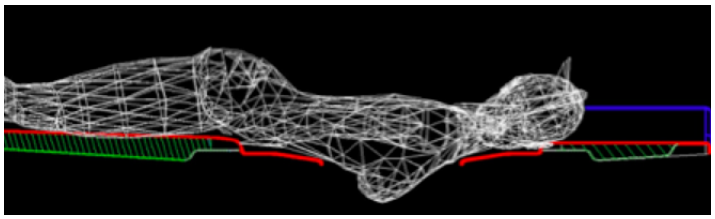

Figure 4.8: The patient lies prone on the support (green and red colors) with the breast freely pendant from a hole.

The SR beam has a limited vertical dimension (defined by a fixed slite of 3 mm at ELETTRA), thus, for a whole breast exam (BCT-SR), the patient support should vertically translate

(for scanning the breast from the chest wall to the nipple) and rotate at all different acquisition heights. This modality may require a long acquisition time that could make the exam uncomfortable. In order to limit the total scan time in multiple turns of the patient support, only a fraction of the pendant breast will be imaged: the region, where a suspicious lesion has been previously located (at the hospital), will be irradiated.
The condition of a partial breast irradiation calls for a specific dose evaluation system, as it is different from all the other breast exams. This evaluation have to be performed by considering the various heights of the total scanned section (the radiologist opinion is required).
A specific Monte Carlo code needs to be developed for evaluating the MGD in the SR-BCT exam and specific dosimetric quantities, which could combine together also the concept of CTDI (as the adjacent breast region can contribute to the dose) need to be derived . This will be the main aim of this PhD research.

Chapter 5

Clinical Breast Dosimetry

This chapter presents the dosimetry work performed at the Diagnostic Medical Physics Laboratory at the Department of Radiology and Imaging Sciences of the Emory University School of Medicine, in Atlanta, Georgia, USA. The work was done under the supervision of Prof. Ioannis Sechopoulos and in collaboration with Dr. Annalisa Trianni of the Udine University Hospital S. Maria della Misericordia (Italy).
Three different dosimetry devices were tested and characterized: thermoluminescence dosimeters (TLDs), radiochromic films (GAFs) and metal oxide semiconductor field effect transistors (MOSFETs). The aim is to compare the dosimeters performances inside an homogeneous breast phantom with the purpose to extend the analysis to an heterogeneous one (made using a 3D-printer). Plane dose distributions have be obtained both for homogeneous and heterogeneous phantoms.
A pre-existent Monte Carlo (MC) code, based on the toolkit GEANT4, was modified to match the experimental conditions in order to validate the code. A voxellized geometry was inserted in the MC code for allowing the heterogeneous phantom to be implemented .
Devices characterization measurements are discussed and some preliminary results of the plane dose distribution are presented. The results are not comprehensive because the study is still going on.

1 Aims of the Work

The monitoring of the radiation delivered to a patient during radiographic procedures is an area of increased interest. Therefore, the choice of the dosimetric technique used for a specific radiographic procedure has to be carefully made. To ensure consistency of radiation detection, the dosimeters have to be calibrated in the appropriate energy ranges before the use. Moreover, an ideal dosimeter should have these characteristics (Dong *et al.*, 2002):

- be simple to use;
- give a linear response within the measured dose range;
- provide real-time outputs;
- have a small area to prevent interference with image quality;

- be tissue equivalent;

Recent investigations in dosimetric field lead to dosimeters which combine together the highest number of this requirements: thermoluminescence dosimetry (TLD) for their high sensitivity, radiochromic films (GAF) for their simplicity of use and metal oxide semiconductor field effect transistor (MOSFET) for their immediate dose measurements.
The estimation of the absorbed dose in human breast is an important task for the mammographic quality control program. As discussed in Chapter 4, breast dosimetry is based on the evaluation of the mean glandular dose which is based on several assumptions: the main one is the glandularity estimation which is often higher than the reality (Yaffe *et al.*, 2009). Punctual dose and dose distribution evaluation can be powerful tools to better investigate the issue of correct dose estimation.
The aim of this study is to investigate the performances of three devices (TLDs, MOSFET and GAF) in a clinical mammographic energetic range: starting from measurements in an homogeneous phantom (produced by CIRS) the purpose is to extend the study to heterogeneous phantoms (made by a 3D-printer) that better reproduce the real breast with the aim to obtain a patient-specific dose evaluation.

2 Equipments

The measurements were performed at two mammographic unit: a General Electric (GE) Senographe 2000D (which is equipped by a dual bi-metal track target of molybdenum (Mo) and rhodium (Rh) with Rh or Mo filter) and a Selenia Dimensions Genius 3D MAMMOGRAPHY (produced by HOLOGIC, with a fixed tungsten (W) target and a rhodium or silver (Ag) filter). Fig. (5.1) shows the GE (left side) and the Selenia Dimensions Genius 3D MAMMOGRAPHY (from now and on called HOLOGIC, on the right side) unit.

Figure 5.1: GE Senographe 200D (left side) and Selenia Dimensions Genius 3D MAMMOGRAPHY (right side).

The GE unity has a fixed source to image distance of 65 cm while HOLOGIC of 70 cm.
An ionization chamber was used during the measurements: the chamber was a RADCAL Corporation model MDH 1015 plugged into an Accu-Pro dose monitoring system. The chamber has a a dedicated probe for mammography aims (model No. 10X5-6M) with an active volume of 6 cm^3, see Fig. (5.2).

Figure 5.2: Dose monitoring system (left side) and mammography probe of the RADCAL chamber (right side).

The RADCAL chamber (for the devices characterization measurements) was positioned free in air at the center of the detector, 6 cm far from the edge and at 15 cm height from the detector (Fig. 5.3). The compression paddle was positioned as far as possible from the detector.

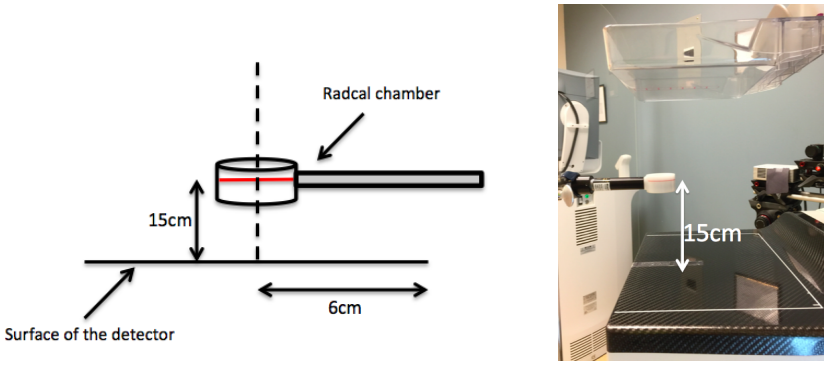

Figure 5.3: Lateral view of the measurements set up for the RADCAL positioning. The probe used is specifically designed for mammographic measurements and has an active volume of 6 cm^3. The red line on the RADCAL is the calibration line.

The phantoms used are shown in Fig. (5.4): the homogeneous phantom is a 50%-50% glandular produced by CIRS (left side in Fig. 5.4) while the heterogeneous phantom is made by a 3D-printer (right side in Fig. 5.4).

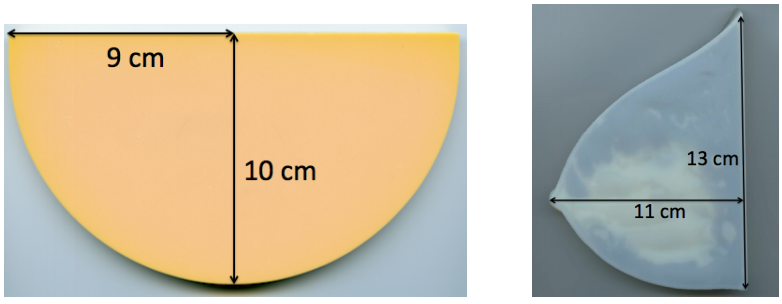

Figure 5.4: On the left side a slice of the 50%-50% homogeneous phantom produced by CIRS. On the right side a slice of the heterogeneous phantom: the whiter inner part is the glandular part (courtesy of Ioannis Sechopoulos).

2.1 Characterization of the two mammographic unit

The automatic anode/filter selection of the two mammographic units was obtained positioning the phantoms on the detector plate. For the homogeneous phantom, the total thickness can be increased by adding phantom slab; thus, it was possible to perform measurements for 2, 4, 6, 8 cm phantom thicknesses. Tab. (5.1) summarizes the parameters selected by the two mammographic unit as a function of the thickness.

System	2 cm	4 cm	6 cm	8 cm
GE	Mo/Mo - 27 kVp	Mo/Mo - 28 kVp	Rh/Rh - 30 kVp	Rh/Rh - 31 kVp
HOLOGIC	W/Rh - 25 kVp	W/Rh - 28 kVp	W/Rh - 31 kVp	W/Ag - 32 kVp

Table 5.1: Automatic parameters selection as function of different breast phantom thickness for General Electric (GE) Senographe 2000D and Hologic Genius 3D MAMMOGRAPHY.

Same procedure was conducted for the heterogeneous phantom: in this case the height of the phantom was about 4 cm and parameters are reported in Tab. (5.2).

System	Heterogeneous Phantom ($\sim 4\ cm$)
GE	Mo/Mo - 29 kVp
HOLOGIC	W/Rh - 28 kVp

Table 5.2: Automatic parameters selection for the heterogeneous phantom.

Half value layers (HVL) measurements were made with the parameters shown in Tab. (5.1) and Tab. (5.2): results are exposed in Tab. (5.3) in mm of aluminum.

System	2 cm	4 cm	6 cm	8 cm	Heterogeneous
GE	0.367	0.388	0.463	0.476	0.395
HOLOGIC	0.495	0.533	0.559	0.615	0.533

Table 5.3: Half value layer in mm of aluminum unity for the two mammographic systems for the two breast phantoms as a function of the thickness.

The heel effect for the two systems was also evaluated moving the RADCAL chamber on the detector in different positions as shown in Fig. (5.5). For each position three measurements were performed and a mean value was calculated (the difference between the measurements was less than 0.1%)

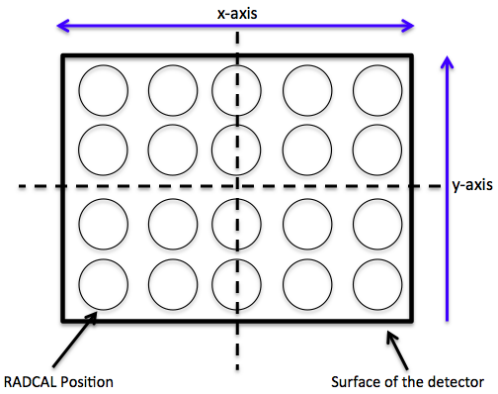

Figure 5.5: The circles represent the different positions of the RADCAL chamber on the detector surface.Three measurements were made for each RADCAL position and then an average number was used.

Fig. (5.6) shows the results for the heel effect measurements as a surface plot: the GE in the upper part and the HOLOGIC at the bottom.

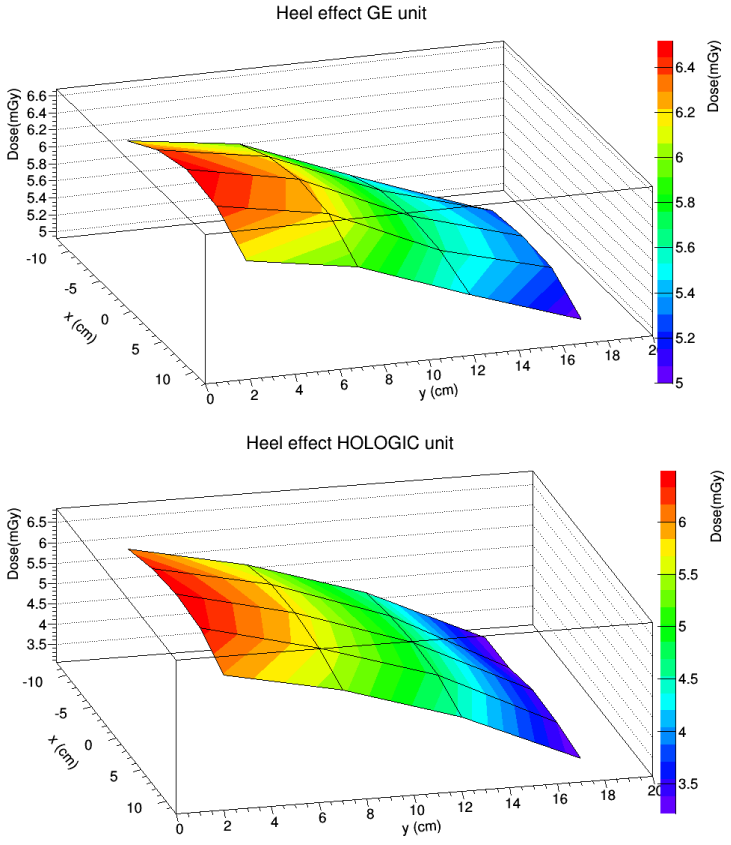

Figure 5.6: Heel effect for the General Electric (GE) Senographe 2000D unity (upper part) and Hologic Genius 3D MAMMOGRAPHY unity (bottom part).

3 Thermoluminescence Dosimetry (TLD)

Thermoluminescence dosimetries (TLDs) are used for dose measurements in several medical applications including radiotherapy, brachytherapy and diagnostic radiology. The selection of the TL material to be used in every applications depends on the specific requirements of the treatments.
For an optimal use of TLDs in medical applications it is important to understand the limitations of each dosimeter.
Many different TL materials are commercially available:

- Lithium Fluoride (LiF) is routinely used for dose measurements (since the effective atomic number of 8.3 is close to water, 8.6);
- Lithium tetraborate ($Li_2B_4O_7$) is more tissue equivalent than LiF (the effective atomic number 7.31) but its stored signal fades rapidly;
- Calcium sulphate ($CaSO_4$) is very sensitive for its high effective atomic number but it is much less tissue equivalent (15.6);
- Calcium fluoride (CaF) has an effective atomic number of 16.9 and it is used for protection dosimetry due to its high sensitivity.

Recently the use of LiF:Mg,Cu,P has emerged as a very interesting TL material with significant advantages over the LiF:Mg,Ti : it has an high sensitivity, an effective atomic number close to water and it can detect low dose.
The presence of impurities appears to be necessary for radiation-induced thermoluminescence. When a TLD chip is irradiated, a fraction of the absorbed energy is stored in the crystal lattice. Then, through a heating system, the TLD is heated and the energy stored is converted into a visible light. A photomultiplier tube (PMT) placed in the TLD reader, collects the light signal converting it into a current.
TLDs used in this study are SCP18815 TLD-100H Chip 3.2 mm x 3.2 mm x 0.38 mm (Thermo Electron Corporation, USA) made from LiF:Mg,Cu,P which has an atomic number of 8.2, low rate of fading and linear dose response (Moscovitch and Horowitz, 2007). The range detection of this dosimeter goes from $1\mu Gy$ to 10 Gy and thus 10-35 times more sensitive than a conventional TLD-100. The reading of the dosimeters was accomplished with a Harshaw TLD 3500 TLD-reader (with Nitrogen flowing at 30 psig).
The Time-Temperature Profile (TTP) of a chip starts with a preheat period (135° C for 10 sec), followed by acquisition at $10°C/s$ up to $240°C$ for 23 1/3 sec and annealing at $240°C$ for 10 sec (as suggested by the manufacturer).
The annealing of the TLD-100H material can be a delicate operation in that it is highly temperature dependent. For this reason it was decided to proceed as follows: before performing any measurements each chip underwent to a readout cycle (which has an annealing part lasting 10 sec). This puts the chips into a "quenched" state. A true annealed state is only obtainable after a full annealing cycle in an external oven in that only this method assures a full reset of the chip. However, the annealing protocol we performed is consistent with all the measurements and all the chips were always putted into the quenched state before using.
The PMT and LIGHT stability of the reader were checked before starting and at the end of the entire reading process.

A typical Glow Curve is shown in Fig. (5.7): a mean peak is present with no others peaks at lower channels. Changes over time of the Glow Curve was checked and no dependency was found. All the 200 channels were used for measurements.

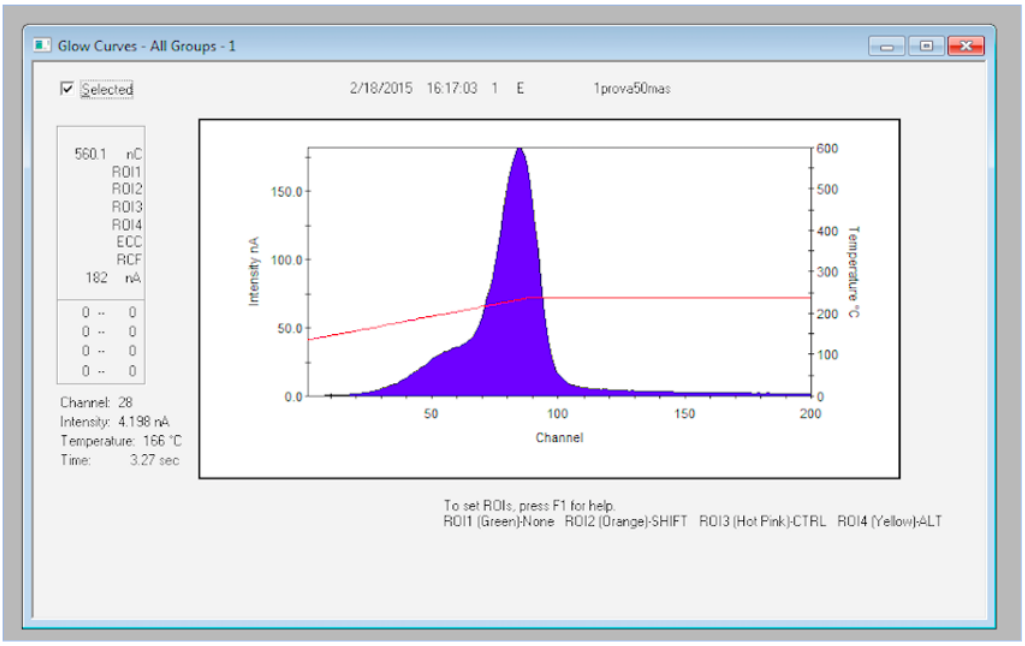

Figure 5.7: Glow Curve obtained with the TLD-100H 48h after irradiation.

All the chips were named with a progressive number in order to unequivocally identify each TLD.

3.1 TLD Characterization

Sensitivity

The chips were annealed, following the procedure previously described, before all the measurements.
The sensitivity of the chips was tested by exposing all the TLDs free in air to a dose of about 11 mGy (with the GE system, Mo/Mo 27 kVp 90 mAs) with the setup shown in Fig. (5.8). The RADCAL ionization chamber (Fig. 5.2) was used for dose monitoring.

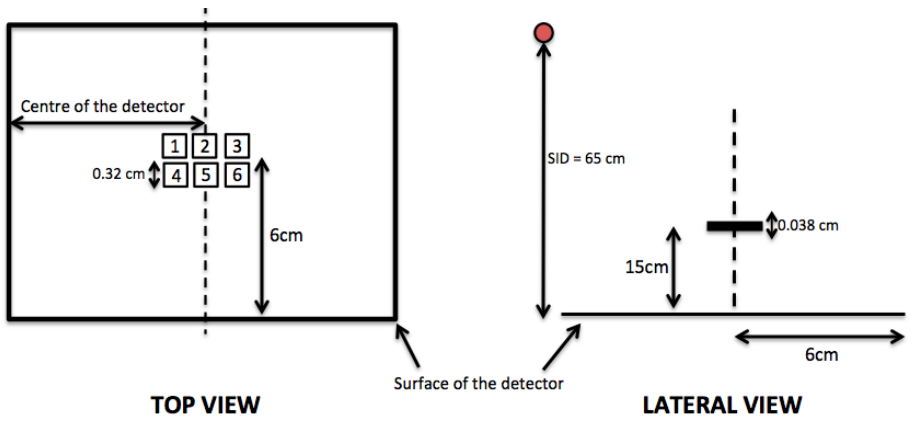

Figure 5.8: Schematic setup of the TLD irradiation: the TLD chips (0.32 cm x 0.32 cm x 0.038 cm) were positioned at the center of the detector (6 cm far from the detector border) and at 15 cm height from the detector plate. Each measurement was done irradiating 6 chips at the same time. The Source to Image Distance (SID) is 65 cm.

After 48h from the irradiation, the chips were read by the TLD reader with the TTP already described. The individual sensitivity (S) is evaluated as the ratio between the single charge collected by each TLD divided by the mean charge of the all TLD chips.
The results of the sensitivity distribution are shown in Fig. (5.9): a mean value of 1 is found. As noticed in Moscovitch and Horowitz (2007), the high sensitivity of the TLD-100 material can lead to a variation in the single TLD output up to 15% due to several reasons: not-exactly same TLD material (i.e. crystal impurities), reading procedure, etc. This trend was confirmed by our measurements where a difference of 14% was found.

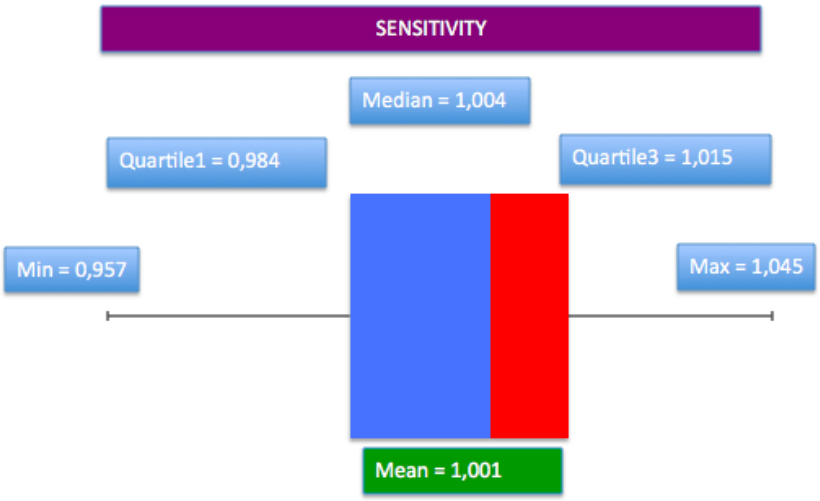

Figure 5.9: Boxplot of the sensitivity for the TLDs chips.

Calibration procedure

The calibration measurements were performed using the setup shown in Fig. (5.8): three TLDs were placed 6 cm far from the detector edge. An average value was obtained from the three TLDs exposed and a calibration factor (K) was obtained from a linear fit (this is justified as in the energy range of 8 - 35 the response of TLD-100H can be considered linear (Moscovitch and Horowitz, 2007).
As the spectrum/filter and the voltage applied to the calibration measurements are the same of the phantom measurements no energy dependence factors need to be introduced.

Dose evaluation

The dose (D_i) measured by the i-TLD was evaluated following the formula:

$$D_i = R_i \cdot S_i \cdot K_i \tag{5.1}$$

where R_i is the i-TLDreader output (nC), S_i (adimensional) is the i-individual TLD sensitivity factor and K_i (mGy/nc) is the calibration factor. The combined percentage uncertainty (u_i) is:

$$u_i(\%) = \sqrt{u_R^2 + u_S^2 + u_K^2 + u_{RADCAL}^2} \tag{5.2}$$

where u_R^2 is the reader uncertainty (5% given by the manufacturer), u_S^2 is the sensitivity combined uncertainty (in the order $5\% - 6\%$), u_K^2 is the calibration-factor uncertainty (in the order 10^{-8}) and u_{RADCAL}^2 is the RADCAL uncertainty (5% given by the manufacturer).
The overall combined uncertainty is between 8%-10%.

4 Metal oxide semiconductor field effect transistor (MOSFET)

Metal oxide semiconductor field effect transistor (MOSFET) dosimeters were initially developed for radiotheraphy ((Rosenfeld *et al.*, 1995), (Butson *et al.*, 1996) and (Ramani *et al.*, 1997)) and then applied also to diagnostic radiology (Scalchi and Francescon (1998), Bower and Hintenlang (1998) and Peet and Pryor (1999)).
The main characteristics of these detectors are the small size, tissue equivalence, an on-line readout possibility, fast dosimeter response and an independence of response from the dose rate. These characteristics make them convenient for medical applications and a good candidate for measuring dose in mammography. However, MOSFETs have a drawback in their limited lifetime, which is due to the accumulated radiation damage (the device become inoperable with an accumulated dose that correspond to 20000 mV).
Fig. (5.10) shows a typical MOSFET orientation during exposure and its internal structure.

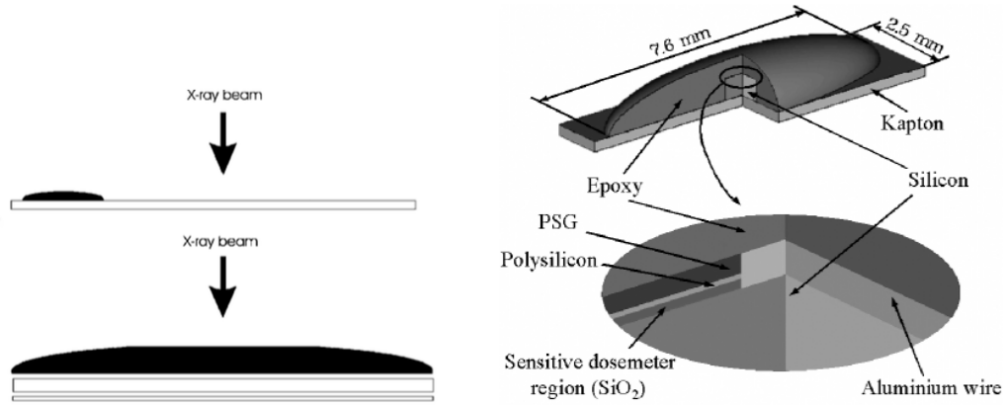

Figure 5.10: Typical clinical orientation of the MOSFET to the x-ray beam (left side, (Benevides and Heintenlang, 2006)) and schematic diagram of the dosimeter structure (right side): three thin layers are sandwich between the silicon substrate and the epoxy cover. The sensitive dosimeter volume (SiO_2) is located under two thin layers (Wang *et al.*, 2005).

The current study uses the high-sensitivity MOSFET model TN-1002RD (Best Medical Canada Ltd., 413 March Road, Ottawa, ON K2K 0E4, Canada) for use in clinical mammography. The dosimeters were plugged in the reader module with the Patient Dose Verification System, model TN-RD-16, as shown in Fig. 5.11.

Figure 5.11: Equipment for the MOSFET dosimeters.

Two bias sensitivities supply can be selected in the reader in order to cover a wide range of doses with optimal reproducibility. In this study the High Sensitivity was chosen as it is specific for low dose applications. In this configuration the sensitivity (as declared by the manufacturer) is 9 mV/cGy.
The dosimeter gives the response in term of mV: MOSFET measures the radiation dose through a shift in the device threshold. Thus, a MOSFET energy calibration is required for obtaining the calibration factors (in terms of mV/mGy) which gives the dose in radiation units following the equation

$$D = \frac{mV}{CF} \tag{5.3}$$

where the CF is the calibration factor in terms of mV/mGy.
Several measurements were performed at the two mammography units (GE and HOLOGIC) to better characterize the MOSFETs.

4.1 MOSFET Characterization

Linearity

The experimental set up is shown in Fig. (5.12): the MOSFET were exposed free in air with the epoxy-side perpendicular and facing the x-ray beam (as in Fig. (5.10) left side).

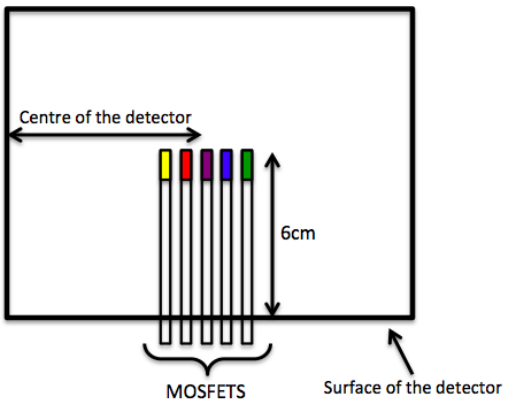

Figure 5.12: Top view of the experimental setup used for the MOSFET measurements: the MOSFET were positioned at the centre of the detector and 6 cm from the detector edge. The measurements were performed free in air.

The target-filter combinations taken into account were those previously exposed in Tabs. (5.1 and 5.2).
To cover the range used in clinical mammography the current-time product (mAs) was selected in the interval range 80 - 320 mAs.
Five exposures were taken at each tube potential (kVp) and tube current-time (mAs). Fig. (5.13) and Fig. (5.14) show the dosimeter response for GE and HOLOGIC unity respectively as function of the increasing tube current-time: in the graphs, the mean value is taken averaging the five exposures while the error bars represent the standard deviation. The dosimeters show a linear response to exposure (with a correlation coefficient $r^2 > 0.99$).

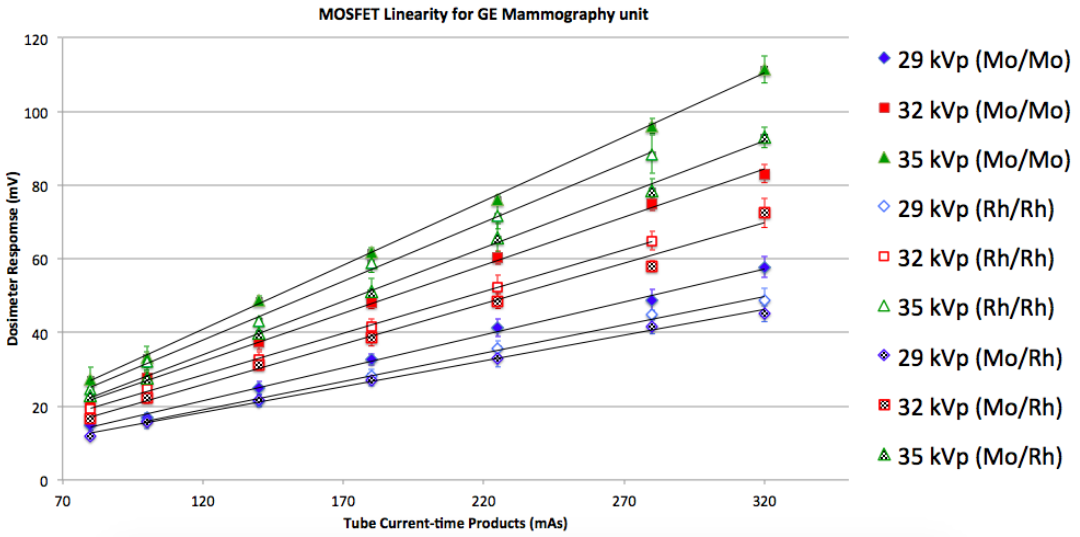

Figure 5.13: Linearity of the MOSFET response for the GE unit as function of the tube current-time.

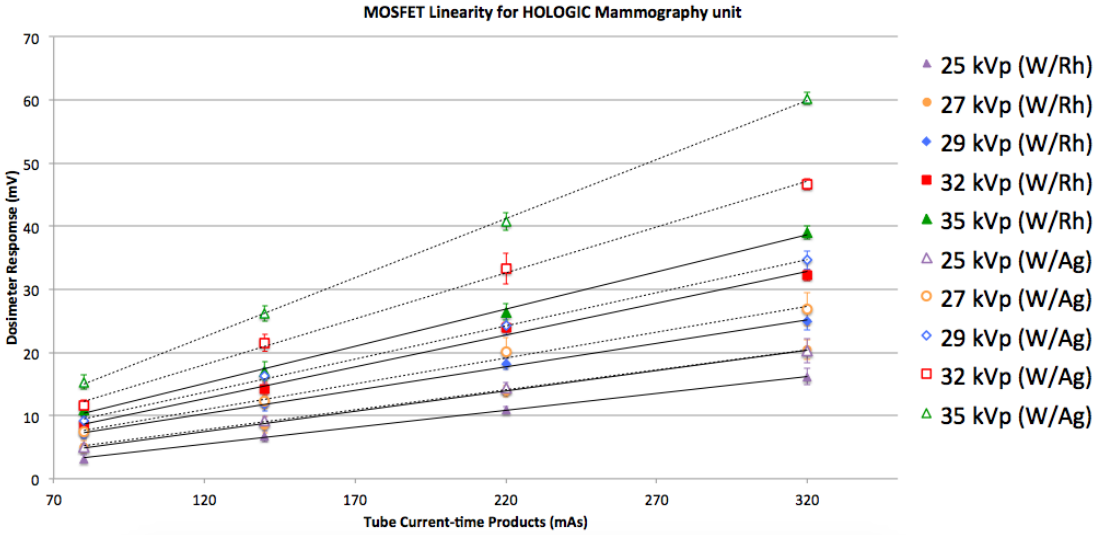

Figure 5.14: Linearity of the MOSFET response for the HOLOGIC unit as function of the tube current-time.

A trend consistent with previoulsy pubblished work (Dong *et al.* (2002) and Benevides and Heintenlang (2006)) was found. However, a comparison of our results with the ones of those papers can not be directly made as the experimental assessment as not exactly the same.

A very good linearity for MOSFET is verified in the mammographic dose range.

Sensitivity

Sensitivity measurements of MOSFET were performed in a similar setup as already described in Fig. (5.12): in these measurements the RADCAL ionization chamber was used as a reference exposure as in Fig. (5.3).
Dosimeters and RADCAL chamber were positioned facing the x-ray beam, exposed free in air with the compression paddle positioned as far as possible from the detector surface to avoid any scatter contribution. Target-filter combinations previously described were taken into account.
Sensitivity was measured as mV over cGy; results are shown in Figs. (5.15, 5.16, 5.17, 5.18, 5.19).

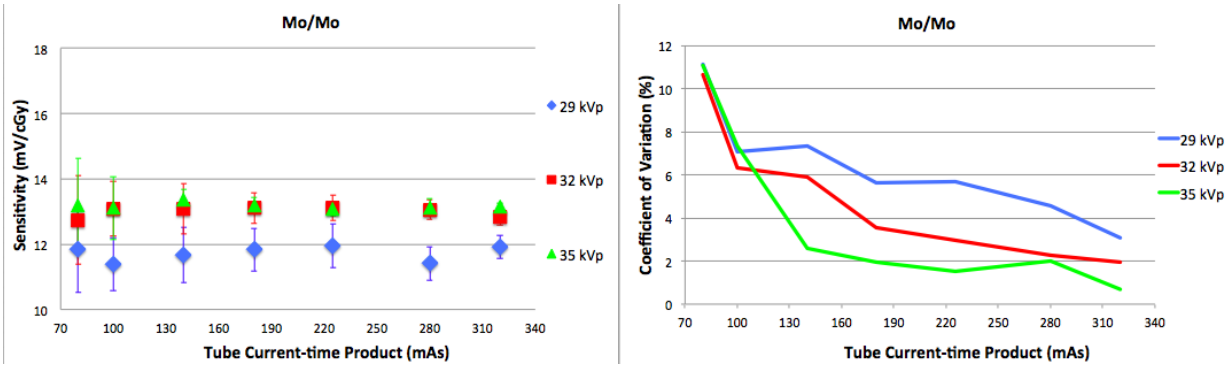

Figure 5.15: The sensitivity response (mV/cGy) for the Mo/Mo anode/filter combination (left graph): it is possible to notice that the sensitivity remained constant. However, at the increasing of the tube output there was a decreasing of the coefficient of variation (right graph).

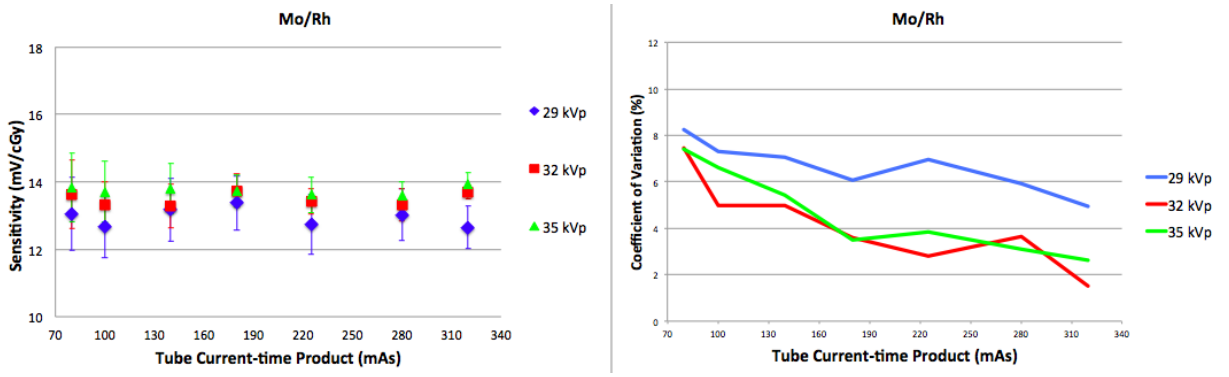

Figure 5.16: The sensitivity response (mV/cGy) for the Mo/Rh anode/filter combination (left graph): it is possible to notice that the sensitivity remained constant. However, at the increasing of the tube output there was a decreasing of the coefficient of variation (right graph).

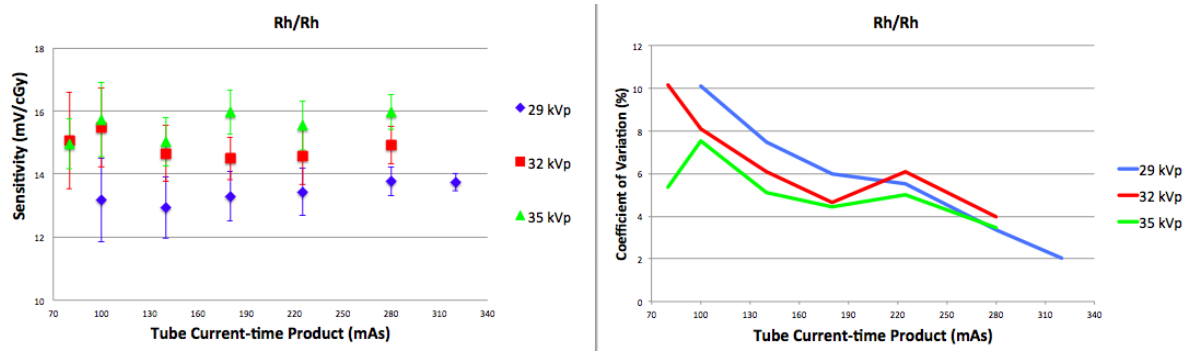

Figure 5.17: The sensitivity response (mV/cGy) for the Rh/Rh anode/filter combination (left graph): it is possible to notice that the sensitivity remained constant. However, at the increasing of the tube output there was a decreasing of the coefficient of variation (right graph).

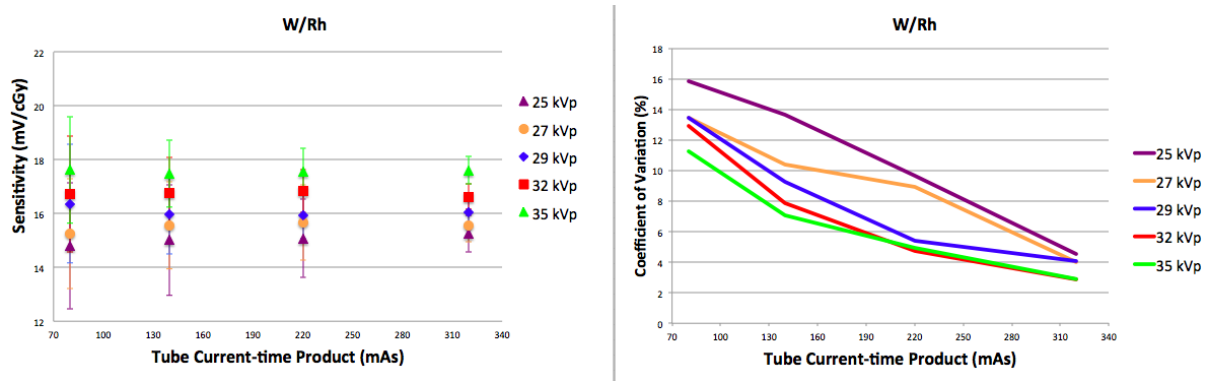

Figure 5.18: The sensitivity response (mV/cGy) for the W/Rh anode/filter combination (left graph): it is possible to notice that the sensitivity remained constant. However, at the increasing of the tube output there was a decreasing of the coefficient of variation (right graph).

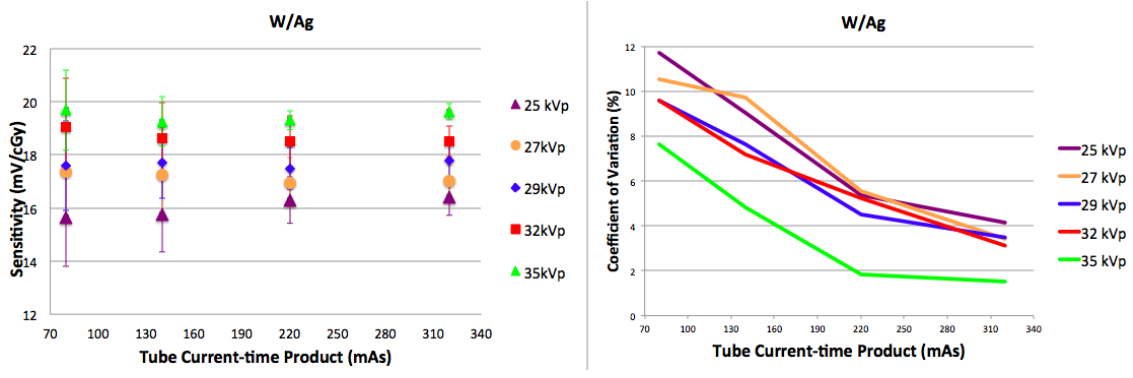

Figure 5.19: The sensitivity response (mV/cGy) for the W/Ag anode/filter combination (left graph): it is possible to notice that the sensitivity remained constant. However, at the increasing of the tube output there was a decreasing of the coefficient of variation (right graph).

Fig. (5.20) shows the MOSFET sensitivity as function of the tube potential (left side) and for the different anode/filter combinations tested (right side).

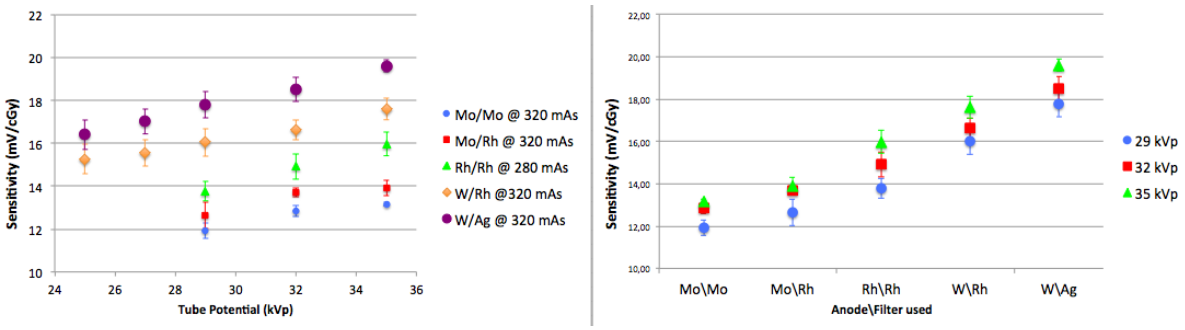

Figure 5.20: The sensitivity response (mV/cGy) for MOSFET in mammography energy ranged 25 to 35 kVp (left graph). On the right graph sensitivity as function of different anode/filter combinations is shown.

The sensitivity of MOSFET remains constant at the increasing of exposure. However, the precision of measurements increased at higher mAs. Low mAs means low MOSFET input signal and, in this case, MOSFET may be considered unstable.

5 Radiochromic Films (GAF)

The development of an accurate dosimetry method is a crucial issue when monitoring the dose delivered during diagnostic radiology procedures. TLDs and MOSFETs dosimeters are considered point dose methods and assume the existence of an homogeneous dose distribution within the measured volume.
Recently the use of films as dose monitoring devices is increasing in the radiology area (de Denaro *et al.* (2007) and Tominaga *et al.* (2011)).
Each radiology application has its own suitable radiochromic films (e.g types HD-810, MD-55-2, RTQA, XR-RV2, EBT, XR-QA, XR-QA2).
Gafchromic^{TM} XR-QA2 (Ashland Inc, Wayne, NJ) are specifically designed for radiology and dosimetry applications in a dose range of 1 mGy to 200 mGy.
The model XR-QA2 is a new model which replaced XR-QA. The main characteristics of Gafchromic XR-QA2 films are presented in (Giaddui *et al.*, 2012).
Gaf XR-QA2 is a reflective-type film which consists of five layers (Fig.5.21): 97 μm thick yellow polyester, 15 μm thick acrylic adhesive layer, 25 μm thick active layer, 3 μm thick surface layer and 97 μm thick opaque white polyester. The films dimensions are 25 cm x 30 cm.
The active layer of the films nominally consist of H, Li, C, N, O, S, Ba and Bi. The inclusion of several high Z elements increases its sensitivity to low x-ray energies as the cross section for the photoelectric effect increases (Brady *et al.*, 2010).

The use of radiochromic films offer several advantages as bi-dimensional dosimetry, thinness and ruggedness (Tomic *et al.*, 2014). On the other side, the use of Gaf requires specific care: the films have to be managed using gloves for avoiding fingerprint, need to be calibrated at all energies used and depend on the environmental light and of the light scanner etc.

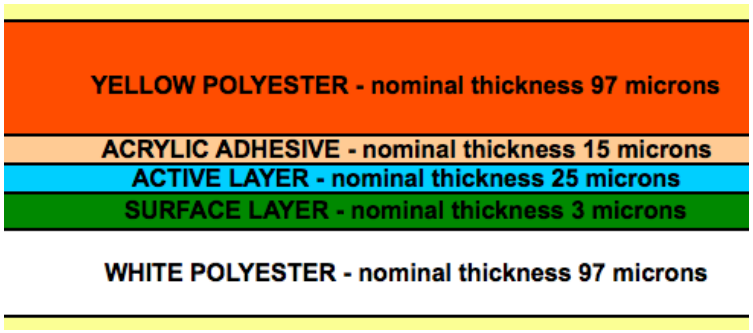

Figure 5.21: Schematic representation of Gaf layers.

5.1 Characterization measurements

Scanner and image acquisition

An Epson Perfection V750 Pro flatbed document scanner was used to scan the films. On the scanner control panel all the automatic image adjustment features were disabled. The resolution was set to 72 dpi (which means that 100 pixels correspond approximately to 3.5 cm) in the 48 bit RGB mode (16 bit per channel). Data were saved in uncompressed tagged image file format (TIFF). Only the red component was extracted from the image file, since the sensitivity is higher in red. Before each acquisition the scanner was warmed up. An analysis of the pixel value stability shows that at least five empty scans are needed to warm up the scanner light (Fig. 5.22).

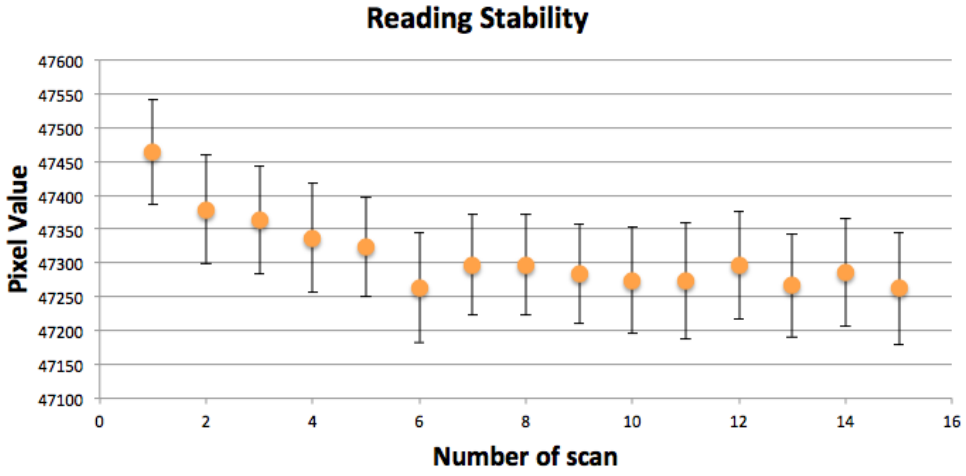

Figure 5.22: Evaluation of the reading stability: pixel value (on y-axis) are reported as a function of the number of scans (on x-axis).

Positioning the gaf films directly on the scanner glass can cause the "Newton Rings" to appear (see Fig. 5.23).

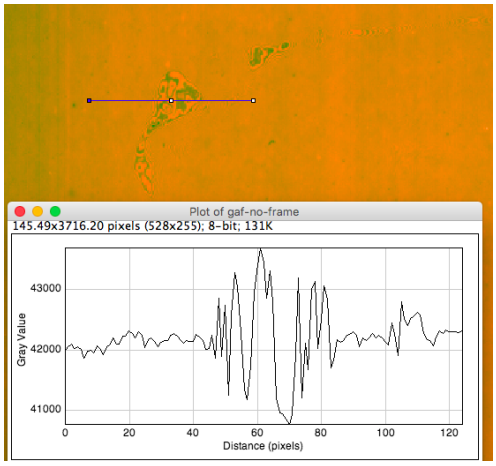

Figure 5.23: Newton rings effects: the plot profile obtained using ImageJ software shows the typical Netwton rings interference pattern.

Newton rings are due to a constructive/destructive interference between reflected/refracted rays that are visible on the films. In order to prevent this effect a thin (< 2 mm thick) simple paper frame was used to prevent contact with glass.
The gaf was scanned with the setup shown in Fig. (5.24): two pieces of Plexiglas where positioned above the gaf for increasing the film adherence and reducing the non-homogeneity. If the Plexiglas is not used, a lever effect due to the scanner hinge can be found: in the scanning direction the difference (top-bottom) goes up to 4-5 %, which is higher if compared to the 1-2% for the Plexiglas setup.

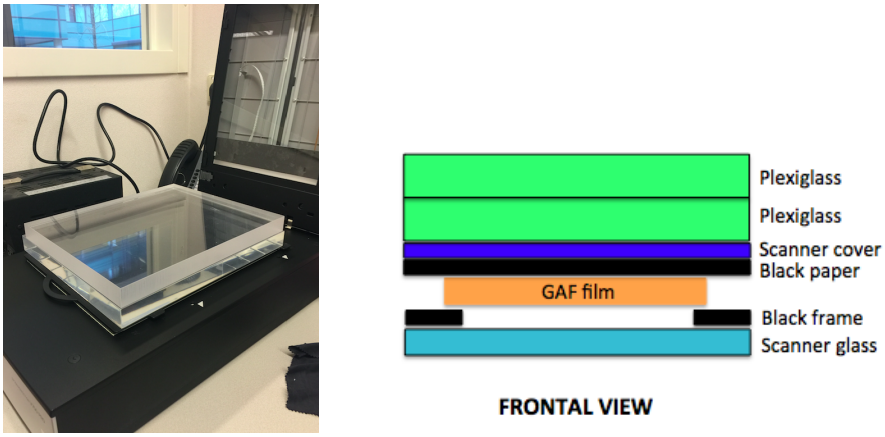

Figure 5.24: Scannig gaf setup (description from top to bottom): two plexiglass pieces, used for adherence purpose; scanner cover and black paper for avoiding reflection; gaf film; black frame in order to prevent the Newton's rings.

The scanner uniformity was checked using a white paper covering the entire scan bed. The advantage of using paper instead of other materials is that paper has a stable behavior over time (Butson *et al.* (2011) and Alnawaf *et al.* (2012)).
Horizontal and vertical profiles were calculated with ImageJ software in the region of interest, ROIs, (7 for horizontal and 6 for vertical) shown in Fig. (5.25).

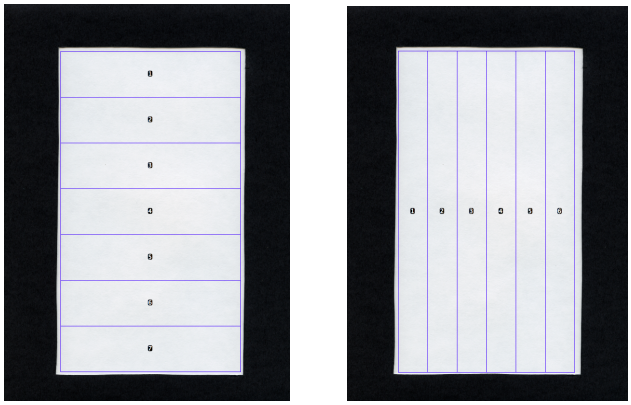

Figure 5.25: On the left side the 7 horizontal ROIs (372 x 95 $pixels^2$); on the right side the 6 vertical ROIs (60 x 666 $pixels^2$). The mean value was calculated within each ROI.

The results (normalized to the mean pixel value of the whole useful scanned area) show a maximum vertical nonuniformity of 3%(Fig. 5.26) and a maxium horizontal nonuniformity of 2% (Fig. 5.27). These results are in agreement with the literature (Menegotti *et al.* (2008) and Bradley *et al.* (2011)).

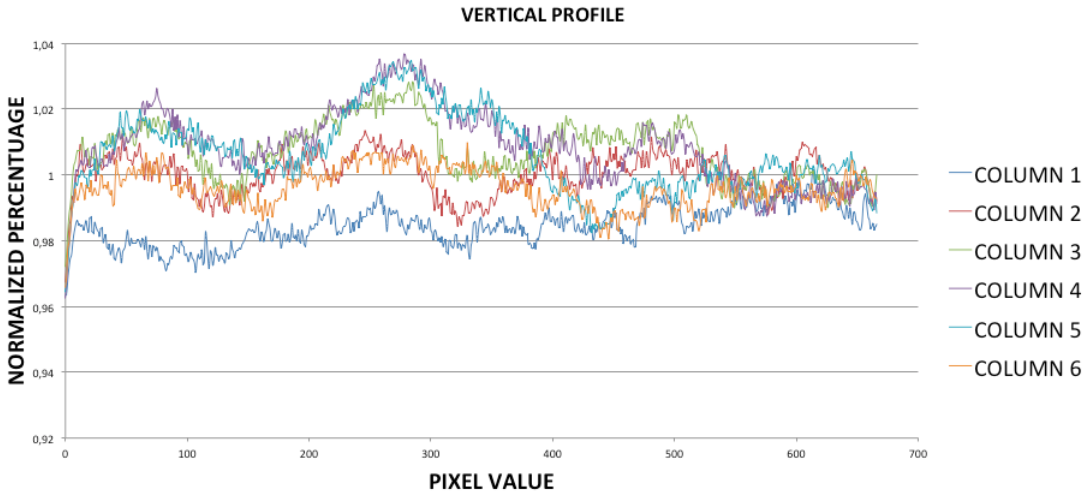

Figure 5.26: Normalized vertical profile.

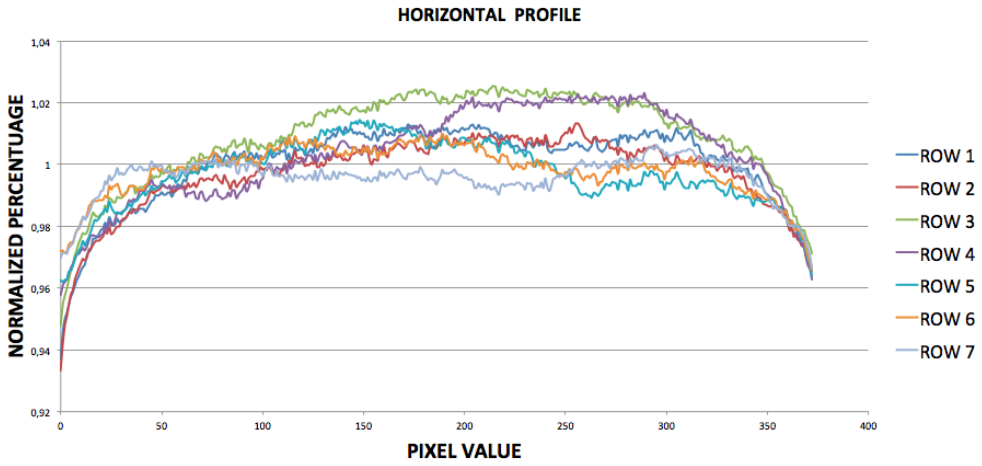

Figure 5.27: Normalized horizontal profile.

Dose evaluation

The evaluation of the Gaf response was performed following the procedure described in (Tomic *et al.*, 2010) and (Tomic *et al.*, 2014). Radiation induced changes in reflectance throughout a visible turning black of the film: this is proportional to the absorbed dose. The pixel values (PV) change, in a rectangular ROI, was evaluated as follows:

$$\Delta R = R_{before} - R_{after} = \frac{PV_{before}}{2^{16}} - \frac{PV_{after}}{2^{16}} \tag{5.4}$$

A control film piece (not irradiated) was used to quantify effects other than radiation exposure (e.g. scanning light, visible light, etc.). This piece was handled in the same way as the other and scanned before and after irradiation. The difference in reflectance of the control film piece is described as:

$$\Delta R^{control} = R^{control}_{before} - R^{control}_{after} = \frac{PV^{control}_{before}}{2^{16}} - \frac{PV^{control}_{after}}{2^{16}} \tag{5.5}$$

The net change in reflectance of the film gaf, $net\Delta R$, was obtained by subtraction between Eq. (5.4) and Eq. (5.5) as follows:

$$net\Delta R = \Delta R - \Delta R^{control} \tag{5.6}$$

All films were scanned after 48h from the irradiation.

Gaf Additive

The Gaf additive was checked dividing an entire sheet of gaf into small pieces of 4 cm x 4 cm (a total of 42 pieces). The film section size was selected in order to avoid the mechanical stress along the cutting edge of the films. Each piece was numbered to be unequivocally determinate. A rectangular ROI of 1 cm x 1 cm was selected inside the image and the mean and the standard deviation (over three pieces) were calculated to be used within the Eq. (5.6). The films were

irradiated (once at the time) as shown in Fig. (5.28) with the orange part facing the x-ray tube: 10 mGy and 20 mGy were delivered in three different modes: single shot, 10 shots and 20 shots. The RADCAL chamber was used as dose reference.

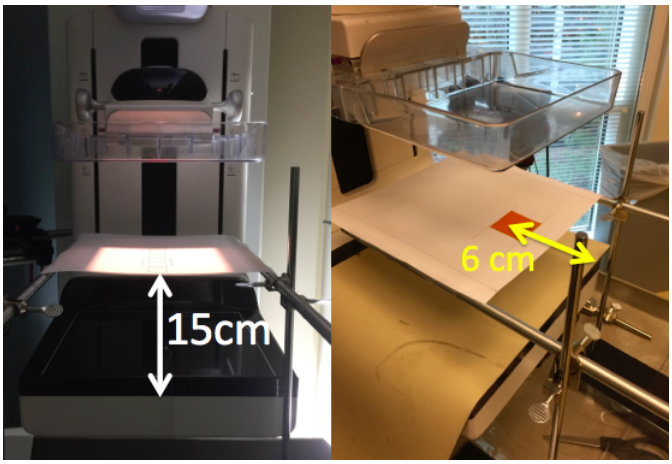

Figure 5.28: Setup of the gaf exposure: each piece was positioned at 15 cm height form the detector and 6 cm far from the edge. The measurements were performed free in air using a white paper as a gaf support and the RADCAL chamber for dose monitoring.

Results (Fig. 5.29) show no difference in the gaf response, confirming the additivity of the film.

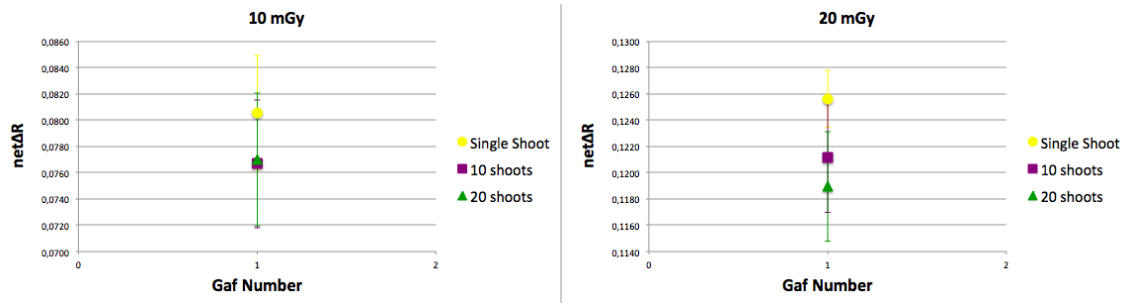

Figure 5.29: On the left side the results for the 10 mGy while on the right side for 20 mGy: all the values are within one standard deviance .

Calibration procedure

Calibration curve was obtained plotting the air kerma, K^{film}, as a function of the corresponding film response, $net\Delta R$, see Eq.(5.6). Three pieces of gaf were exposed to the same air kerma (in a similar setup as shown in Fig. 5.29) and the average values were obtained. For each measurement (free-in-air or inside phantom) specific calibration curves were obtained.
The choice of the analytical form for the calibration curves was based on the criteria exposed in Tomic *et al.* (2010): (i) the fit function that has to be monotonically increased; (ii) highest r^2 values obtained by the fitting program (Table Curve 2D v5.01, SYSTAT Software Inc.). Two possible fitting functions obtained satisfactory (i.e. high r^2) results for the data fitted:

$$K^{film} = a \cdot net\Delta R \tag{5.7}$$

$$K^{film} = a + b\left(\frac{net\Delta R}{ln(net\Delta R)}\right) \tag{5.8}$$

where a and b are fit parameters which vary for each measurement.
The best fitting function was selected plotting the relative K^{film}, calculated as a relative difference between calculated (using Eqs. 5.7 or 5.8) and measured air kerma (using the RADCAL chamber). The uncertainty analysis was performed following Tomic *et al.* (2010) who separated the experimental contribution (due to the uncertainty of the measured air kerma) and the parameter fit uncertainty.
Figs. (5.30, 5.31, 5.32, 5.33, 5.34) show the results when applying a linear fit function (Eq. 5.7) in the case of the 4cm homogeneous phantom exposed to the GE spectrum (MO/MO 28kVp).

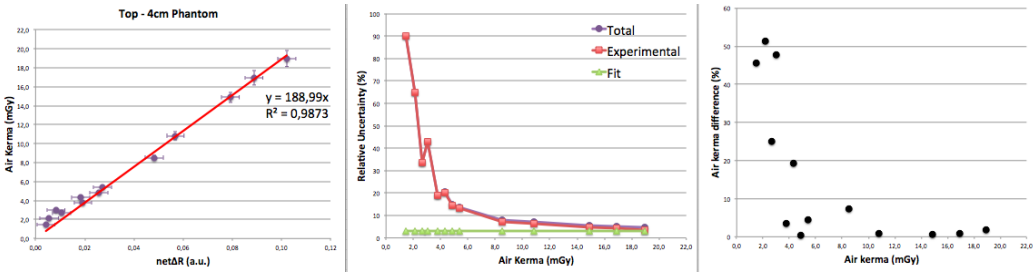

Figure 5.30: Results of analysis for the radiochromic films. On the left graph: calibration curve; middle graph: total one sigma uncertainty (with the two contributions); on the right: relative error.

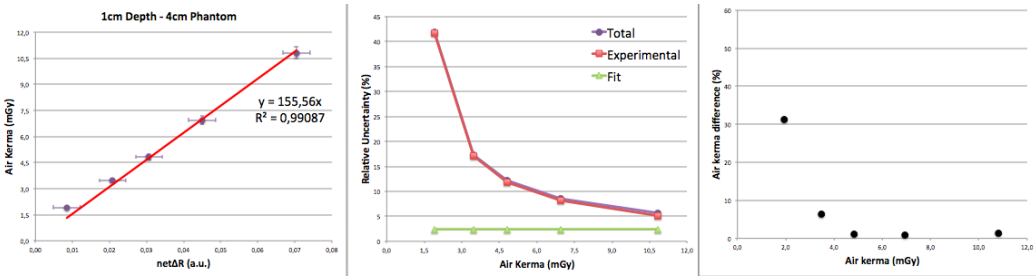

Figure 5.31: Results of analysis for the radiochromic films. On the left graph: calibration curve; middle graph: total one sigma uncertainty (with the two contributions); on the right: relative error.

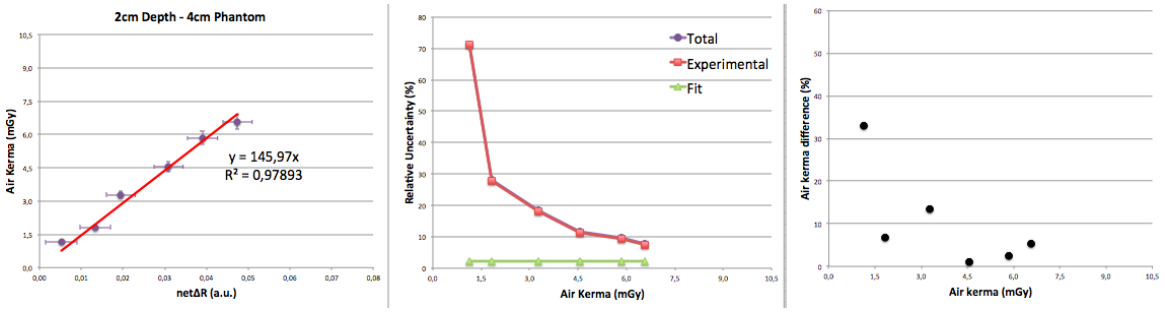

Figure 5.32: Results of analysis for the radiochromic films. On the left graph: calibration curve; middle graph: total one sigma uncertainty (with the two contributions); on the right: relative error.

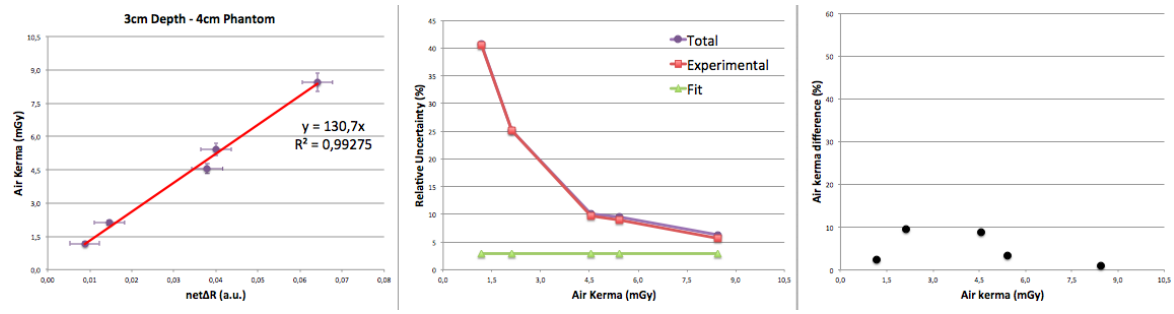

Figure 5.33: Results of analysis for the radiochromic films. On the left graph: calibration curve; middle graph: total one sigma uncertainty (with the two contributions); on the right: relative error.

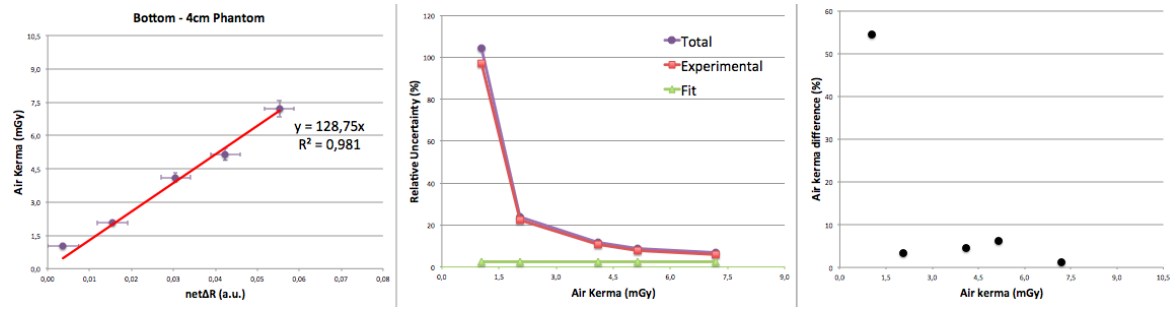

Figure 5.34: Results of analysis for the radiochromic films. On the left graph: calibration curve; middle graph: total one sigma uncertainty (with the two contributions); on the right: relative error.

Figs. (5.35, 5.36, 5.37, 5.38, 5.39) show the results when applying the fit function shown in Eq. (5.8) in the case of the 4cm homogeneous phantom exposed to the GE spectrum (MO/MO 28kVp).

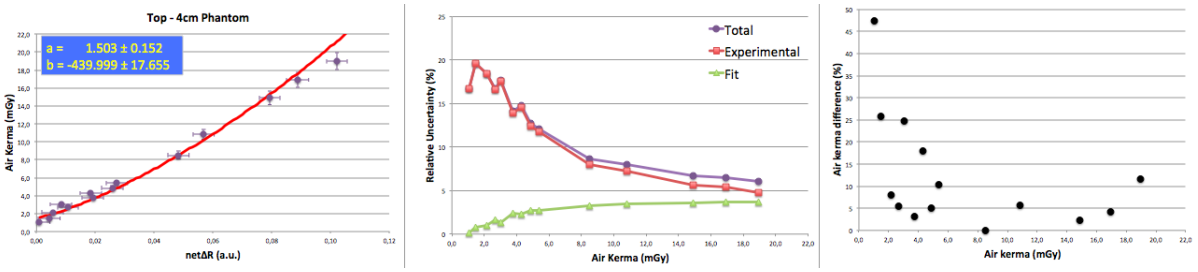

Figure 5.35: Results of analysis for the radiochromic films. On the left graph: calibration curve; middle graph: total one sigma uncertainty (with the two contributions); on the right: relative error.

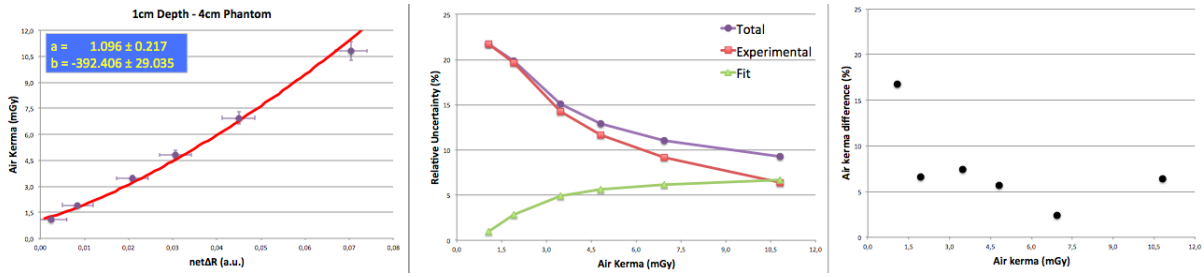

Figure 5.36: Results of analysis for the radiochromic films. On the left graph: calibration curve; middle graph: total one sigma uncertainty (with the two contributions); on the right: relative error.

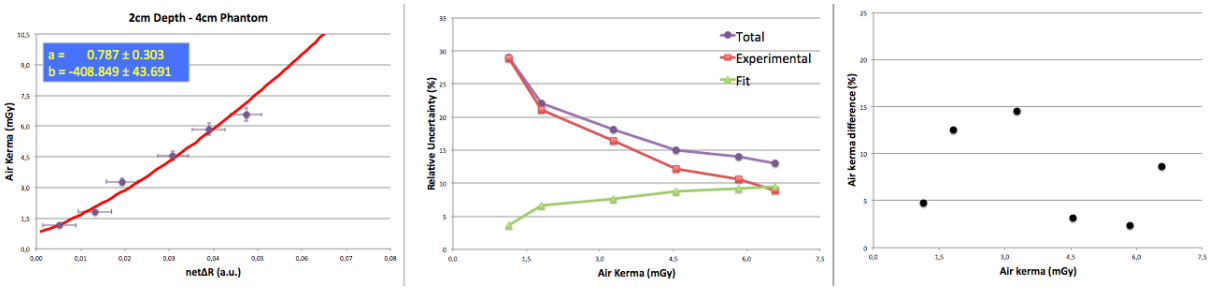

Figure 5.37: Results of analysis for the radiochromic films. On the left graph: calibration curve; middle graph: total one sigma uncertainty (with the two contributions); on the right: relative error.

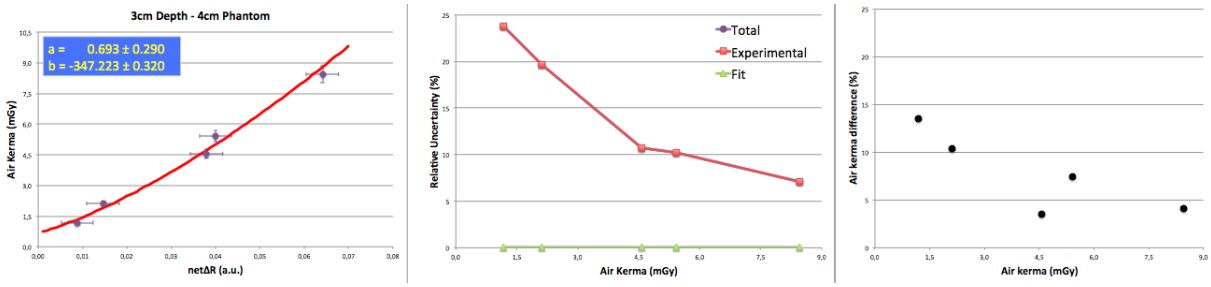

Figure 5.38: Results of analysis for the radiochromic films. On the left graph: calibration curve; middle graph: total one sigma uncertainty (with the two contributions); on the right: relative error.

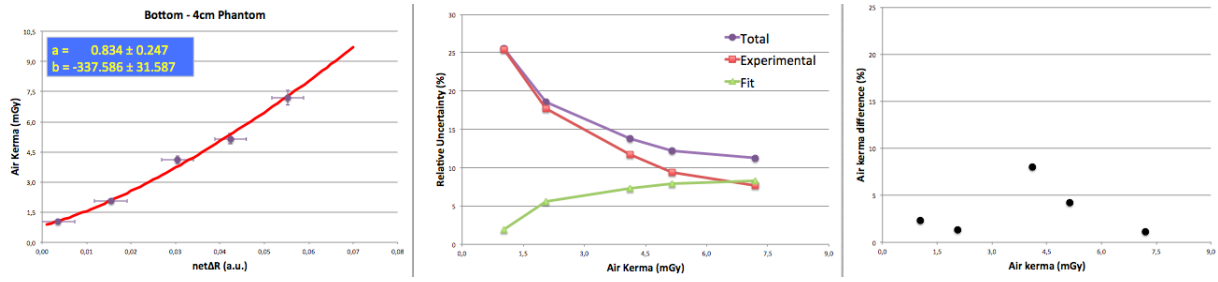

Figure 5.39: Results of analysis for the radiochromic films. On the left graph: calibration curve; middle graph: total one sigma uncertainty (with the two contributions); on the right: relative error.

Results for the fit equation (5.8) show a lower uncertainty (in a percentage range of 30%-10%) for the low air kerma region (1mGy - 6mGy) compared to results of the linear fit (100%-10%) in the same dose range. However, when the air kerma delivered increased (> 6mGy), the uncertainty on the linear equation rapidly decreased to a value lower than 10%, while the uncertainty of Eq. (5.8) remained stable to 10% and then slowly decreased.
This trend is comparable to previous works (Tomic *et al.* (2010), Tomic *et al.* (2014), Di Lillo *et al.*, 2015) where the increased of the delivered air kerma (> 5mGy) results in a total uncertainty lower than 10%.
When the radiochromic films were used inside phantoms for the dose map distribution the delivered air kerma was always higher than 5 mGy, in order to have an uncertainty lower than 10%.

6 Monte Carlo code

A pre-existent Monte Carlo (MC) code (Sechopoulos *et al.*, 2006), based on the toolkit GEANT4, was modified to match the experimental conditions exposed in the previous sections.
All spectra, with the modulation due to the measured heel effect (Fig 5.6), were implemented in the *G4PrimaryGenarationAction* class.
The MC code was specifically modified in order to implement a voxelized geometry corresponding to the image of the 3D printed phantom (Fig. 5.4 right side).
The simulations output is a matrix file in which each entrance is the dose deposited.
As all the dosimeters are calibrated respect to the RADCAL chamber (which gives the air kerma), the material implemented in the simulation is air.

7 Preliminary results for the 4 cm homogeneous phantom

Preliminary results obtained for the 4cm homogeneous phantom are exposed. Only the depth of 1cm is presented while same analyses will be extended to all others cases.
In order to have TLDs and MOSFET at the same place, a fixed matrix displacement was used, as shown in Fig. (5.40).

Due to the symmetry of the measurements in respect to the central line of the detector, the dosimeters were positioned only in one half of the phantom. This hypotesis was previously

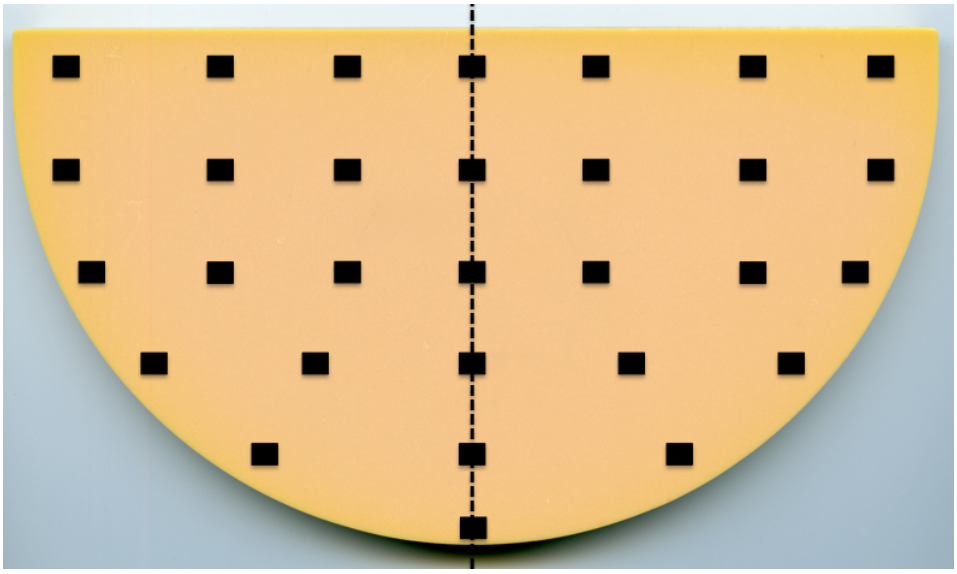

Figure 5.40: Dosimeters experimental displacement on the slab phantom: each black square correspond to the position where a TLD or a MOSFET was positioned.

verified with three full dosimeter irradiation and the results were within the experimental uncertainties.
Results are shown in Fig. (5.41).

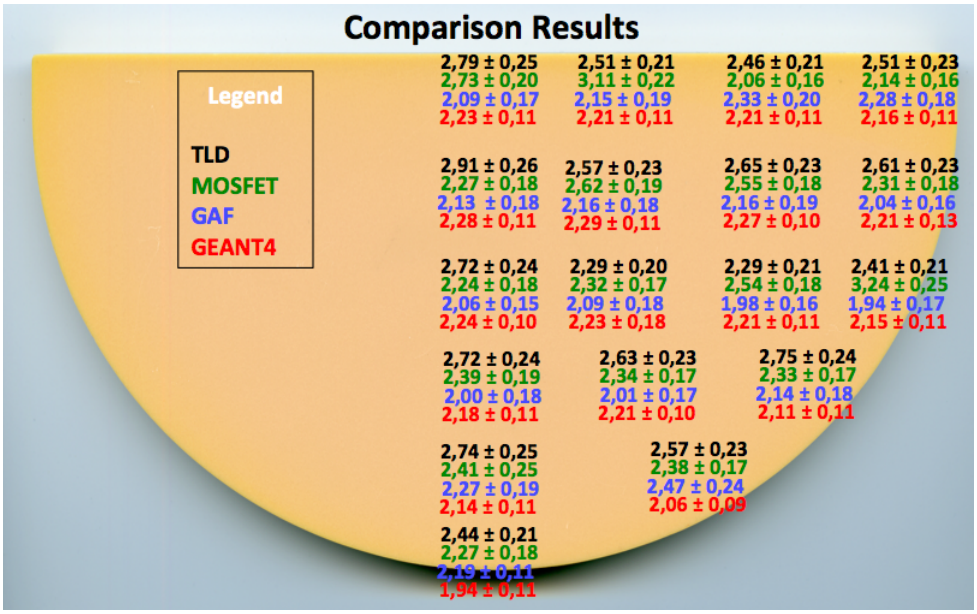

Figure 5.41: Comparison betweeen dose obtained with TLD (black), MOSFET (green), GAF film (blue) and MC (red). The uncertainty correspond to one standard deviation.

The uncertainty on the MC results is about 5%, which is not realistic for MC data: this is due to the lower cross-section interaction for photons in air. Hence, firstly, a higher number of

primary events need to be simulated in order to decrease the statistics uncertainty. However, in this preliminary phase, some conclusions can be derived.
MC, MOSFET and GAF show a good agreement: the majority of the measurements (13/18) are compatible within one standard deviation while all measurements are compatible within two standard deviations.
TLDs show an over-response for the majority of the measurements. However all the results are still compatible within 2 standard deviations and 55% of the measurements are within one standard deviation.
These results show that all the characterization measurements performed (i.e. calibration curves, sensitivity, sensibility, response, etc.) give compatible results with different dosimetric techiniques.
Analyses will be extended to all the cases shown in Tab. (5.1) with the aim to obtain a dose map for all the devices and MC also for the heterogeneous breast phantom.

Chapter 6

Monte Carlo Simulations

Monte Carlo (MC) methods are a broad category of computational algorithms based on the generation of pseudo-casual numbers for obtaining numerical results. The MC approach is widely used both for finding numerical solutions to mathematical problems or for modeling experimental measurements. Thanks to MC simulations it is possible to obtain physical information not available in any others ways such as particles position, momentum direction, energy delivered etc.
This chapter briefly introduces the main features of GEANT4 MC software: a simulation toolkit extensively employs in medical physics and used within the SYRMA-CT project.
The MC code developed in this work is then deeply analyzed: the structural computational choices are exposed and discussed and a MC code's validation against the literature and experimental measurements is provided.

1 GEANT4 - GEometry ANd Tracking

GEANT4 (Agostinelli and et al., 2003) is a general purpose toolkit for MC simulation firstly developed at CERN (Conseil Européen pour la Recherche Nucléaire) by an international collaboration of scientists from all over the world. The word GEANT is an acronym standing for *GEometry ANd Tracking* due to its skills to describe geometrical structures and to simulate the particles' interaction with matter.
The very first version of GEANT dates back to 1974 and it was written in FORTRAN while the current version exploits the Object Oriented Programming (OOP) in C++. The OOP gives to the toolkit three main advantages: *Extesibility* (i.e. the possibility to add, remove or modify parts of the code), *Flexibility* (i.e. users can provide several choices to solve problems) and *Openness* (i.e. each part of the code is directly controlled by users). These characteristics yield to GEANT4 the capabilities to be used for different applications such as high energy physics, nuclear physics, astrophysics, medical physics and recently biophysics (with the Geant4-DNA project Incerti and et al. (2010)).
The main concepts of OOP are classes and inheritance: a class represents a common set of attributes and functionalities while inheritance means that every object can derive methods and attributes from other objects (as in a hierarchic structure).

1.1 Architecture and Design

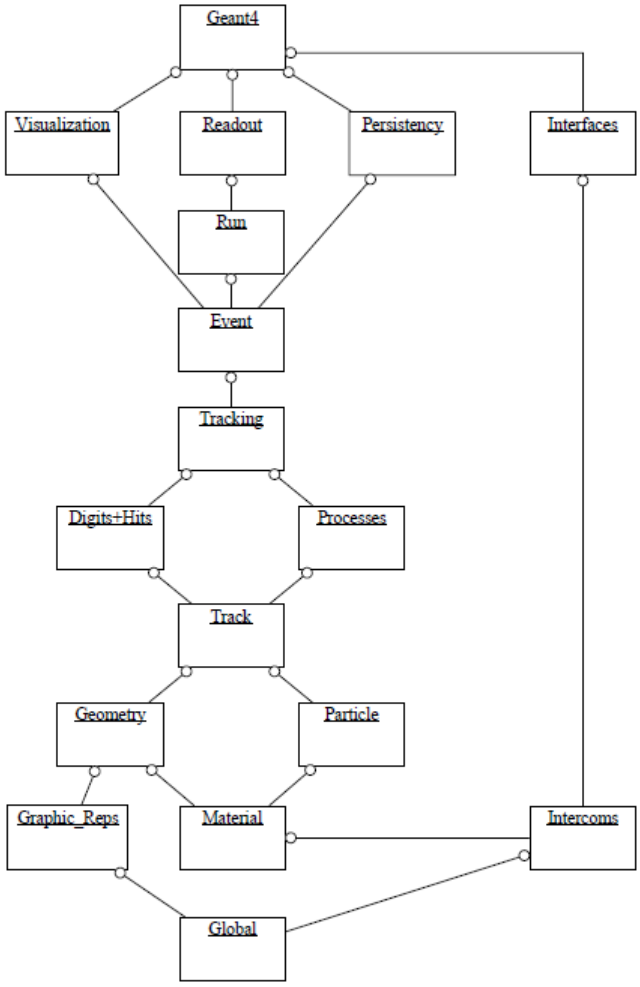

Figure 6.1: The diagram shows all GEANT4 categories (Agostinelli and et al., 2003).

The diagram of all categories in which GEANT4 is divided is shown in Fig.(6.1): the lower part represents the basis of the toolkit and the upper part comes from it.
The features of the main categories can be summarized as follows:

- *Run* and *Event* − this part controls the creation of the primary event and of all the secondary particles that can be produced.
  The classes that compose the *Run* and *Event* part are *G4Run* and *G4Event*.
  The management of single events is controlled by a *stack*, containing the particles that have still to be processed. When the stack is empty the event is finished.

- *Tracking*, *Track* and *Step* − are connected to the propagation of the particles and can control the length of a *step*, which describes the gap between two points and is represented by the class *G4Step*.

- *Hit* and *Digitization* − control the real sensitive part of the simulation and create the track of a particle that passes through a volume generating a logic signal.
  A *hit*, described by the class *G4hit*, is a sort of picture of the particles interaction with the detector. At the end of each event every hits can be collected in *G4Event*.

- *Particle* − this category controls the particles physical properties. The class *G4Particle Definition* allows to implement the particles properties (such as electric charge, mass, etc.).

- *Material* − Material refers strictly to real world: only molecules, isotopes or materials already contained in the libraries of the National Institute of Standard Tecnology (NIST) can be used in the *G4NistManager* class.

- *Geometry* − this part controls the different geometrical structures that can be created, such as cylinders (*G4Tubs*), spheres (*G4Sphere*), cubes (*G4Box*), etc.
  In GEANT4 the *Solid Volume*, which is the real dimension of the structure, the *Logic Volume*, such as materials and other properties, and the *Physics Volume*, which is the positioning of the structure in space, have to be specified.

- *Physics* − this part rules all physical processes that can occur to a particle from its decay to its electromagnetic or adronic interaction.

Three mandatory classes have to be implemented in a GEANT4 application:

- *G4UserDetectorConstruction* − which gives a definition of the simulation environment, including the description of all geometrical structures, materials and sensitive parts.

- *G4UserPhysicsList* − where the user is asked to specify which kind of physical interaction has to be used.

- *G4UserPrimaryGenerationAction* − in which the user has to indicate how the particles have to be generated.

The existence of these three classes is ensured at the beginning of the simulation by *G4RunManager*, which involves *initialize* and *beamOn*.
These following classes can be implemented to personalize the output:

- *G4UserRunAction* − to control actions that have to be done at the beginning and at the end of every simulation run.

- *G4UserEventAction* − to control actions that have to be done at the beginning and at the end of every simulation event.

- *G4UserSteppingAction* − to control actions that have to be done at every simulation step.

2 Monte Carlo Computational Choices

Every MC programs developed using GEANT4 can be highly customized according to the specific users' requirements.
While the *G4UserDetectorConstruction* and *G4UserPrimaryGenerationAction* classes are not

usually "fixed" for each simulations (i.e. the users can change the geometry, the material composition or the particles generation between one simulation and the further) the *G4UserPhysicsList* is the same for each simulations.
The same condition happens for the simulation output: the output can be highly personalized by users but the method implemented for calculating the Mean Glandular Dose (MGD) is the same for all simulations.
The choices made about those two aspects are now discussed.

2.1 PhysicsList

As a toolkit, GEANT4 offers to the users several choices physical processes models: users can specify the physical interactions that have to be simulated by implementing the class *G4UserPhysicsList*. Several reference PhysicsLists are routinely validated (Katsuya and et al., 2005) and updated by the GEANT4 collaboration. It is mandatory, for medical applications, to have a very good description of electromagnetic interactions of photons, electrons, hadrons and ions with matter in the energy range of interest. The electromagnetic interactions of photons are crucial for mammographic applications and the choice of the PhysicsList has to be carefully operated.
The choices the researchers make regarding the PhysicsLists are not usually stated in the literature: scientific papers do not often specify this information (Thacker and Glick. (2004), Sechopoulos *et al.* (2006), Myronakis *et al.* (2013) or Mahdavi *et al.* (2015)) nor authors make same choices (Lanconelli *et al.* (2013), Mittone *et al.* (2014) or White *et al.* (2014)).
A work conduct within the SYRMA-CT project (Fedon *et al.*, 2015) discuss which can be the optimal choice.
Starting from the suggestions made by the Geant4 Low Energy Electromagnetic Physics Working Group, several PhysicsLists (Incerti and et al., 2014) were tested: Tab. (6.1) presents the PhysicsLists implemented in this analysis.

Name	Content
G4EmStandardPhysics	Standard EM physics
G4EmLivermorePhysics	Low-energy EM physics using Livermore data
$G4EmStandardPhysics-option4$	Most accurate physics models from standard and low energy
G4EmPenelopePhysics	Low-energy EM physics implementing Penelope models

Table 6.1: PhysicsLists suitable for medical applications (Incerti and et al., 2014).

In order to select which of these PhysicsLists show the best performance for a breast dosimetry simulation, the data provide by Hammerstein Hammerstein *et al.* (1979) for different glandular fractions were used as a benchmark. Then experimental results of (Johns and Yaffe, 1987) and (Chen and et al., 2010) were also used for testing the MC values.
The linear attenuation coefficient (μ) was obtained using the following formula:

$$\frac{\mu}{\rho} = \frac{-ln\left(\frac{I_{out}}{I_0}\right)}{x \cdot \rho} \tag{6.1}$$

where I_{out} is the number of photons that exit from the sample, I_0 is the number of photons entering in the sample, x is the thickness and ρ the density reffering to the property tissue.

Several runs of a point monochromatic photons source within the energy range of 8-50 keV were simulated (with a 1 keV step). The number of primary photons generated was 10^6 and in order to achieve a good statistical uncertainty on the estimated quantities (i.e. a Coefficient Of Variation (COV) less than 0.5%) simulations were repeated using different seeds for each simulation. The monochromatic photon beam impinged on a slab of one of the selected materials. The chemical composition of the materials used are obtained by the data of (Hammerstein *et al.*, 1979) and briefly summarized in Tab. 6.2

Glandularity Fraction (%)	Density (g cm^{-3})	H(%)	C(%)	N(%)	O(%)	P(%)
0%	0.9301	11.2	61.9	1.7	25.1	0.1
50%	0.9819	10.7	40.1	2.5	46.4	0.3
100%	1.04	10.2	18.4	3.2	67.7	0.5
Skin	1.09	9.8	17.8	5	66.7	0.7

Table 6.2: Breast tissues composition from (Hammerstein *et al.*, 1979).

The slab thickness was set to 2 cm in order to avoid that all photons were absorbed or traverse the slab without interacting. When a photon has an interaction, the simulation event is aborted. Data were stored in appropriate variables that allowed us to calculate the coefficients. Fig. (6.2) shows the simulated geometry.

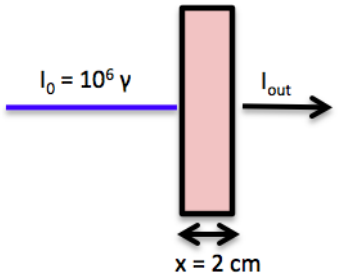

Figure 6.2: A sketch of the simulated geometry: 10^6 monochromatic photons impinged on a slab (2 cm thickness) of a specific glandular material. The number of photons which exit from the slab is used for estimating the linear attenuation coefficient.

The relative difference $R\%$ is used for compared the results:

$$R\% = \frac{\mu - \mu^*}{\mu^*} \cdot 100 \tag{6.2}$$

where μ is the linear attenuation coefficient calculated in the present work and μ^* is the linear attenuation coefficient presented in (Hammerstein *et al.*, 1979) or the experimental one. The results are shown on Fig. (6.3).

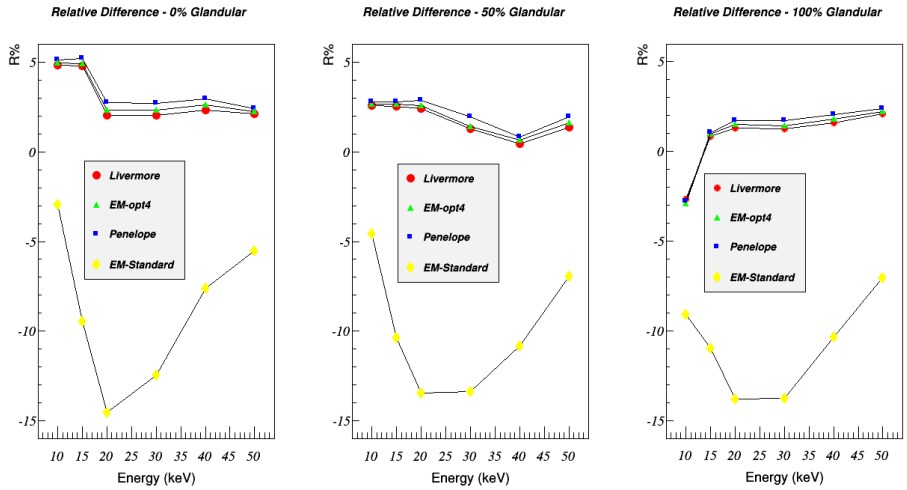

Figure 6.3: R% values for 0% (left side), 50% (centre) and 100% (right side) glandular fraction. All graphs show the comparison between G4EmLivermorePhysics (red dots), G4EmStandardPhysics-Option4 (green triangles), G4EmPenelopePhysics (blue squares) and G4EmStandardPhysics (yellow diamonds) as a function of energy.

The relative difference R% (Eq. 6.2) for the G4EmStandardPhysics is in the range of 3-14.5% while for the three low energy PhysicsLists is within range of 0.5-5.2% (Fig. 6.3): among them the best results are always obtained by G4EmLivermorePhysics. G4EmStandardPhysics can be considered as a starting point of every GEANT4 simulation: the Rayleigh effect is not available in the G4EmStandardPhysics and the set of models for the particles interactions are different from three low energy PhysicsLists (Katsuya and et al., 2005).
Fig. (6.4) focuses the attention on G4EmLivermorePhysics (i.e. the PhysicsList that obtained the best results, Fig. 6.3) and reports the comparison with Hammerstein (Hammerstein *et al.*, 1979) and experimental values obtained by Johns and Yaffe (1987) and Chen and et al. (2010).

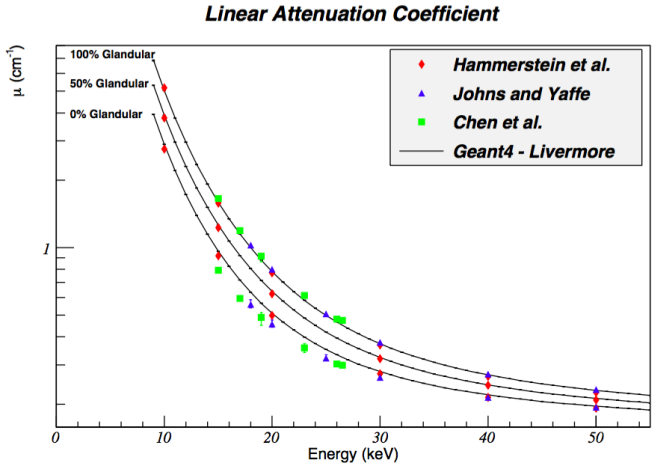

Figure 6.4: Linear attenuation coefficient obtained using G4EmLivermorePhysics for 0%,Äì50%,Äì100% glandular fraction (solid lines). Data obtained by Hammerstein et al. (Hammerstein *et al.*, 1979) are reported in red diamonds, experimental results of Johns and Jaffe (Johns and Yaffe, 1987) in blue triangle while Chen et al. (Chen and et al., 2010) in green square. The bars on experimental data are referring to the values range.

A good agreement is found for the 100% glandular tissue: maximum difference of 2.7% with data of Hammerstein *et al.* (1979) and maximum difference of 2.6% with experimental data (Johns and Yaffe, 1987). Larger differences are observed for the 0% glandular at the low energies: maximum difference of 4.8% with data of Hammerstein *et al.* (1979) and maximum overestimation of 10% with experimental data (Johns and Yaffe, 1987).
The agreement between simulated data and Hammerstein *et al.* (1979) was expected as both glandular and adipose tissues composition is the same (see also Fig. 6.5 which shows an excellent agreement, $r^2 = 1$).

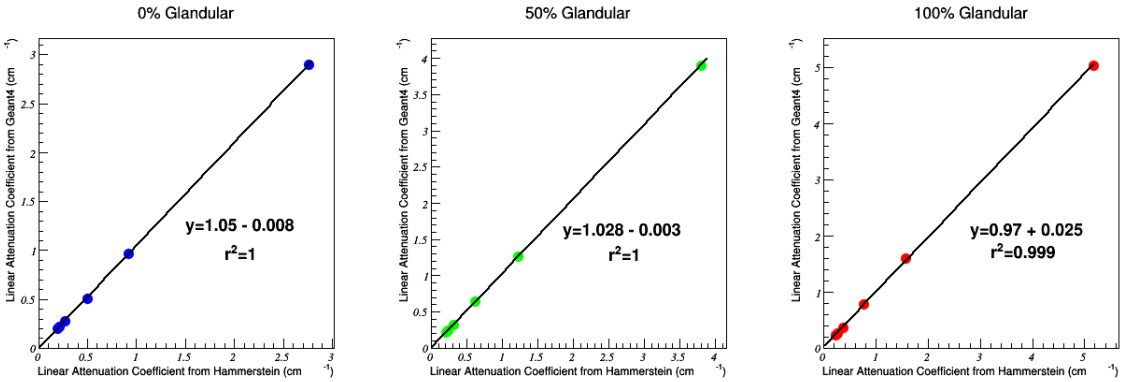

Figure 6.5: Regression line fit equation for 0% - 50% - 100% glandular fraction. An excellent agrement is found between simulated data using G4EmLivermorePhysics (y-axes) and (Hammerstein *et al.*, 1979)(x-axes).

The experimental linear attenuation coefficients of the adipose tissues are lower that the MC data; however, the fat values of the two experimental data set (Johns and Yaffe (1987) and Chen and et al. (2010)) are comparable within the experimental uncertainties. The differences with MC data decrease at the high energies, up to be negligible at 50 keV. Such a systematic overestimation of the adipose linear attenuation coefficients based on Hammerstein data can be related to experimental uncertainties of the fat composition or density and to the inter-individual variability (Pani and et al., 2004).
The performances of G4EmLivermorePhysics were deepen verified activating or deactivating the physical interactions (e.g. photoelectric effect, Compton and Rayleigh scattering) for obtaining the mass attenuation coefficients for each processes. The results are shown in Fig. (6.6) with the comparison with the NIST data (Hubbell and Seltzer, 1993) and (Hammerstein *et al.*, 1979).
G4EmLivermorePhysics was decided to be used in all the MC simulations.

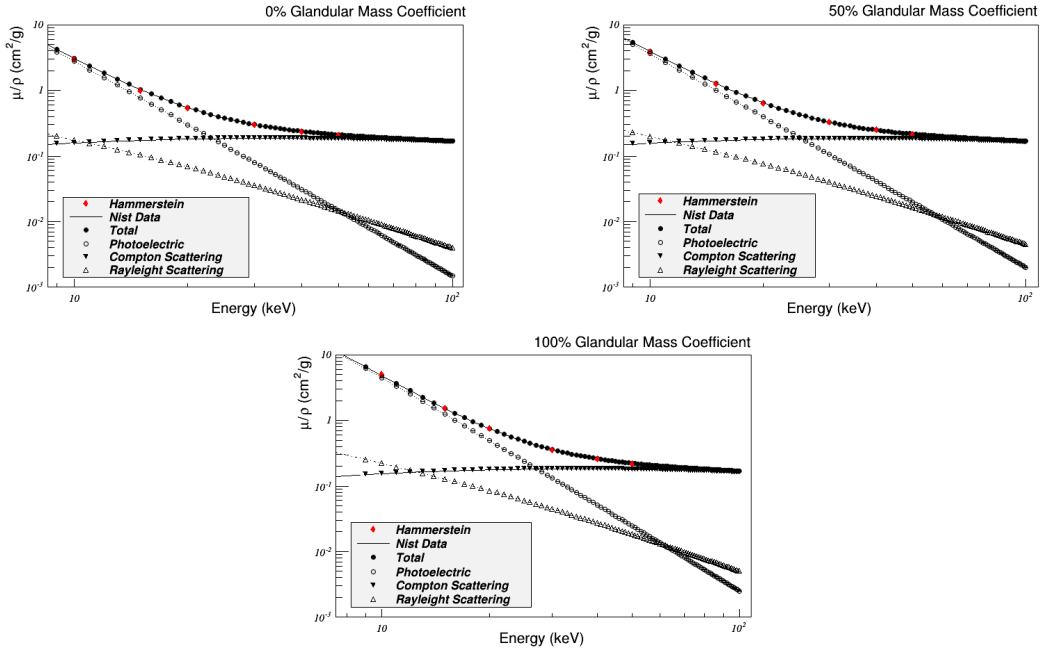

Figure 6.6: Mass attenuation coefficients obtained using G4EmLivermorePhysics for different physical interactions (points), Hammerstein et al. data (Hammerstein *et al.*, 1979) (red rhombi) and NIST data (continue and dashed lines) for three different glandular fraction.

2.2 Dose Evaluation Procedure

The parameter that quantifies the radiation dose delivered to the glandular component of the breast tissue is the Mean Glandular Dose (MGD, as explained in chapter 4). In this work the MGD obtained by MC code is calculated as follows:

$$MGD = \frac{E_{dep} \cdot G}{mass_g \cdot f_g} \tag{6.3}$$

where E_{dep} is the energy delivered to the breast tissue (without skin), $mass_g$ is the mass of the breast (without skin), f_g is the glandular fraction and G is the G-factor introduced by Boone (Boone, 1999) as

$$G = \frac{f_g \left(\frac{\mu_{en}}{\rho}\right)_g}{\left[f_g \left(\frac{\mu_{en}}{\rho}\right)_g + (1 - f_g)\left(\frac{\mu_{en}}{\rho}\right)_a\right]} \tag{6.4}$$

where the mass energy absorption coefficients (μ_{en}/ρ) are referred with an a subscript for adipose tissue and with a g subscript for glandular tissue, while f_g is the glandular fraction, by weight, of the breast tissue (f_g = 1 for glandular, f_g = 0.5 for 50% glandular etc.). The G-factor coefficient was introduced for taking into account the glandularity and should be applied interaction-by-interaction (as described by (Wilkinson and Heggie, 2001).

Even if the use of G-factor coefficient is well documented in the literature nevertheless some authors use it interaction-by-interaction (Boone (2002), Thacker and Glick. (2004), Sechopoulos *et al.* (2006), Myronakis *et al.* (2013)) while others consider the G-factor as an additional coefficient, which has to be added retrospectively for MGD evaluation (Boone (1999), Mittone *et al.* (2014)). Thus, different results can be achieved: the results of the two approaches (interaction-by-interaction and retrospectively) are compared and discussed (Fedon *et al.*, 2015). Two scenarios are taking into account: (i) the G-factor is added retrospectively, when μ_{en}/ρ are related to the beam primary energy, (ii) the G-factor is estimated interaction-by-interaction.
The method proposed by Okunade (Okunade, 2007) was used for calculating the mass energy absorption coefficient for all the compounds elements; according to that method values of $(\mu_{en}/\rho)_a$ or $(\mu_{en}/\rho)_g$ were obtained as follows:

$$\frac{\mu_{en}}{\rho}(x) = \Sigma_i W_i \left[\frac{\mu_{en}}{\rho}(x)\right]_i \tag{6.5}$$

where $[(\mu_{en}/\rho)(x)]_i$ are the mass energy absorption coefficients for the ith element and W_i is the fraction by weight for the ith element in the compound. Values of $(\mu_{en}/\rho)_a$ and $(\mu_{en}/\rho)_g$ obtained by Eq.(6.5) were fitted in the interval energy 8 - 50 keV using the ROOT data Analysis Framework and the results are presented in Fig. (6.7). The fit functions are composed by several parts, which best-fitted specific energy interval. All fit functions show an excellent correlation ($r^2 > 0.999$) with the NIST data (a difference below 0.1% was achieved). Wilcoxon Signed Rank test was used between NIST data and fit data: fit data were not significantly different from the NIST data (p-value for adipose 0.98; p-value for glandular 0.99).

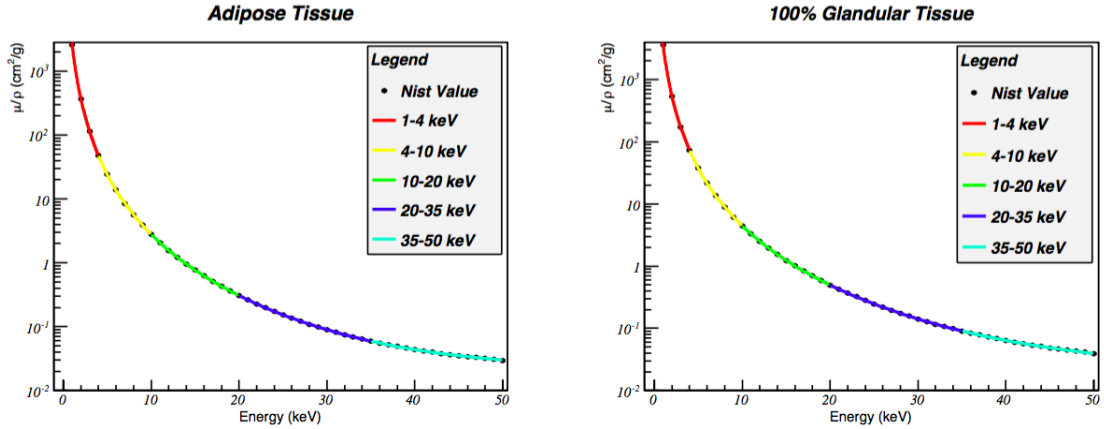

Figure 6.7: NIST values of mass energy absorption coefficient (black dots) and fit functions (with different colours).

The mathematical equations and the related parameters of the several fit functions are presented in Tabs. (6.3 and 6.4).

The proposed fit equations were implemented in the MC program and the G-factor analysis was carried on according to Eq. (6.3) and Eq. (6.4).
Fig. (6.8) shows the results of applying the G-factor interaction-by-interaction (solid line) or retrospectively (dotted line) for a 50% glandular breast using G4EmLivermorePhysics (similar behavior is found for all other glandular fractions).

Energy range (keV)	Fit equation	Parameters value
1-4	$(a/(x^b+c))+d$	a= 2768.13 b= 2.88037 c= 0.07367 d= -3.23978
4-10	$(a/(b+c\cdot x^d))+e$	a= 50707.5 b= 13.9004 c= 14.5793 d= 3.08251 e= -0.089153
10-20	$(a/(b+c\cdot x^3))+d+e\cdot x$	a= 55966.6 b= -580.838 c= 20.0272 d= -0.145142 e= 0.00507372
20-35	$(a/(b+c\cdot x^3))+d+e\cdot x$	$a=$ 43.9956 $b=$ -11.1528 $c=$ 0.0192767 d= -0.00892 e= 0.0004033
35-50	$(a/(b+c\cdot x^3))+d$	$a=$ $2.6947\cdot 10^6$ $b=$ $-1.4991\cdot 10^7$ $c=$ 1847.76 d= 0.0175524

Table 6.3: Fit functions and parameters values for $(\mu_{en}/\rho)_a$.

Energy range (keV)	Fit equation	Parameters value
1-4	$(a/(x^b+c))+d$	a= 3664.9 b= 2.7337 c= 0.009753 d= -9.01574
4-10	$(a/(b+c\cdot x^d))+e$	a= 73226.7 b= 17.6474 c= 14.2058 d= 3.0487 e= -0.140218
10-20	$(a/(b+c\cdot x^3))+d+e\cdot x$	a= 892136 b= -4276.73 c= 198.54 d= -0.20005 e= 0.0067657
20-35	$(a/(b+c\cdot x^3))+d+e\cdot x$	$a=$ 73.0777 $b=$ -5.98609 $c=$ 0.01857 d= -0.03248 e= 0.0008786
35-50	$(a/(b+c\cdot x^3))+d$	a= 5.0999 b= -10.7473 c= 0.01841 d= 0.01617

Table 6.4: Fit functions and parameters values for $(\mu_{en}/\rho)_g$.

The retrospectively G-factor application leads to an overestimation of MGD of 7% (at 10 keV) that decreases with the energy increase: at 10 keV the linear attenuation coefficient of several tissues is higher than a high energy. The low energy photons (10 keV) were mainly attenuated by the skin layer Boone (1999) causing an energy reduction of the incoming photon. Thus higher values for $(\mu_{en}/\rho)_a$ and $(\mu_{en}/\rho)_g$ are applied for the G-factor glandular calculation.
The effect of skin attenuation decreased while increasing the energy (20 keV) but photons were also attenuated by breast material. In fact, at this energy, the photoelectric effect is predominant and the energy delivered to the tissue is the highest possible. At 50 keV the tissue attenuation is lower, so the G-factor applied interaction-by-interaction is almost equal to the one applied retrospectively (due also to the smoother trend of energy absorption coefficients).
The retrospective application of G-factor leads to the scenario in which an incorrect glandular weighting factor is applied to the total energy deposited: the energy reduction, due to the skin layer and glandular material, is not further taken into account thus, the values for $(\mu_{en}/\rho)_a$ and $(\mu_{en}/\rho)_g$ are always lower, leading to a higher G-factor.

The application of G-factor interaction-by-interaction was used in all the MC simulations.

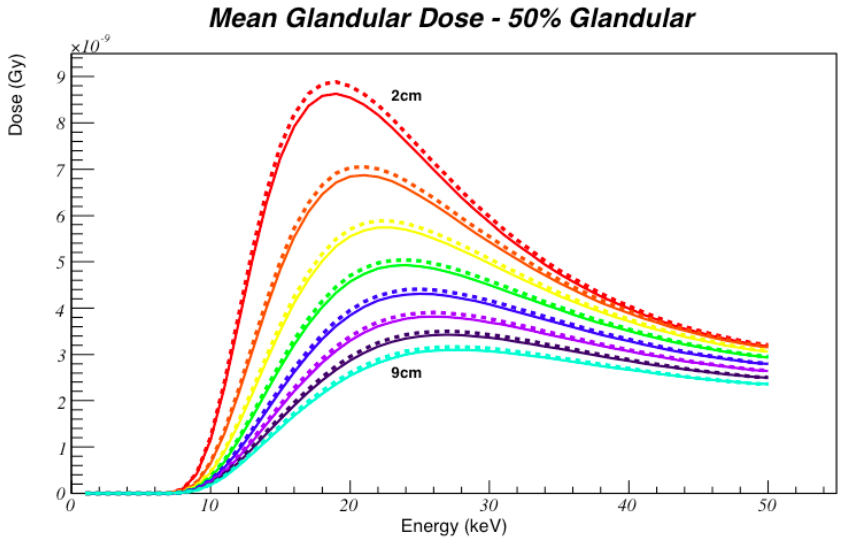

Figure 6.8: G-factor applied interaction by interaction (solid line) and retrospectively (dotted line) as a function of monochromatic energy. The data are shown for breast thickness ranging from 2 up to 9 cm.

3 Monte Carlo Validation

The Monte Carlo code was validated comparing the results with the literature and with experimental measurements.
The validation against the literature was carried on comparing the MC data with the mammography set up proposed by (Boone, 2002) (which is considered the starting point for every breast dosimetry MC code) and with the data obtained by (Boone *et al.*, 2004) and (Mittone *et al.*, 2014) in a breast-CT set up.
The experimental validation was performed at the SYRMEP beam line of Elettra synchrotron implementing the experimental set up within the MC code.

3.1 Literature Validation

Mammography

In order to validate the code with the literature, the data produced by (Boone, 2002) with the (Wilkinson and Heggie, 2001) suggestion is used as a benchmark.
The code was modified in order to match as closed as possible the set up described in (Boone, 2002). The geometry is comprehensively described in the work of Boone (2002), whilst here only an outline is given.
A semi-cylindrical breast shape was simulated (with a thickness ranging from 2 to 9 cm with a 1 cm step) with a radius of 8.5 cm and a skin layer of 0.4 cm (Fig. 6.9). A semi-cone shaped radiation field irradiated the breast (with energy from 8 up to 50 keV with a 1 keV step) from a fixed distant of 65 cm.

The breast homogeneous tissue composition is shown in Tab. (6.2). For each breast thickness and breast composition, the number of monochromatic primary photons generated was 10^6 and simulations were repeated nine times (per each case), using different seeds, for achiev-

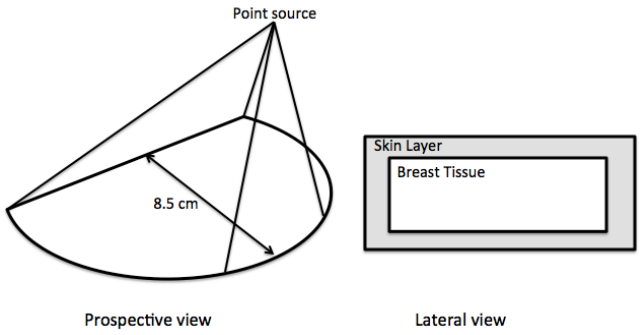

Figure 6.9: Schematic representation of the simulated geometry: the prospective view (on the left side) shows the semi-cylindrical breast shape and the x-ray point source; the lateral view (on the right side) shows the skin layer and the inner homogeneous breast tissue.

ing a coefficient of variation (COV defined as the ratio of the standard deviation to the mean value) less than 0.5%. Figs. (6.10) and Figs. (6.11) shown the result for the quantity called f(E), which is defined in Boone (1999):

$$f(E) = \frac{energy\ absorbed\ per\ incident\ photon}{photon\ energy} \tag{6.6}$$

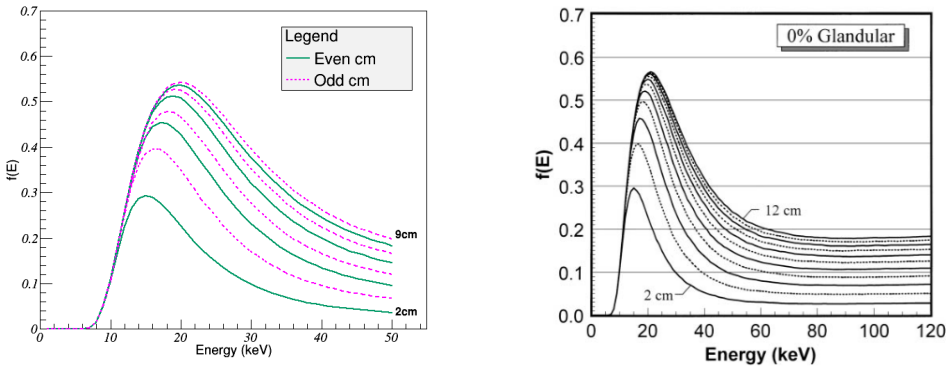

Figure 6.10: Comparison between f(E) quantity obtained by MC (left side) and by Boone(Boone, 1999) (right side). The glandularity taken into account is 0%.

The comparison assures that the energy deposited on the inner-breast part is the same.

The formula used for estimating the normalized glandular dose coefficient (DgN) is based on previous Eq. (6.3) divided by the exposure (χ) measured at the breast surface as shown in the following equation:

$$DgN(E) = \frac{MGD}{\chi} \tag{6.7}$$

Fig. (6.12) shows the linear correlation between DgN obtained by Boone (2002) (on abscissa) and by the MC code (on ordinate) for a standard breast (as defined in Commission

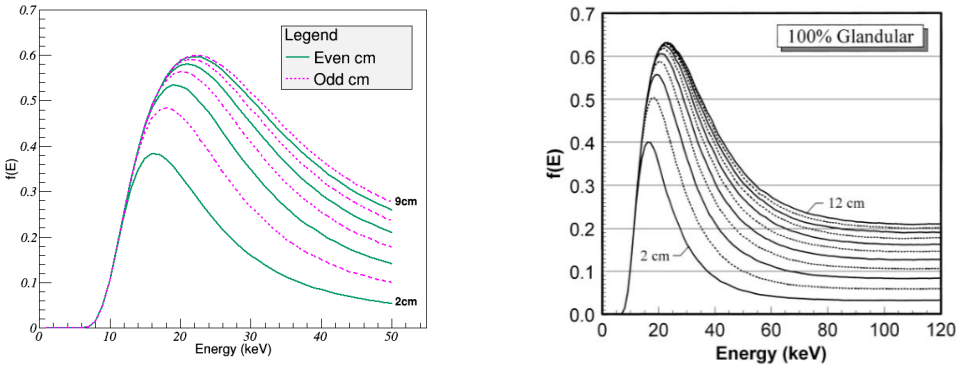

Figure 6.11: Comparison between f(E) quantity obtained by MC (left side) and by Boone (1999) (right side). The glandularity taken into account is 100%.

(2006)): an excellent agreement is found.
In appendix A are presented the comparison results for all the thicknesses and glandular fraction.

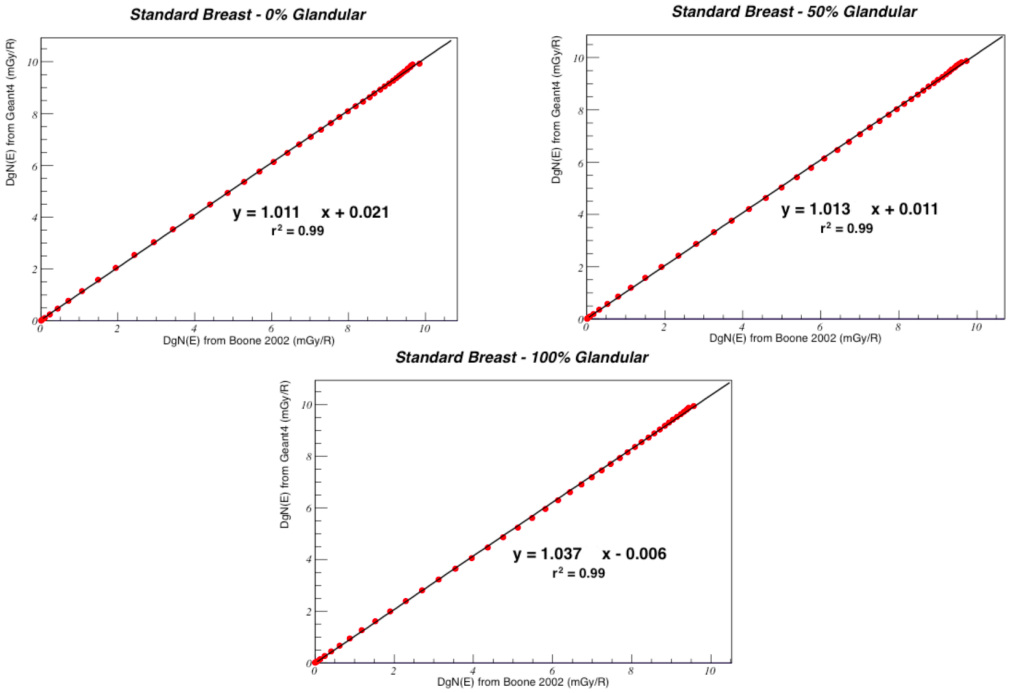

Figure 6.12: Linear correlation between Boone data (Boone, 2002) (on abscissa) and MC data obtained by GEANT4 (on ordinate): excellent linear correlation is observed.

Computed Tomography

The MC code was modified in order to match as closed as possible the geometry described by Boone *et al.* (2004) and Mittone *et al.* (2014).
In Boone *et al.* (2004) the geometry consists in a cylindrical breast sample with a diameter ranging from 8 to 20 cm. The monoenergetic photons were emitted from a x-ray cone source toward the breast sample. The histogram of the number of photon interactions as a function of x-ray energy for an input x-ray beam consisting of monoenergetic 60 keV photons was produced and compared with the one shows in Fig. (5) of Boone *et al.* (2004). Result are portrayed in Fig. (6.13).

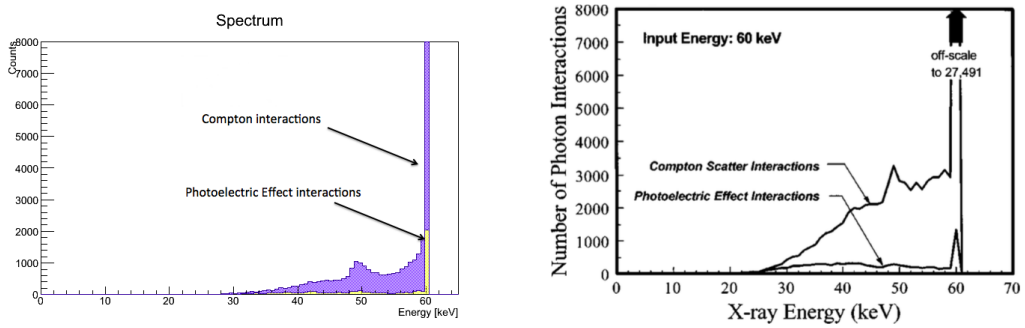

Figure 6.13: Pulse height spectrum obtained by MC code (left side) and by Boone *et al.* (2004) (right side).

In Mittone *et al.* (2014) the breast was modeled as a homogeneous cylindrical volume and the photons were emitted from a monochromatic parallel beam toward the breast sample. Fig. (6.15) shows the comparison between MC data and the data obtained by Boone *et al.* (2004) and Mittone *et al.* (2014) in term of Mean Glandular Dose for a 12 cm diameter breast with a glandular composition of 50%.

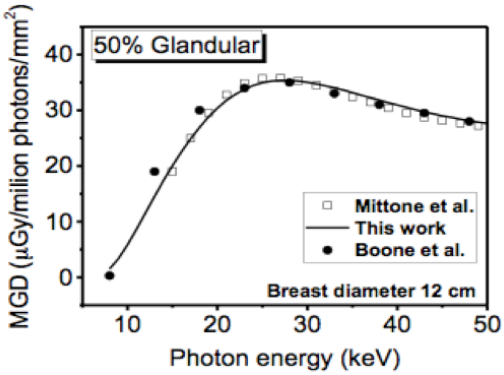

Figure 6.14: Comparison among the data calculated with the present code (black line) and the data reported in the literature (Boone *et al.*, 2004) (close circle) and (Mittone *et al.*, 2014) (open square).

The maximum deviation between the data in this work and that of Boone *et al.* (2004) is 3% over 18 keV, and that between this work and the MC data of Mittone *et al.* (2014) is 3% in all energy range.

3.2 Experimental Validation

CTDI Measurements

Computed Tomography Dose Index (CTDI) is the current standard for CT examination, and provides information on the radiation dose to the scan volume. As explain in chapter 4, this index takes into account the scatter dose, which makes radiation dose from a multiple acquisition greater than that of a single slice.
The measurement of CTDI follows a precise protocol (AAPM, 2010) which implies the use of a polymethylmethacrylate cylinder of 15 cm length and diameter of 16 cm (head phantom) and 32 cm (body phantom), Fig. (6.15).

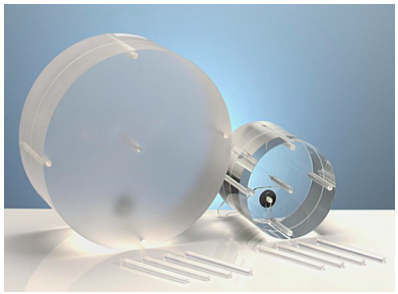

Figure 6.15: Phantoms used for measuring the Computed Tomography Dose Index (CTDI): body phantom (on left side) and head phantom (on right side).

The CTDI measurements were performed with a Radcal pencil chamber (mod. 10X6-3CT) connected to the dosimeter Accu-Pro (Radcal). The ionization chamber provides the exposure time and the air-kerma value corrected with the temperature, pressure and calibration factor. The active volume is 3 cm^3 (100 mm length and base area of 0.3 cm^2).
The phantoms used in this measurements were custom-made in order to better approximate the breast condition: the height was the same as prescribe in the AAPM protocol but the diameter was 8, 10, 12 and 14 cm.
During the measurements the phantom rotates by 360 degree with a speed of 3 deg/s in an exposure time of 60 s. Fig. (6.16) shows the experimental set up.

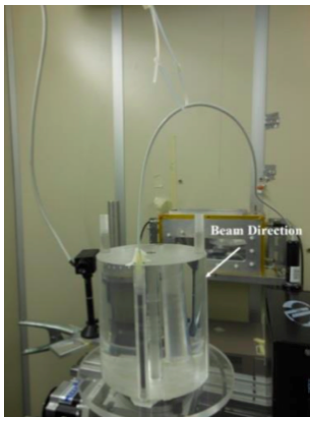

Figure 6.16: Computed Tomography Dose Index (CTDI) experimental set up: the synchrotron radiation beam comes from the right part and impinges on the PMMA phatom in which the RADCAL chamber was insert.

The measurements were carried out at 18, 20, 24, 28, 32, 35, 38 and 40 keV.
The described set up was simulated with the code developed in this work.
The RADCAL was modeled based on the data given by the manufacturer: an inner cylinder volume of $3cm^3$ was implemented surrounded by cylindrical layers of different materials (0.5 mm graphite, 0.5 mm air and 0.5 mm graphite). The energy deposit by any interaction that took place inside the inner part of the ionization chamber was recorded and used to calculated the CTDI.
For each projections up to 5 million photons were generated from a monochromatic parallel beam source. The simulations were repeated 25 times using different seeds for each simulations for achieving a COV value less than 1%.
Fig. (6.17) shows the simulated phantom (left side) and the simulated RADCAL chamber (right side).

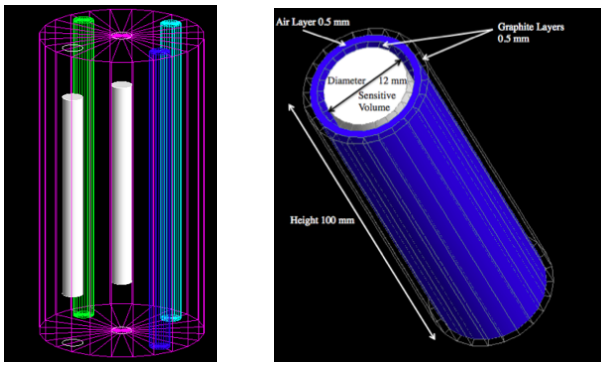

Figure 6.17: Left figure shows the simulated phantom: the dose was recorded within the white cylinder according to the AAPM protocol (on the center or on the peripheral). The right figure shows the simulated RADCAL chamber: the dose was reordered only within the white sensitive volume.

The comparison between the simulated (open black circle) and measured (closed symbol) ratio of CTDI values in the center of the phantom and in air are shown in Fig. (6.18). The experimental bar error is 5%. The agreement is within the bar error of the experimental data for the majority of the measurements. Some measurements (as 38, 40 keV) show a discrepancy between simulated and experimental data due to a very low flux at those high energy.

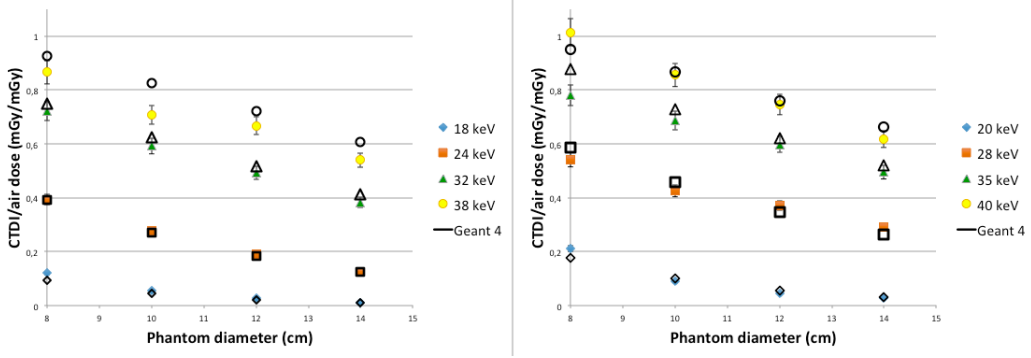

Figure 6.18: Comparison between simulated data (open black circle) and measured (closed symbol). The graphs shows the ratio of the CTDI values to the air dose (vertical axes) as a function of phantom diameter (horizontal axes) for several energy taken into account.

TLD Measurements

Thermoluminescence dosimetry is one of the main dosimetric techniques used for estimating the absorbed dose in medical applications.
There are different types of TLDs chips can (see Chapter 5) according to the application and the material whom they are made. TLDs type GR-200A are the dosimeters used for these measurements: they are made of LiF:Mg,Cu,P (according to Tab. 6.5), and have a cylindrical shape with a radius of 2.25 mm and a height of 0.8 mm. They are produced by Solid Dosimetric Detector Method Laboratory in Beijing, China. GR-200A can be considered equivalent to the type TLD-100H, which are produced in USA by Thermo Scientific.

LiF	Mg	Cu	P
99.5 %	0.2 %	0.004 %	0.296 %

Table 6.5: Chemical composition of Tld GR-200A.

The dose measured by the i-TLD chip (D_i) is evaluated using the formula:

$$D_i = R_i \cdot K_i \cdot E_i \tag{6.8}$$

where R_i is the TLDreader output (nC), K_i (mGy/nc) is the individual calibration factor and E_i is an adimensional factor which takes into account the tld energy response (obtained by Fig. 6.19). The combined percentage uncertainty (u_i) is:

$$u_i(\%) = \sqrt{u_R^2 + u_K^2} \tag{6.9}$$

where u_R^2 is the reader uncertainty (5% given by the manufacturer), u_K^2 is the calibration factor uncertainty (in the range 1-5 %).
The overall combined uncertainty is between 5%-7%.

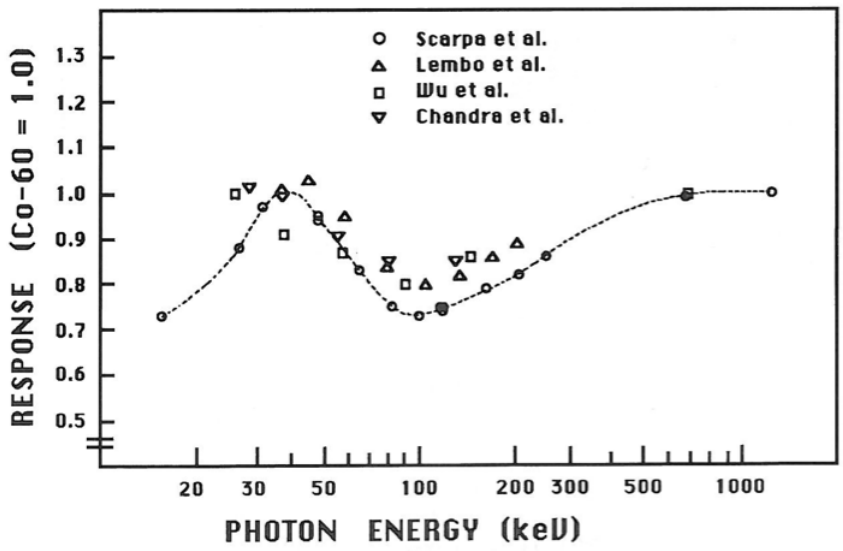

Figure 6.19: Tld GR-200A energy response normalized to ^{60}Co (Martella).

The TLD chips were inserted into a cubic Plexiglas phantom (90 mm x 90 mm) composed of 6 slices of 10 mm thickness (three chips can be placed at the same time on each slice). The phantom design allowed no one of the TLDs in a slice to obscure the chips on the next slice and therefore an hexagon inside a dodecagon tld displacement could be obtained (see Fig. 6.20).

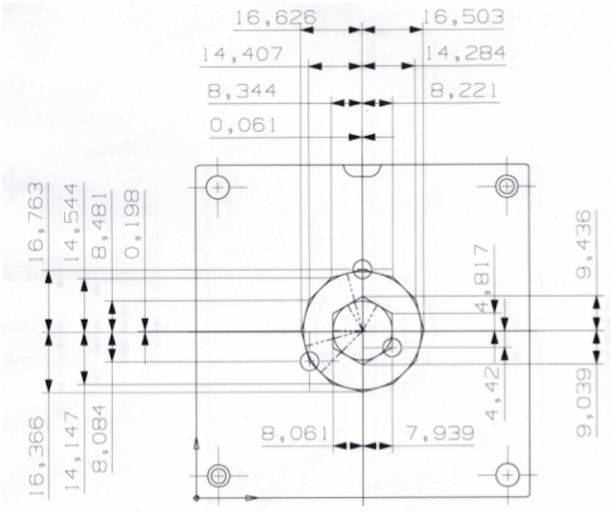

Figure 6.20: Phantom project for the TLDs measurments. All numbers are in mm.

The phantom was then exposed for 15 hours to a radioactive source of ^{60}Co (activity of 49.53 MBq) placed at 1 m from the object in the calibration bunker of the Elettra Synchrotron, as shown in Fig. (6.21). A plexiglass slab of 5 mm thickness was placed in front of the object for build-up purposes.

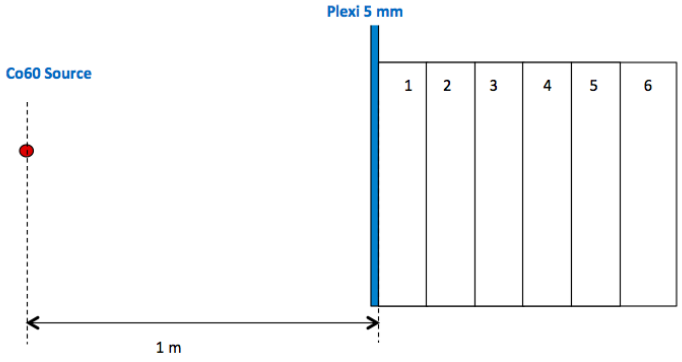

Figure 6.21: Irraditiation setup inside the calibration bunker of Elettra: the ^{60}Co source was placed 1 m far from the phantom and an additional plexiglass slab of 5 mm thickness was added for build-up purposes.

The same experimental setup was then implemented into the GEANT4 MC code and into another MC code developed by the radiation protection staff of Elettra using FLUKA (Ferrari *et al.* (2005) and Battistoni *et al.* (2007)). Fig. 6.22 shows the implemented setup in GEANT4: each TLD position was numbered in order to have positions 1-2-3 on the first slab, position 4-5-6 on the second slab, etc.

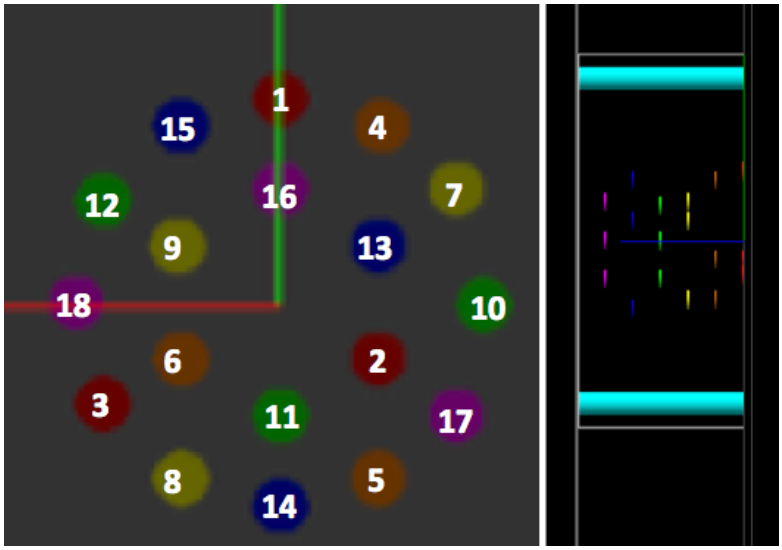

Figure 6.22: Phantom simulated in GEANT4: frontal view (left side) and lateral view (right side). The two cyan cylinders on the right side are filled of air.

Up to 500 billion ^{60}Co decays were simulated in GEANT4 in order to achieve a COV value lower than 0.1 %, while in FLUKA 27 billion decays were simulated (with a COV value of 3%). The difference in the primary particle generation is due to the different computer facilities: GEANT4 MC code was run on the INFN farm in Trieste (mainly devoted to research aims), whilst FLUKA MC code was run on the Elettra facility, which gives to the users a limited time for running MC simulations. However, as the aim of these measurements is not to compare the performance of the two MC software, the higher FLUKA statistic uncertainty is not an issue, in that it can be decreased increasing the simulation time.
The experimental dose obtained using Eq. (6.8) is related to the water-dose (as the calibration coefficient is given for evaluating the dose in water), so the ratio of the mass-energy-absorption coefficient between the TLD LiF material and water needs to be added. Thus, the formula becomes:

$$D_i^{Total} = D_i \cdot \frac{(\mu/\rho)_{en}^{LiF}}{(\mu/\rho)_{en}^{Water}} \tag{6.10}$$

where D_i is equal to Eq. (6.8) and $(\mu/\rho)_{en}^{LiF}/(\mu/\rho)_{en}^{Water}$ is evaluated at 1253 keV (mean energy of the two gamma emitted ^{60}Co). E_i factor (in Eq. 6.8) is equal to 1 as the measurement is performed using the ^{60}Co reference source. The value of $(\mu/\rho)_{en}^{LiF}$ and $(\mu/\rho)_{en}^{Water}$ was calculated using the software XMuDat (Nowotny, 1998).
The MC results were multiplied by a scale factor that accords the experimental and the simulated ^{60}Co activity.
Results are shown in Fig. (6.23): all MC and experimental measurements are compatible within the experimental uncertainties; little discrepancy (within 3-4%) is found between FLUKA and GEANT4 code, mainly due to the different cross section libraries and the particle code transportation method which are implemented in the two software.

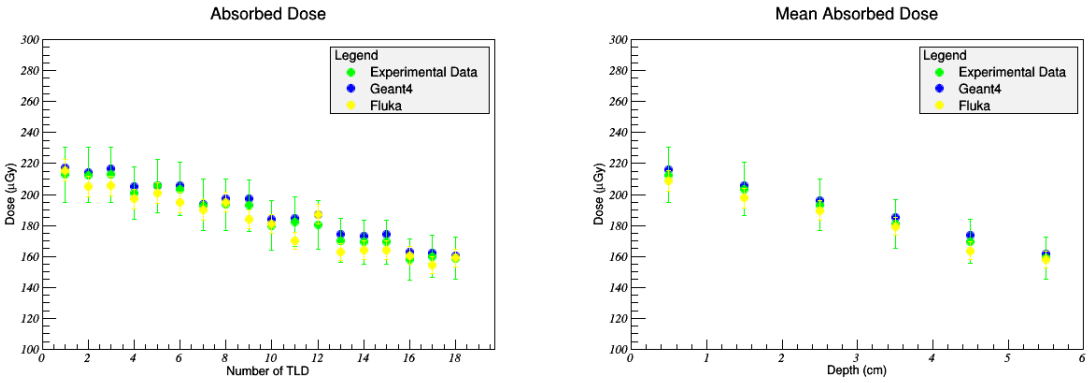

Figure 6.23: Dose absorbed by each TLDs chip (left side) and mean absorbed dose (average of the three TLDs on the same slice, right side). Green dots represent the experimental measurements (with a uncertainty of 5-7%), blu dots represent the GEANT4 results (uncertainty less than 0.1 %) whilst yellow dots represent FLUKA results (uncertainty of 3%).

Further measurements were then performed at the SYRMEP beamline using the mammographic setup presented in chapter 2: the Plexiglas phantom was positioned at the breast reference point (see Fig.3.3, chapter 3) where the ionization chambers of the SYRMEP beamline are calibrated.
The energetic range was varied from 18 keV to 38 keV.
The compressor plate system was implemented into the GEANT4 MC code: a frontal plate of 2.1 mm thickness made by plexiglass and a bottom plate of 1.7 mm thickness made by carbon fiber compose the compression system (Fig. 6.24).

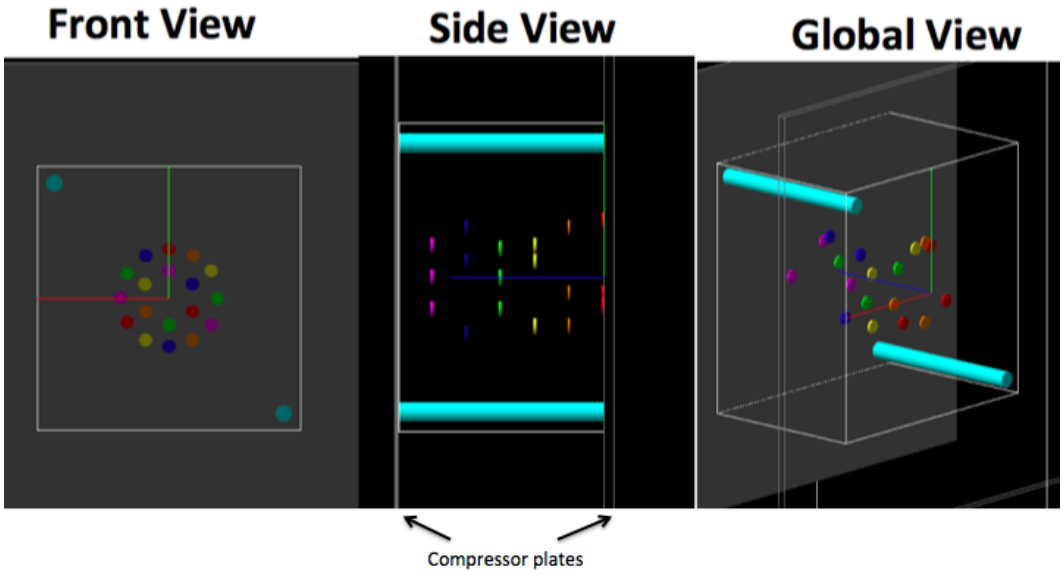

Figure 6.24: Phantom simulation in the SYRMEP setup with the two compressor plates.

The experimental dose is evaluated using Eq. (6.8) and the uncertainty is evaluated using Eq. (6.9) where a factor u^2_{IOC} (5%) is added for taking into account the uncertainty on the

air-kerma measured by the ionization chamber: this leads to a total uncertainty between 7-9%. Tab. (6.6) summarizes the parameters for the comparison between experimental and simulated dose.

	18 keV	20 keV	24 keV	26 keV	28 keV	33 keV	38 keV
$(\mu/\rho)_{en}^{LiF}\ (cm^2/g)$	0.924	0.663	0.375	0.293	0.232	0.142	0.093
$(\mu/\rho)_{en}^{Water}\ (cm^2/g)$	0.764	0.548	0.310	0.242	0.192	0.117	0.080
Ratio	1.209	1.211	1.213	1.211	1.209	1.205	1.171
Exp. Fluence (γ/mm^2)	2.20e6	2.22e6	8.89e7	6.75e7	9.19e7	8.07e7	8.70e7
Sim. Fluence (γ/mm^2)	1.23e5	1.23e5	1.23e5	1.23e5	1.23e5	1.23e5	1.23e5
Scale Factor	17.820	17.982	720.090	546.750	744.390	653.670	704.295
Energy Response (E_i)	0.74	0.77	0.85	0.87	0.90	0.96	0.97

Table 6.6: Parameters used for the comparison between experimental and simulation results.

Results are shown in Figs (6.25 and 6.26).

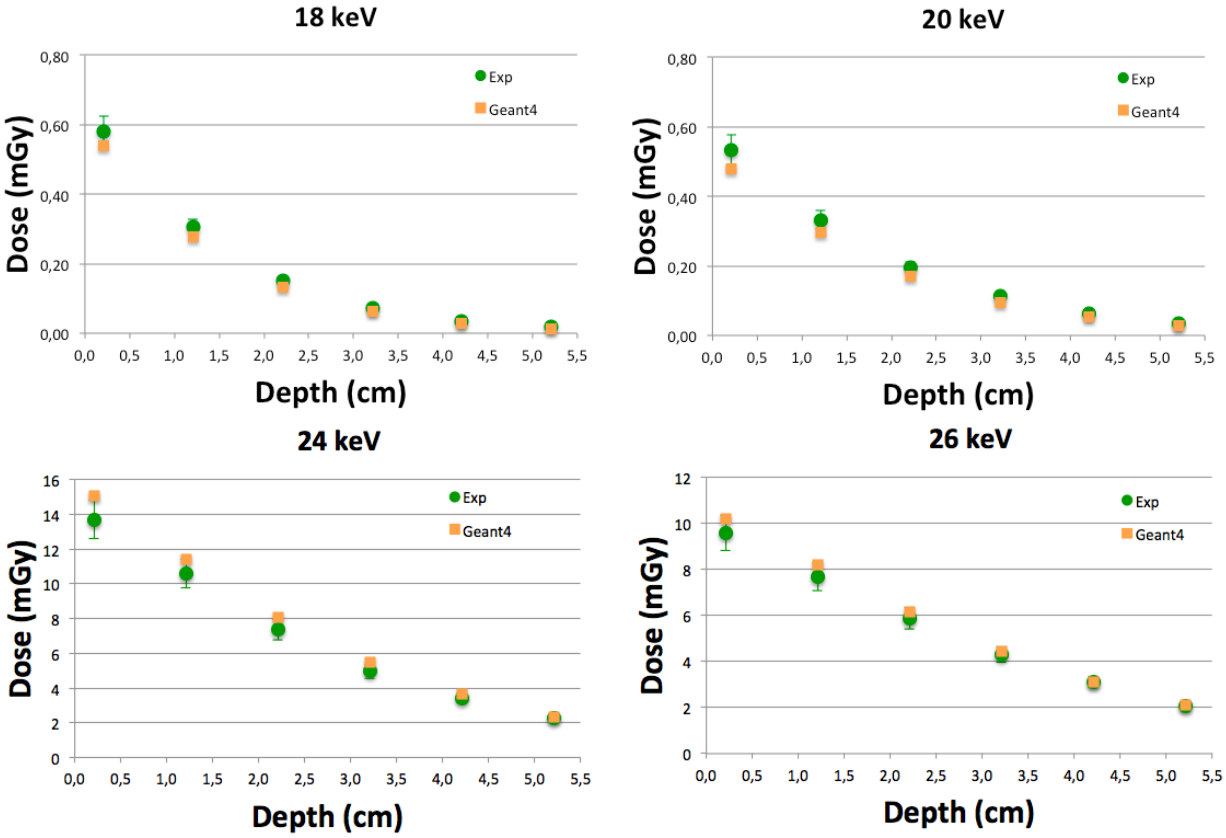

Figure 6.25: Comparison between experimental dose (green dots) and MC results (orange squares) for 18, 20, 24, 26 keV: the values are obtained averaging the dose deposit on the three TLDs of the same slice.

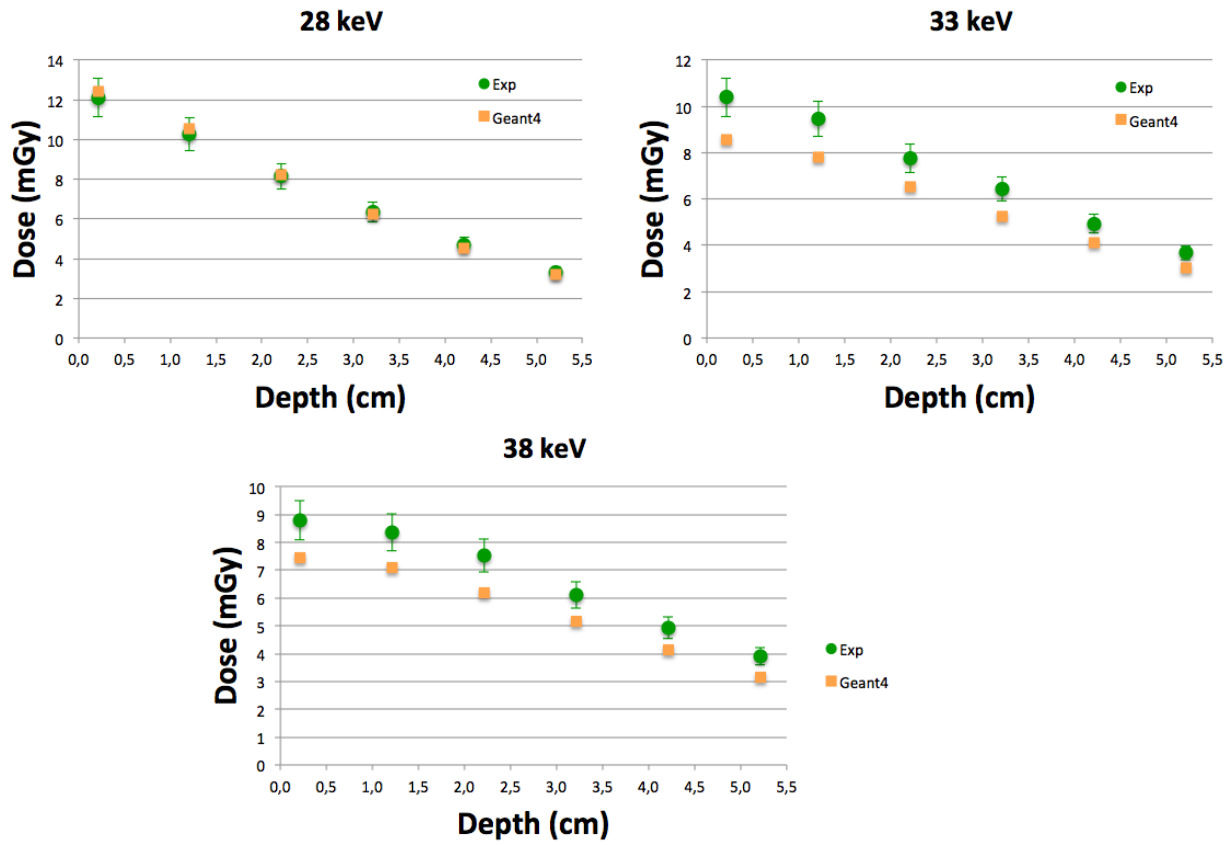

Figure 6.26: Comparison between experimental dose (green dots) and MC results (orange squares) for 28, 33, 38 keV: the values are obtained averaging the dose deposit on the three TLDs of the same slice.

The results show a good agreement (within the experimental uncertainty of 9%) in the energetic range 18-28 keV, while for the energies 33 keV and 38 keV the simulation underestimated the experimental values of 10-15%. This is probably related to the fact that the calibration of the ionization chambers of the SYRMEP beamline was done in the range 9-28 keV while an inter-comparison between a RADCAL ionization chamber was used for energies up to 40 keV and not the primary standard. However, if the error bar is expanded (k=2) all the measurements are compatible.
Future TLDs measurements (after the extension of the IOC calibration up to 40 keV) have been scheduled to confirm the results.
TLD chips were also used for better investigating the response of GR-200A to monoenergetic radiation with respect to a calibrated ^{60}Co gamma-ray source. Results are pubblished in (Emiro *et al.*, 2015).

GAF Measurements

The radiochromic films XR-QA2 (same type of the one already described in chapter 5) were used for the quantitative imaging of the synchrotron radiation beam.
The measurements were performed within the SYRMA-CT collaboration, in particular within the dosimetry group of University "Federico II", Naples (Italy).
The aim of the measurements is to experimentally asses the beam distribution in a plane transverse to the beam propagation direction. The 2D distribution of the photon fluence at the isocenter were obtained after calibration with an ionization chamber in terms of air kerma.
All the results of these measurements are deepen exposed in (Di Lillo *et al.*, 2015) while here only the main results are exposed.

Figs. (6.27) show the horizontal (a) and vertical (b) synchrotron radiation beam profile at 28 keV: maximum variation of 20% and 37% were observed with respect to the peak value.

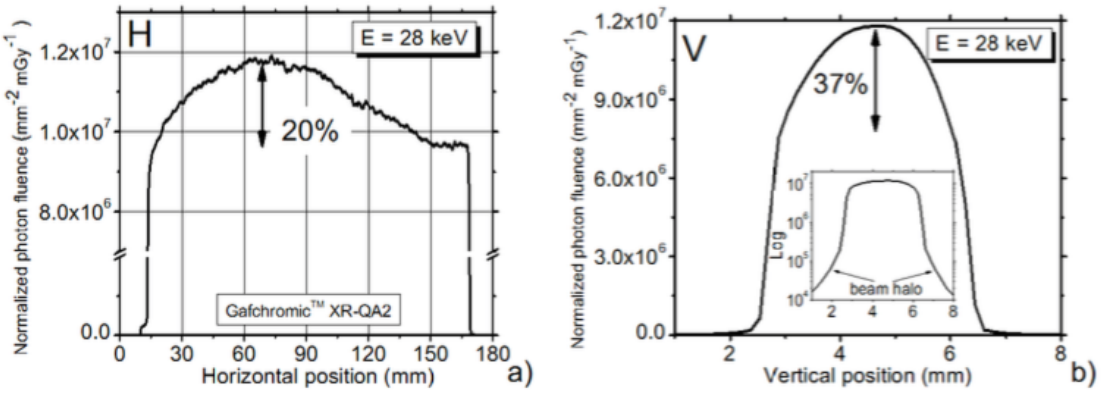

Figure 6.27: a) Horizontal (H) and b) vertical (V) profiles of SR beam at 28 keV obtained by radiochromic film. The insert in (b), in log scale, highlights a low-intensity scatter signal at the periphery of the beam (Di Lillo *et al.*, 2015).

The beam profiles obtained at 40 keV are shown in Fig. (6.28): in this case a maximum horizontal non-uniformity of 15% was found while the variation of about 64% in the vertical direction is attributed to the misalignment of the slits system with the peak.

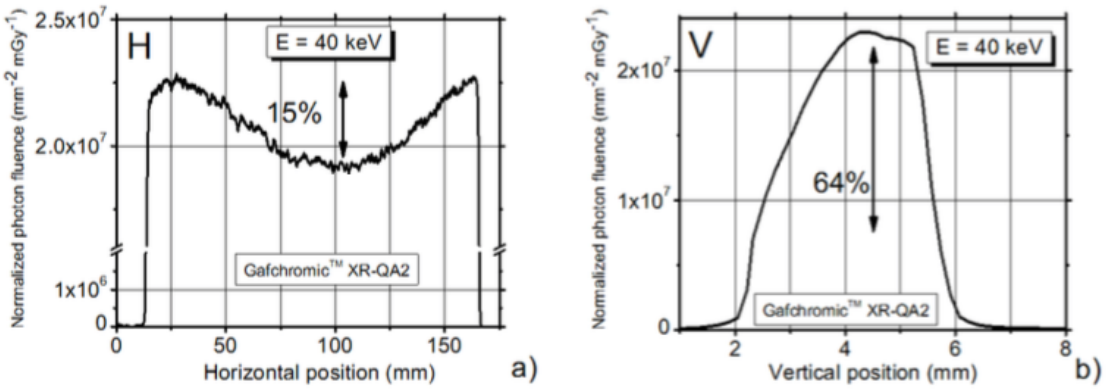

Figure 6.28: a) Horizontal (H) and b) vertical (V) profiles of SR beam at 40 keV obtained by radiochromic film. Maximum variation of 15% (H) and 64% (V) were observed (Di Lillo *et al.*, 2015).

The radiochromic film provides the 2D distribution of the beam intensity in terms of photon fluence per unit of air kerma. The observed variation ranges from 15% to 64% over the whole beam. This indicates that, for better evaluating the dose distribution using the MC code, the real beam shape might be implemented using the beam intensity measured by radiochromic film XR-QA2. Moreover, the radiochromic films may have the potential to on-line monitor the beam intensity for each breast-ct exam (this hypothesis will be investigated with future measurements).
Moreover, thanks to these results it was possible to notice that an horizontal variation of 15% is too high and that might be caused by the monochromator: for this reason a technical maintenance to the monochromator was planned and performed.

Chapter 7

Results

This chapter presents the application of the Monte Carlo code, discussed and validated in chapter 6, to the specific case of the SYRMA-CT project. Several cases which will be useful to the SYRMA-CT project are proposed.
The results presented hereby have also been published in Mettivier *et al.* (2016).

1 Dose evaluation for the SYRMA-CT project

The estimation of the mean glandular dose (MGD) is the aim of the dosimetric assessment for the clinical evaluation of the dose in mammography.
The evaluation of the MGD is obtained multiplying the entrance surface air kerma (ESAK) by the normalized glandular dose coefficients (DgNs, see chapter 4) according to the following formula:

$$MGD = DgN \cdot ESAK \tag{7.1}$$

While the ESAK is directly measured by the ionization chamber on the beam line (see chapter 3), the DgN can only be estimated by Monte Carlo (MC) methods.
The MC code developed within the SYRMA-CT project gives the DgN_{CT} which will be used for the MGD evaluation.
In the SYRMA-CT the idea is to irradiate a partial breast volume vertically shifting the patient support with a 3 mm step (i.e. the beam height). The condition of partial breast irradiation is different from that of (full field) 2D mammography (Dance (1990) and Wu *et al.* (1994)), of digital breast tomosynthesis (Sechopoulos (2013a) and Sechopoulos (2013b)) as well as of breast computer tomography (Boone *et al.* (2004) and Kalender *et al.* (2012)). In the dosimetric protocols adopted for these 2D and 3D imaging techniques, the whole breast volume is always irradiated and the definition of MGD refers to the total energy (E_g) deposited in the glandular tissue, divided by the total glandular mass (M_g), according to

$$MGD = \frac{M_g}{E_g} \tag{7.2}$$

However, in the case of a partial breast irradiation, no protocols are available. Thus, if the MGD evaluation is based on the calculation of the energy deposited in the irradiated volume

(e_g), divided by the total glandular mass (M_g) of the breast, the MGD may be underestimated. In fact, since there is no scatter dose, e_g is lower than E_g. For this reason, a specific dosimetric evaluation is needed.
In an analogous way, as MGD is defined through Eq. (7.2), in the case only a fraction of the breast volume is irradiated, a quantity MGD_v can be calculated as follows:

$$MGD_v = \frac{e_g}{m_g} \tag{7.3}$$

where e_g is the energy deposited only in the glandular mass and m_g is the glandular mass of the irradiated volume.
However, when a partial irradiation is taken into account, also the dose delivered to the glandular tissue outside the irradiated volume has to be considered: this dose comes from the radiation scatter to the breast regions adjacent to the irradiated ones. A third quantity MGD_t can be defined as the ratio between the total energy deposited in the whole breast (E_g) and the glandular mass in the irradiated volume (m_g):

$$MGD_t = \frac{E_g}{m_g} \tag{7.4}$$

The simulated set up is shown in Fig. (7.1): the breast has a cylindrical shape and a height of 1.5 times the sample radius (as indicated in Boone *et al.* (2004)), whilst a water box (with a volume of 13.5 dm^3) is added for simulating the body of the patient.
The skin thickness is 1.45 mm (according to Huang *et al.* (2008) and Shi *et al.* (2013)).

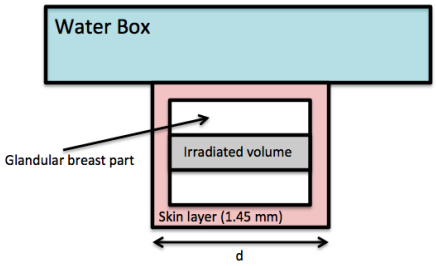

Figure 7.1: Sketch of the simulated setup. The total irradiation field was set according to the irradiated volume height. A water box was added to simulate the patient body.

In order to match the characteristics of the synchrotron radiation beam, the radiation field shape is set to a rectangle with fixed height (3 mm) and variable horizontal dimension (according to the breast diameter).
The simulation parameters are:

- Primary particles: 1 million photons;
- Simulations repeated 9 times using different seeds for achieving a COV value lower than 1%;
- Several glandular fractions (0%, 14.3%, 25%, 50%, 75%, 100%) with the chemical composition set in accordance to (Hammerstein *et al.*, 1979)

Fig. (7.2) shows the simulation results for the MGD (Eq. 7.2) when only a slice of 3 mm is irradiated.

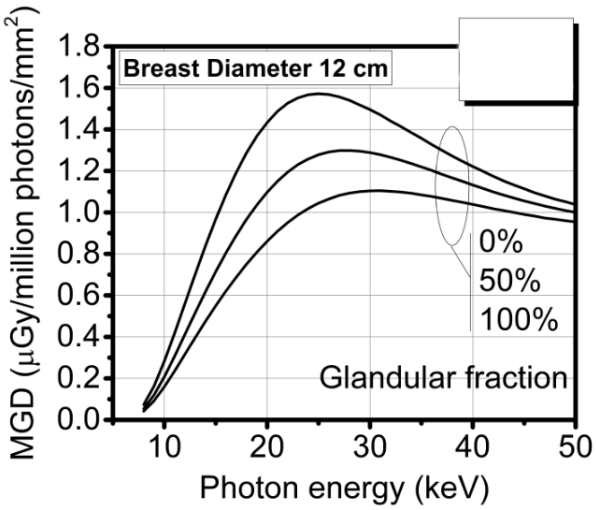

Figure 7.2: *MGD* calculated on the entire breast mass as a function of photon energy when only a slice of 3 mm is irradiated.

Results for MGD_t and MGD_v for a breast diameter of 12 cm are shown in Fig. (7.3) as a function of energy, when only a slice of 3 mm is irradiated.

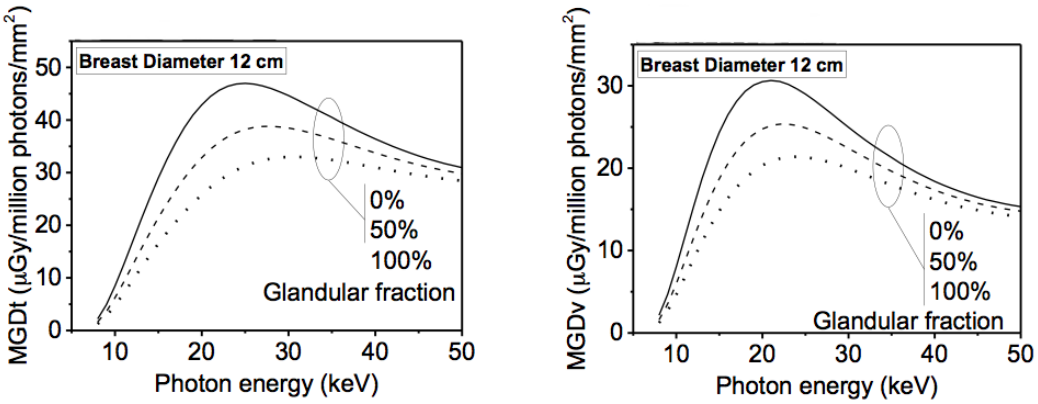

Figure 7.3: MGD_t (on the left) and MGD_v (on the right) in a 3 mm volume irradiation height. In all simulations the photon fluence was kept constant.

The values obtained from Fig. (7.2) are lower than those obtained from Fig. (7.3). This is due to the evaluation of a larger mass: the MGD_t and the MGD_v seem to better estimate the real dose delivered to the breast tissue.
The use of the MGD quantity can lead to a high underestimation of the dose delivered as the mass is considered hypothesizing that the phantom's height is 1.5 times the radius of the breast at the chest wall.
Four different cases are then analyzed to gather together several quantities combination according to Fig. (7.4): the energy deposited can be E_g or e_g and the glandular mass can be M_g or m_g.

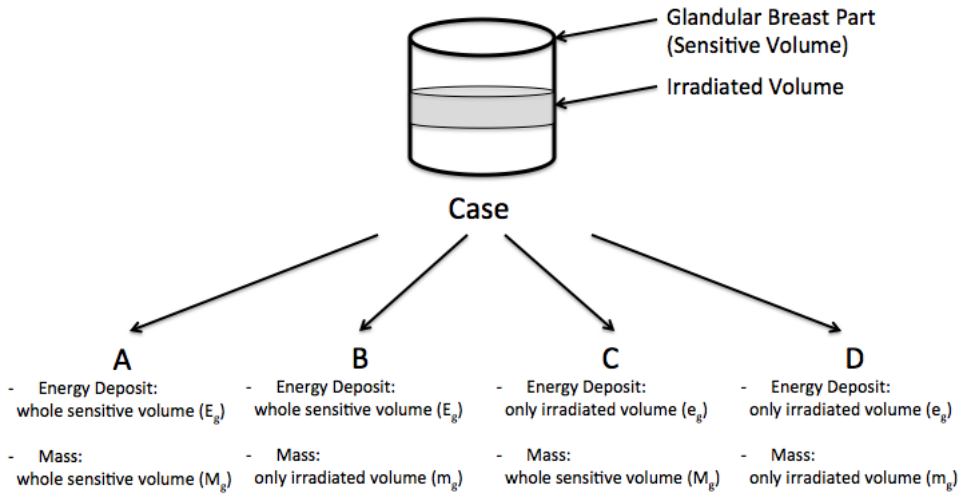

Figure 7.4: Different cases taken into account for the analysis.

Results for the DgN_{CT} quantities related to Fig. (7.4) will be discussed in the next section. The height of the irradiated volume was gradually increased (see Fig. 7.5) for better quantifying the differences of the several scenarios.

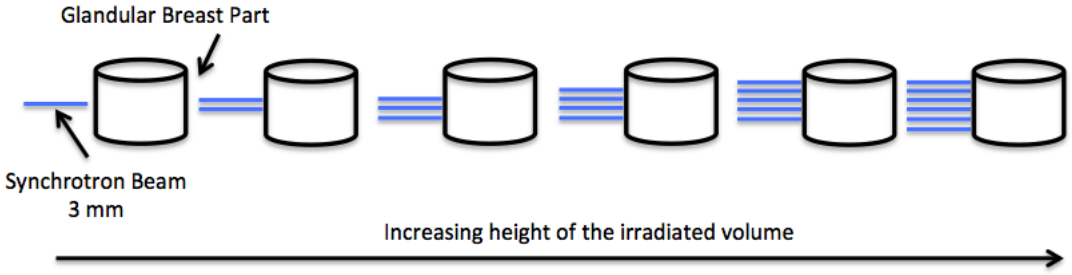

Figure 7.5: The irradiated volume was gradually increased for quantifying the differences from the several scenarios reported in Fig. (7.4): the synchrotron beam increased from 3 mm up to 90 mm (i.e. the maximum height for a 12 cm breast diameter).

Fig. (7.6) shows the results for all four cases for a 12 cm breast diameter (height 9 cm) with a glandular fraction of 50%, at the fixed energy of 38 keV (the energy value that will be adopted in the SYRMA-CT project), as a function of the height of the irradiated volume.

From Fig. (7.6) it is possible to notice the linear dependence of the MGD (case A, blue line) from the height of the irradiated volume, which is due to the linear increase of the deposited energy with the vertical dimension of the irradiated volume.

On the other hand, the MGD_v (case D, green line) increases with a sub-linear trend with the increasing of the vertical dimension of the irradiated volume, in that the deposited energy increases together with the glandular mass of the irradiated volume.

For the MGD_t (case B, red line), the energy is deposited throughout the whole breast but the glandular mass is that of the irradiated volume. This dose value is almost constant with a little decrease with the vertical dimension of the irradiated slice in that when the irradiated area approximates the size of the entire breast the energy delivered outside the slice is gradually

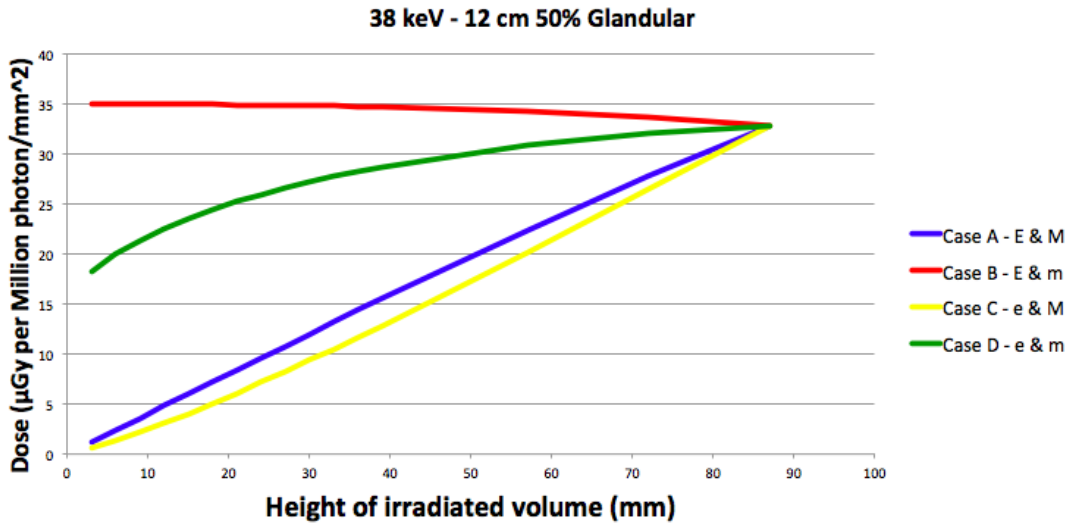

Figure 7.6: Case A (blue line) is the MGD of the glandular mass present in the whole breast, case B (red line) is the MGD_t in the irradiated volume to which the contribution from scatter dose is added, case C (yellow line) is the MGD when the whole glandular breast mass is taken into account without scatter contribution and case D (green line) is the MGD_v in the irradiated volume without the contribution from scatter dose. All data are for a 12 cm diameter breast phantom with a glandular fraction of 50%, taken varying the dimension of the irradiated volume with a 3 mm height beam. The photon energy of the monoenergetic beam was 38keV.

smaller. Case C (yellow line) shows a similar trend to case A as there is a linear dependence from the height of the irradiated volume. However, it is always lower because there is no scatter dose.

The use of the MGD (case A) in a partial breast irradiation could lead to an underestimation of the delivered dose as indicated in Fig. (7.6), where a single slice of 3 mm height is irradiated. The value of this underestimation depends on the dimensions of the irradiated breast, Fig. (7.6), and, in particular, it increases with the decrease of the irradiated volume, up to 97% in the case of the irradiation of a single slice of 3 mm (compared to case B, MGD_t).
MGD_t and MGD_v values provide a more accurate and precautionary estimation of the dose deposited in the organ, compared to the MGD. In particular, from Fig. (7.6), the MGD_t values are almost independent from the dimensions of the irradiated volume and this is similar to the MGD values for the whole irradiation.
In addition, the close proximity between the MGD_t and the CDTI concept (see chapter 4) has to be noticed.

1.1 Normalized Glandular Dose (DgN) Coefficients

The DgN coefficients which will be used in the Eq. (7.1) for the different cases shown in Fig. (7.4) are now presented.
The irradiated volume (see Fig. 7.1) has a 3 cm height, in accordance to the one planned to be irradiated in the SYRMA-CT project.

Case A

Case A represents the scenario in which there is an underestimation of the dose delivered during the exam: in this case the mass of the breast (M_g) is higher than the mass of the irradiated zone. The energy deposit includes the scatter radiation outside the irradiated volume.
As the height of the breast is fixed (i.e. 1.5 times sample radius), it could be hypothesized that if increasing that height (i.e. considered more mass), the DgN_{CT} would decrease, leading to a lower value.
The DgN_{CT} values for this case are exposed in appendix B.1.

Case B

Case B represents the scenario in which the scatter radiation outside the irradiated volume is counted as if the energy deposit took place in the irradiated slice. This is the most conservative case as all the energy deposit is taken into account.
The DgN_{CT} values for this case are exposed in appendix B.2.
The quantity MGD_t, Eq. (7.4), will be calculated using these DgN_{CT} (appendix B.2).

Case C

Case C represents the worst scenario in which no scatter radiation is taken into account and the mass is that of the whole breast: these conditions underestimated the dose both for the scatter contribution and for the mass, whose height can be set up arbitrarily.
The DgN_{CT} values for this case are exposed in appendix B.3.

Case D

Case D is the scenario in which the scatter radiation is not taken into account but the mass is the one of the irradiated volume: in this case there is an underestimation due to the fact the scatter radiation is not taken into account.
The DgN_{CT} values for this case are exposed in appendix B.4.
The quantity MGD_v, Eq. (7.3) will be calculated using these DgN_{CT} (appendix B.4).

Chapter 8

Conclusions

The evaluation of the dose delivered to the breast during an x-ray exam is a critical issue.
The clinical transition from a 2D mammography to a 3D examination requires suitable methods to evaluate the Mean Glandular Dose (MGD).
In breast tomography, the evaluation of the MGD is only possible using Monte Carlo (MC) simulations: with the MC code the Normalized Glandular Dose (DgN_{CT}) coefficients are obtained and the MGD is evaluated multiplying these coefficients by the measured air kerma at the scanner isocenter.
The aim of the SYRMA-CT collaboration is to set-up the first Breast Computed Tomography (BCT) clinical study using a non-conventional x-ray source: the Synchrotron Radiation (SR).
Since 2006, a clinical study of Mammography with Synchrotron Radiation (MSR) has been carried out at Elettra, the Italian synchrotron light source in Trieste. MSR showed great potential both for diagnostic evaluations and dose reduction (Castelli and et al. (2011) and Longo *et al.* (2014)).
Since 2014, the SYRMA-CT project has been investigating the feasibility of a BCT using SR. Thus, the evaluation of the MGD assumes a key-role.
Due to the peculiarity of the x-ray source used and to the novelty of the 3D BCT examination, no literature is available for the MGD evaluation, with these specific requirements.
Suitable parameters and new methods for evaluating the MGD for BCT-SR have been developed in this PhD thesis.
A MC code was created using the toolkit GEANT4: a careful selection of the main parameters to be implemented was performed. GEANT4 offers to the users several choices for implementing MC simulations especially for the PhysicsList (i.e. the physics processes which are simulated): the main options for the medical physics applications were analyzed (Fedon *et al.*, 2015).
The MC code was validated with previous pubblished work of Boone (Boone (2002) and Boone *et al.* (2004)), reproducing the setup described by the author. Experimental measurements were performed at the SYRMEP beamline for validation purposes: these measurements involve the use of an ionization chamber (RADCAL) for the Computed Tomography Dose Index (CTDI) evaluations, ThermoLuminescence Dosimeters (TLD) (Emiro *et al.*, 2015) and XR-QA2 radiochromic films (GAF) (Di Lillo *et al., 2015*). All the validation measurements showed good agreement between experimental and MC data (Mettivier *et al.*, 2016).

Two parameters are found to be suitable for evaluating the dose in the BCT-SR exam (Mettivier *et al.*, 2016): MGD_t, which takes into account the scatter dose outside the irradiated region, and the MGD_v, which considers only the dose delivered within the irradiated zone (i.e. without the scatter radiation).
MGD_t assumes values similar to the MGD value when a whole breast irradiation is performed and its concept is very close to the CTDI one.
The use of MGD_v instead of MGD_t can lead to an underestimation of the dose delivered up to 97% when a single slice of 3 mm height is irradiated (Mettivier *et al.*, 2016).
The evaluation of the MGD, obtained using the MC code developed during this PhD activity, has already been used in experimental measurements on two breast specimens (Longo *et al.*, 2016).
The MC code is being used also for the definition of the protocol exam to be submitted to the Ethic Committee and for the clinical exam optimization. Further ongoing studies concern:
(i) The dose distribution delivered to the patient breast, implementing a voxelized geometry into the MC code. This study will lead to the possibility of a specific patient-dose evaluation, with the prospective of implementing into the code the real breast shape and composition.
(ii) Irradiation modalities that could be performed at the mammographic facility of Elettra light source (e.g spiral CT).

Appendix A

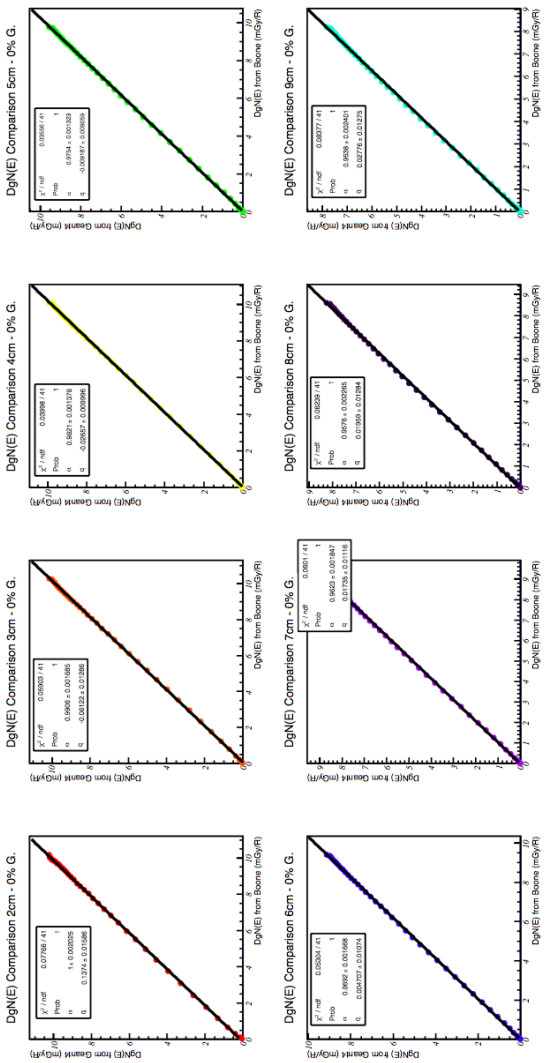

Figure A.1: Linear correlation between Boone data (Boone, 2002) (on abscissa) and MC data obtained by GEANT4 (on ordinate) for 0% glandular fraction: excellent correlation is found.

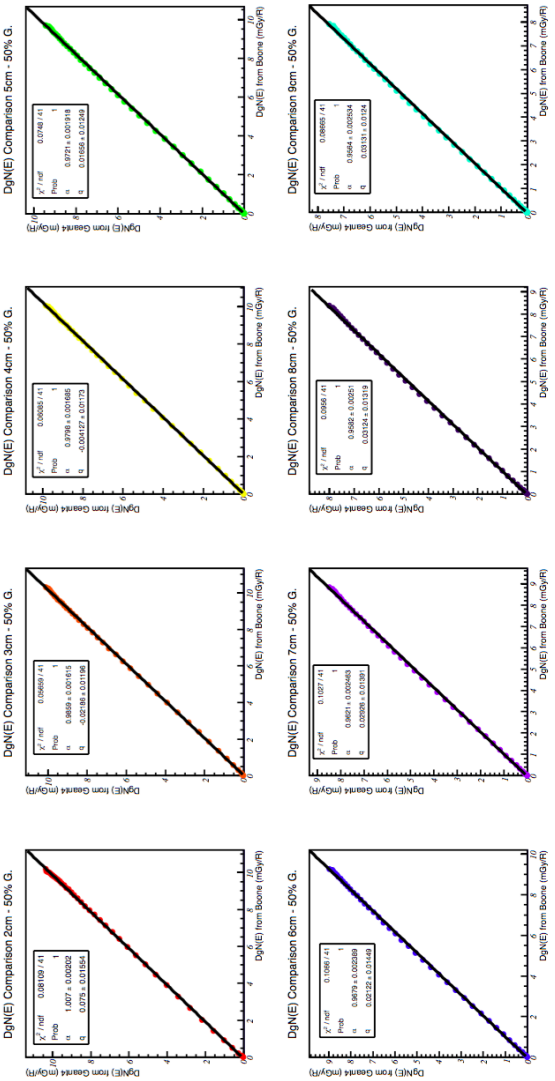

Figure A.2: Linear correlation between Boone data (Boone, 2002) (on abscissa) and MC data obtained by GEANT4 (on ordinate) for 50% glandular fraction: excellent correlation is found.

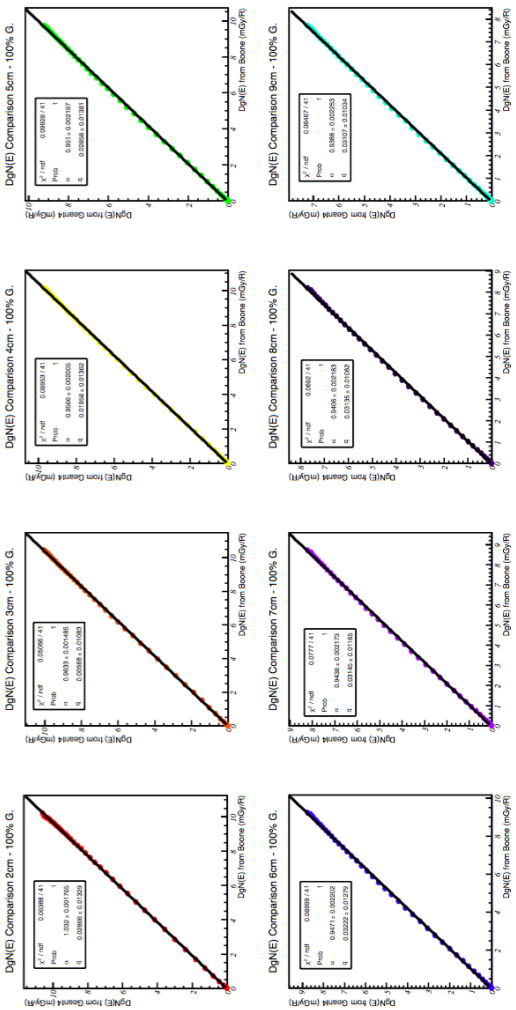

Figure A.3: Linear correlation between Boone data (Boone, 2002) (on abscissa) and MC data obtained by GEANT4 (on ordinate) for 100% glandular fraction: excellent correlation is found.

Appendix B

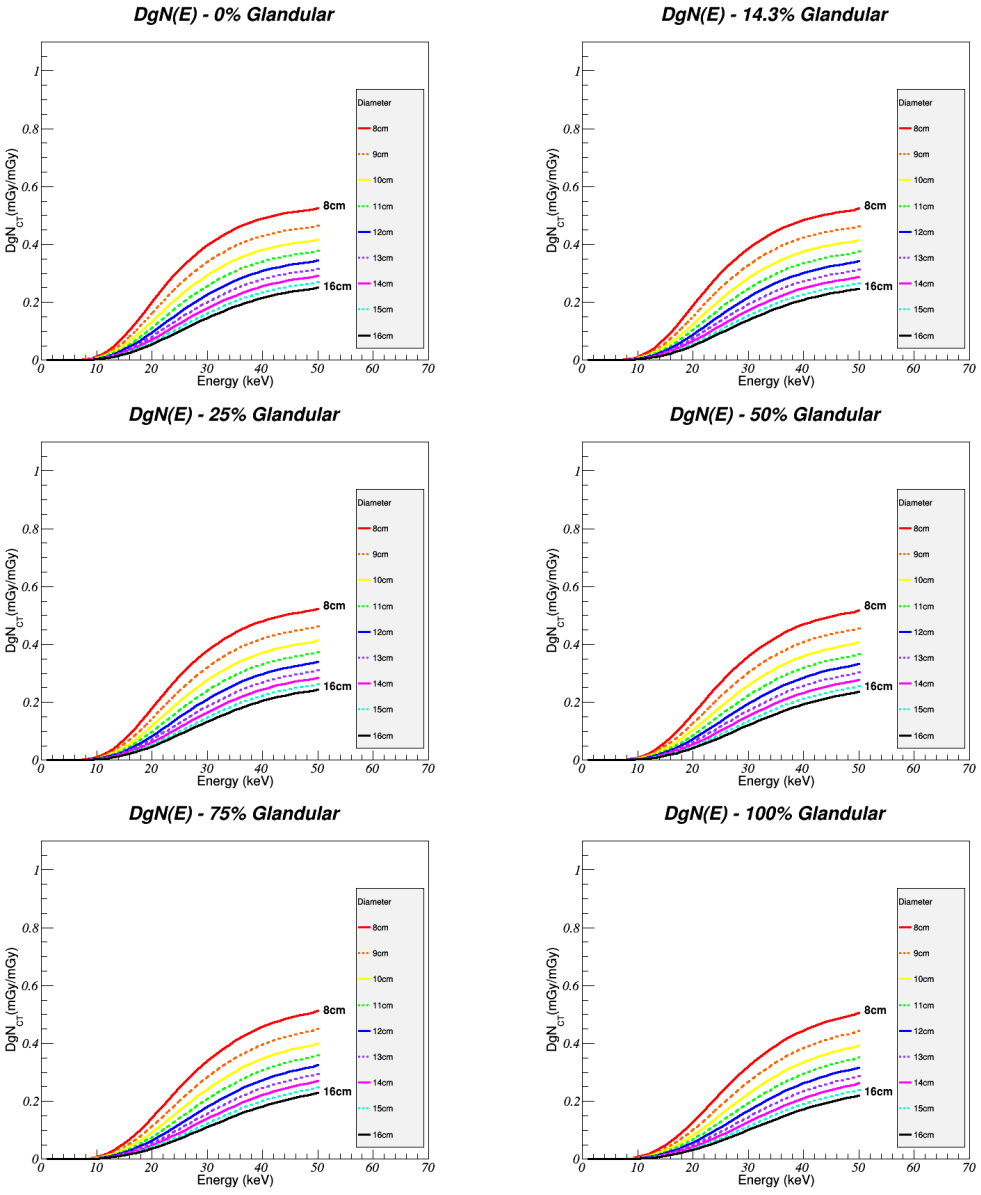

Figure B.1: DgN values for several glandularity fraction. The irradiation scenario was the one presented in case A (Fig.7.4) which considers an irradiated volume of 3 cm height, the energy deposited and the mass are the ones of the whole glandular breast part.

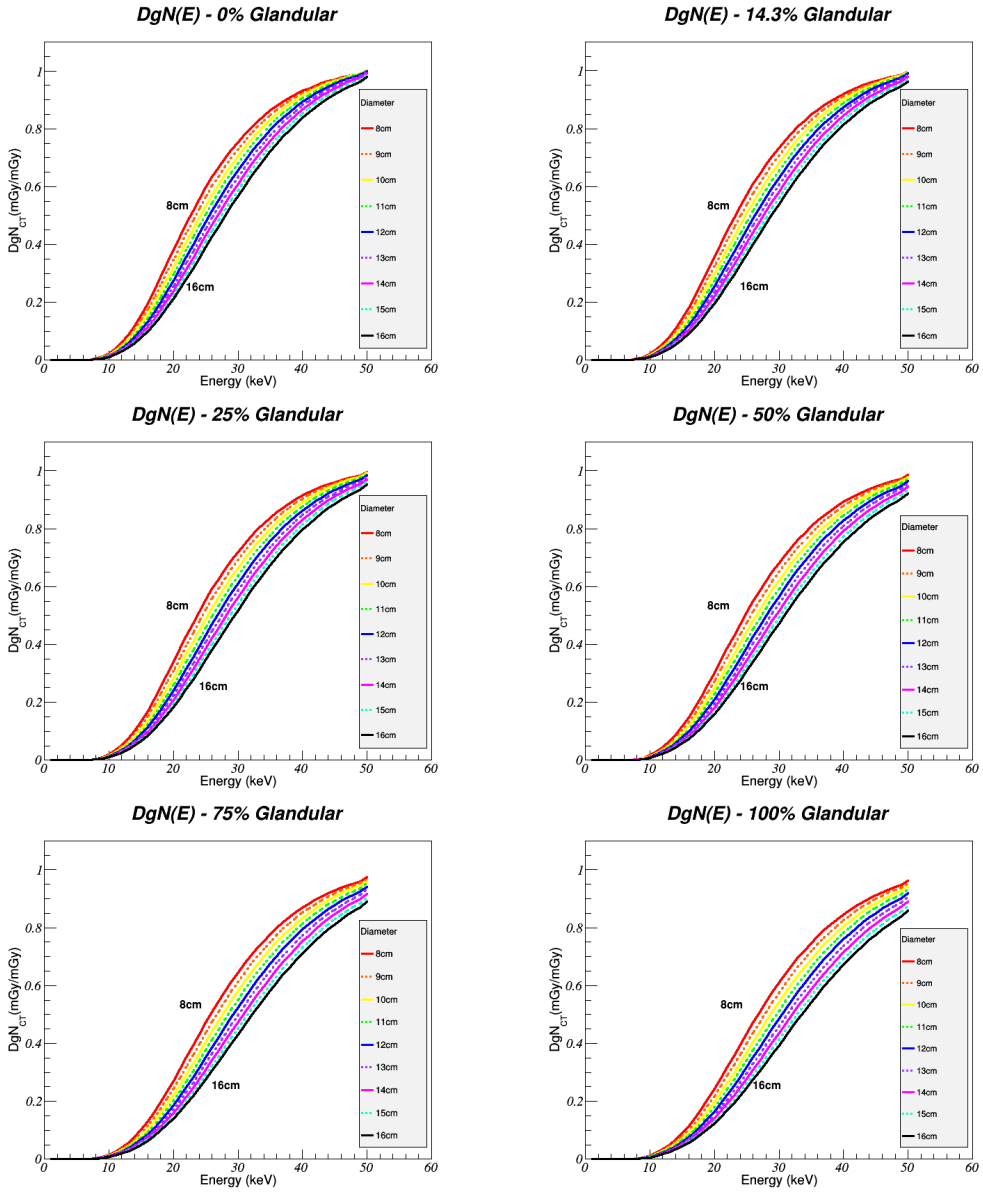

Figure B.2: DgN values for several glandularity fraction. The irradiation scenario was the one presented in B (Fig.7.4) which considers an irradiated volume of 3 cm height, the energy deposited on whole breast and the mass of only the irradiated volume.

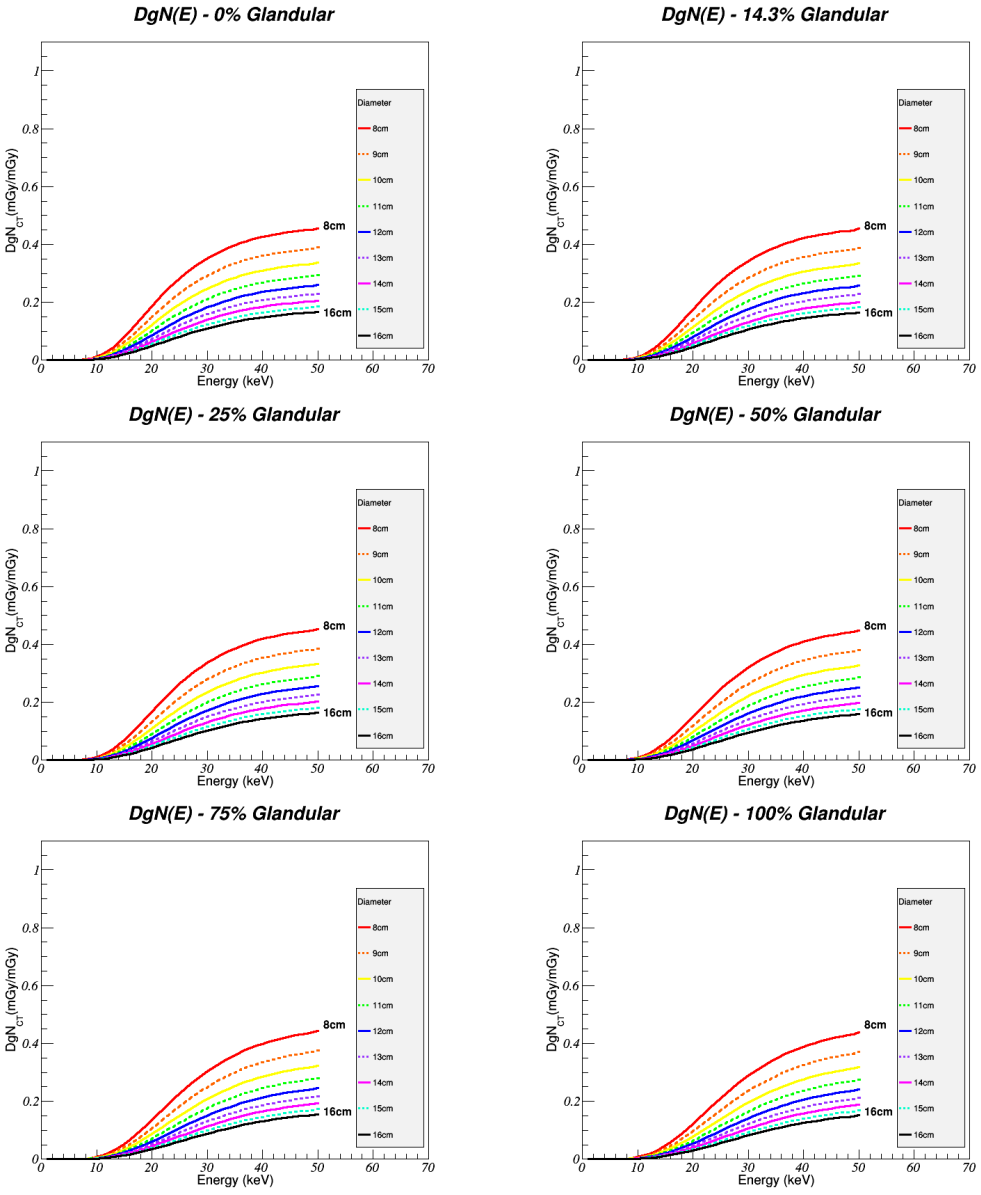

Figure B.3: DgN values for several glandularity fraction. The irradiation scenario was the one presented in C (Fig.7.4) which considers an irradiated volume of 3 cm height, the energy deposited only on the irradiated volume and the mass of the whole glandular breast part.

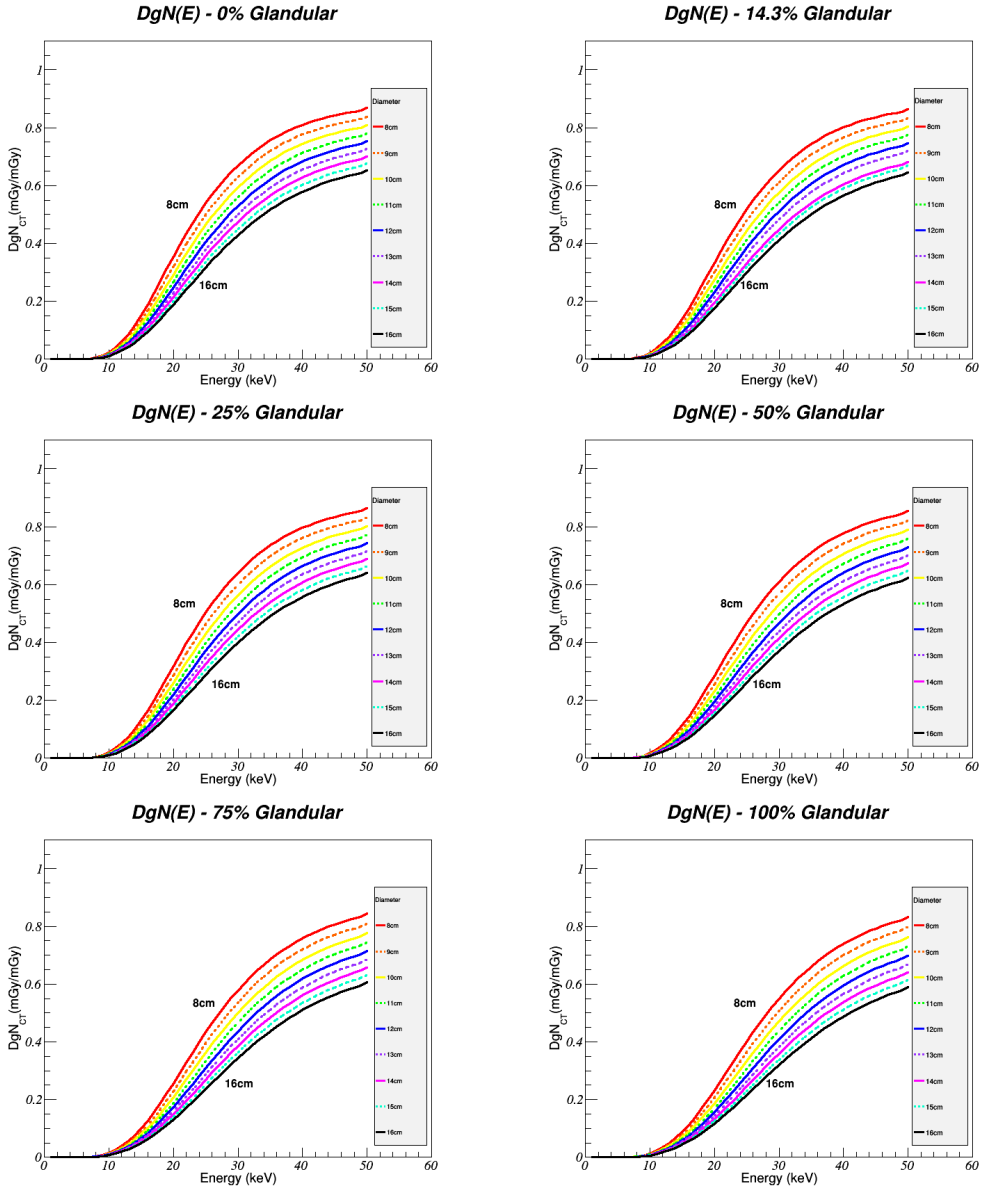

Figure B.4: DgN values for several glandularity fraction. The irradiation scenario was the one presented in D (Fig.7.4) which considers an irradiated volume of 3 cm height, the energy deposited and the mass are only of the irradiated volume.

Bibliography

AAPM. *Report 11 Comprehensive Methodology for the Evaluation of Radiation Dose in X-ray Computed Tomography*. 2010.

S. Agostinelli and et al. Geant4 - a simulation toolkit. *Nucl. Instrum. and Methods in Physics Research A*, (506):250–303, 2003.

H. Alnawaf, P. Yu, and M. Butson. Comparison of epson scanner quality for radiochromic film evaluation. *J. Appl. Clin. Med. Phys.*, (13(5)):314–21, 2012.

F. Arfelli and et al. Low-dose phase contrast x-ray medical imaging. *Phys. Med. Biol.*, (43(10)):2845–52, 1998.

F. Arfelli and et al. Mammography with synchrotron radiation: phase-detection technique. *Radiology*, (215(1)):286–93, 2000.

G. Battistoni, S. Muraro ans P. R. Sala, F. Cerutti, A. Ferrari, S. Roesler, A. Fasso, and J. Ranft. The fluka code: Description and benchmarking. *Proceedings of the Hadronic Shower Workshop*, (896):31–49, 2007.

M. Beister, D. Kolditz, and W. A. Kalender. Iterative reconstruction methods in x-ray ct. *Physica Medica*, (28):94–108, 2012.

R. Bellazzini, G. Spandre, A. Brez, M. Minuti, M. Pinchera, and P. Mozzo. Chromatic x-ray imaging with a fine pitch cdte sensor coupled to a large area photon counting pixel asics. *J. Instrum*, (8):C02028, 2013.

L. A. Benevides and D. E. Heintenlang. Characterization of metal oxide semiconductor field effect transistor dosimeters for application in clinical mammography. *Med. Phys.*, (33 (2)):514–20, 2006.

J. M. Boone, N. Shah, and T. R. Nelson. A comprehensive analysis of dgn_{CT} coefficients for pendant-geometry cone-beam breast computed tomography. *Med. Phys.*, (31):226–35, 2004.

J. M. Boone, A. L. C. Kwan, J. A. Seibert, N. Shah, K. K. Lindfors, and T. R. Nelson. Technique factors and their relationship to radiation dose in pendant geometry breast ct. *Med. Phys.*, (32):3767–76, 2005.

J. M. Boone. Glandular breast dose for monoenergetic and high-energy x-ray beams: Monte carlo assessment. *Radiology*, (213):23–37, 1999.

J. M. Boone. Normalized glandular dose (dgn) coefficients for arbitrary x-ray spectra in mammography: computer-fit values of monte carlo derived data. *Med. Phys.*, (29):869–75, 2002.

M. Bovi and et al. Absolute air-kerma measurement in a synchrotron radiation beam by ionization free-air chamber. *Conference procedings*, 2006.

M. W. Bower and D. E. Hintenlang. The characterization of a commercial mosfet dosimeter system for use in diagnostic x ray. *Health Phys.*, (75):197–204, 1998.

P. M. Bradley, A. M. Speidel, L. Tina Pike, and S. M. Van Lysel. Calibration of gafchromic xr-rv3 radiochromic film for skin dose measurement using standarized x-ray spectra and a commercial flatbed scanner. *Med. Phys.*, (38):1918–30, 2011.

S. Brady, T. Yoshizumi, G. Toncheva, and D. Frush. Implementation of radiochromic film dosimetry protocol for volumetric dose assessments to various organs during diagnostic ct procedures. *Med. Phy.*, (37 (9)):4782–92, 2010.

Anders Brahme. *Comprehensive biomedical physics*. Elsevier, 2014.

A. Bravin, P. Coan, and P. Suortti. X-ray phase-contrast imaging: from pre-clinical applications towards clinics. *Phy. Med. Biol.*, (58):R1–R35, 2014.

D. T. Burns, M. Bovi, and M. P. Toni. Comparison of the air-kerma standards of the enea-inmri and the bimp in the low-energy x-ray range. *Rapport BIPM 99/11*.

M. J. Butson, A. Rozenfeld, J. N. Mathur, M. Carolan, T. P. Wong, and P. E. Metcalfe. A new radiotherapy surface dose detector: the mosfet. *Med. Phy.*, (23 (5)):655–58, 1996.

E. Butson, H. Alnawaf, P. K. N. Yu, and M. Butson. Scanner uniformity improvements for radiochromic film analysis with matt reflectance backing. *Australas Eng. Phys. Sci Med.*, (34):401–7, 2011.

E. Castelli and et al. Clinical mammography at the syrmep beam line. *Nucl. Instrum. Methods Phys. Res. A*, (572(1)):237–40, 2007.

E. Castelli and et al. Mammography with synchrotron radiation: first clinical experience of phase-detection technique. *Radiology*, (259(3)):684–694, 2011.

R. C. Chen and et al. Measurment of the linear attenuation coefficients of breast tissues by synchrotron radiation computed tomogrpahy. *Phys. Med. Biol.*, (55):4993–5005, 2010.

European Commission. *European Guidelines on quality criteria for computed tomography*. Luxembourg: Office for Official Publications of the European Communities, 1999.

European Commission. *European Guidelines for Quality Assurance in Breast Cancer Screening and Diagnosis 4th edn*. Luxembourg: Office for Official Publications of the European Communities, 2006.

A.M. O' Connell, A. Karellas, and S. Vedantham. The potential role of dedicated 3d breast ct as a diagnostic tool: review and early clinical examples. *Breast Journal*, (20):592–605, 2014.

D. R. Dance, C. L. Skinner, K. C. Young, J. R. Beckett, and C. J. Kotre. Additional factors for the estimations of mean glandular breast dose using the uk mammography dosimetry protocol. *Phys. Med. Biol.*, (45):3225–40, 2000.

D. R. Dance, K. C. Young, and R. E. van Engen. Further factors for the estimation of mean glandular dose using the united kingdom european and iaea breast dosimetry protocols. *Phys. Med. Biol.*, (54):4361–72, 2009.

D. R. Dance, K. C. Young, and R. E. van Engen. Estimation of mean glandular dose for contrast enhanced digital mammography: factors for use with the uk, european and iaea breast dosimetry protocols. *Phys. Med. Biol.*, (59):2127–37, 2014.

D.R. Dance. Monte carlo calculation of conversion factors for the estimation of the mean glandular dose. *Phys. Med. Biol.*, (35(9)):1211–19, 1990.

M. de Denaro, P. Bregant, M. Severgnini, and F. de Guarrini. In vivo dosimetry for estimation of effective doses in multislice ct coronary angiography. *Med. Phy.*, (34):3705–10, 2007.

S. L. Dong, T. C. Chu, G. Y. Lan, T. H. Wu, Y. C. Lin, and J. S. Lee. Characterization of high-sensitivity metal oxide semiconductor field effect transistor dosimeters system and lif:mg,cu,p thermoluminescence dosimeters for use in diagnostic radiology. *Applied Radiation and Isotopes*, (57):883–91, 2002.

F. Emiro, F. Di Lillo, G. Mettivier, C. Fedon, R. Longo, G. Tromba, and P. Russo. Energy response of gr-200a thermoluminescence dosemeters to co-60 and to monoenergetic synchrotron radiation in the energy range 28-40 kev. *Radiation Protection Dosimetry*, pages 1–6, 2015.

C. Fedon, E. Quai, F. Arfelli, D. Dreossi, L. Rigon, M. Tonutti, G. Tromba, M.A. Cova, and R. Longo. Phase-contrast mammography with synchrotron radiation dosimetric results. *10.1594/ecr2014/C-1253*, 2014.

C. Fedon, F. Longo, G. Mettivier, and R. Longo. Geant4 for breast dosimetry: parameters optimitation study. *Phys. Med. Biol.*, (60):311–23, 2015.

A. Ferrari, P. R. Sala, A. Fasso, and J. Ranft. Fluka: a multi-particle transport code. *CERN-2005-10*, 2005.

R. Fitzgerard. Phase-sensitive x-ray imaging. *Phys. Today*, (51(8)):866–84, 2000.

N. Geeraert, R. Klausz, S. Muller, I. Bloch, and H. Bosmans. Evaluation of exposure in mammography: limitations of average glandular dose and proposal of a new quantity. *Radiation Protection Dosimetry*, pages 1–4, 2015.

T. Giaddui, Y. Cui, J. Galvin, W. Chen, Y. Yu, and Y. Xiao. Characteristic of gafchromic xrqa2 films for kv image dose measurment. *Med. Phy.*, (39):842–50, 2012.

SJ. Glick. Breast ct. *Annu. Rev. Biomed. Eng.*, (9):501–526, 2007.

R. Gordon, R. Bender, and G. T. Herman. Algebraic reconstruction techniques (art) for three-dmensional electron microscopy and x-ray photography. *J. Theor. Biol.*, (29):471–81, 1970.

G.R. Hammerstein, D.W. Miller, D.R. White, M.E. Masterson, H.Q. Woodard, and J.S. Laughlin. Absorbed radiation dose in mammography. *Radiology*, (130):485–91, 1979.

S. Y. Huang, J. M. Boone, K. Yang, A. L. C. Kwan, and N. J. Pachard. The effect of skin thicnkess determined using breast ct on mammographic dosimetry. *Med. Phys.*, (35):1199–206, 2008.

J. H. Hubbell and S. M. Seltzer. Web site: http://www.nist.gov/pml/data/xraycoef/. 1993.

IAEA. *Status of computed tomography. Dosimetry for wide cone beam scanners*. IAEA Human Health Reports No 5 (Vienna: International Atomic Energy)(*www − pub.iaea.org/MTCD/Publications/PDF/Pub*1528*_web.pdf*), 2011.

IEC. *Amendment 1 to IEC 60601-2-44: 2009 Medical electrical equipment: part 2-44. Particular requirements for the basic safety and essentiell performance of x-ray equipment for computed tomography Committee Draft (CD) 62B/804/CD.* 2010.

S. Incerti and et al. The geant4-dna project. *Int. J. Model. Simul. Sci. Comput*, (1):157–78, 2010.

S. Incerti and et al. Web site: https://twiki.cern.ch/twiki/bin/view/geant4/lowephysicslists. 2014.

V.N. Ingal, E.A. Beliaevskaya, A.P. Brianskaya, and R.D. Merkurieva. Phase mammography: a new technique for breast investigation. *Phys. Med. Biol.*, (43(9)):2555–67, 1998.

P. C. Johns and M. J. Yaffe. X-ray characterization of normal and neoplastic breast tissues. *Phys. Med. Biol.*, (32):675–95, 1987.

A. C. Kak and M. Slaney. *Principles of Computerized Tomography Imaging*. IEEE Press, 1988.

W.A Kalender, M. Beister, J.M. Boone, D. Kolditz, and S.V. Vollmar. High-resolution spiral ct of the breast at very low dose: concept and feasibility consideration. *Eur. Radiol.*, (22):1–8, 2012.

W. A. Kalender. Dose in x-ray computed tomography. *Phys. Med. Biol.*, (59):129–50, 2014.

A. Katsuya and et al. Comparison of geant4 electromagnetic physics models against the nist reference data. *IEEE Trans. On Nucl. Science*, (52(4)):910–18, 2005.

R. N. Kulkarni and S. J. Supe. Radiation dose to the breast during mammography: a comprehensive, realistic monte carlo calculation. *Phys. Med. Biol.*, (29):1257–64, 1984.

N. Lanconelli, G. Mettivier, S. Lo Meo, and P. Russo. Investigation of the dose distribution for a cone beam ct system dedicated to breast imaging. *Physica Medica*, (29):1257–64, 2013.

R. Lewis. Medical applications of synchrotron radiation x-rays. *Phys. Med. Biol.*, (42):1213–43, 1997.

R. Longo and et al. Towards breast tomography with synchrotron radiation at elettra: first images. *Phys. Med. Biol.*, (61):1634–49, 2016.

R. Longo, M. Tonutti, L. Rigon, F. Arfelli, D. Dreossi, E. Quaia, F. Zanconati, E. Castelli, G. Tromba, and M.A. Cova. Clinical study in phase contrast mammography: image-quality analysis. *Phill. Trans. R. Soc.*, (372):2013005, 2014.

S. R. Mahdavi, A. D.Esmaeeli, M. Pouladian, A. S. Monfared, D. Sardari, and S. Bagheri. Breast dosimetry in transverse and longitudinal field mri-linac radiotherapy system. *Med. Phys.*, (42(2)):925–36, 2015.

M. Malvezzi, P. Bertuccio, F. Levi, C. La Vecchia, and E. Negri. European cancer mortality predictions for the year 2014. *Annals of Oncology*, (00):1–7, 2014.

E. Martella. Dosimetric characteristics of lif:mg,cu,p (gr-200a). *A.S.G. - Applicazioni Scientifiche Generali*.

L. Menegotti, A. Delana, and A. Martignano. Radiochromic film dosimetry with flatbed scanners: A fast and accurate method for dose calibration and uniformity correction with single film exposure. *Med. Phys.*, (35):3079–85, 2008.

G. Mettivier, C. Fedon, F. Di Lillo, R. Longo, A. Sarno, G. Tromba, and P. Russo. Glandular dose in breast computed tomography with synchrotron radiation. *Phys. Med. Biol.*, pages 569–87, 2016.

A. Mittone, A. Bravin, and P. Coan. Radiation dose in breast ct imaging with monochromatic x-rays: simulation study of the influence of energy, composition and thickness. *Phys. Med. Biol.*, (59):2199–2217, 2014.

M. Moscovitch and Y. S. Horowitz. Thermoluminescent materials for medical applications: Lif:mg,ti and lif:mg,cu,p. *Radiation Measurements*, (41):S71–S77, 2007.

M. E. Myronakis, M. Zvelebil, and D.G. Darambara. Normalized mean glandular dose computation from mammography using gate: a validation study. *Phys. Med. Biol.*, (58):2247–65, 2013.

R. Nowotny. Xmudat: photon attenuation data on pc. *IAEA-NDS-195*, 1998.

A. Okunade. Parameters and computer software for the evaluation of mass attenuation and mass energy-absorption coefficients for body tissues and substitutes. *J. Med. Phys*, pages 124–32, 2007.

S. Pacile and et al. X-ray phase-contrast imaging: from pre-clinical applications towards clinics. *Biomed. Opt. Express*, (6):3099, 2015.

D. Paganin, S. C. Mayo, T. E. Gureyev, and S. W. Wilkins. Simultaneous phase and amplitude extraction from a single defocused image of a homogeneous object. *J. Micros.*, (206):33–40, 2002.

S. Pani and et al. Breast tomography with synchrotron radiation: preliminary results. *Phys. Med. Biol.*, (49):1739–40, 2004.

D. J. Peet and M. D. Pryor. Evaluation of a mosfet radiation sensor for the measurment of entrance surface dose in diagnostic radiology. *Br. J. Radiol.*, (72):562–568, 1999.

E.D. Pisano and et al. Human breast cancer specimens: diffraction-enhanced imaging with histologic correlation improved conspicuity of lesion detail compared with digital radiography. *Radiology*, (214(3)):895–901, 2000.

N.D. Prionas, K.K. Lindfors, S. Ray, S.Y. Huang, L.A. Beckett, W.L. Monsky, and J.M. Boone. Contrast-enhanced dedicated breast ct: initial clinical experience. *Radiology*, (256(3)):714–23, 2010.

E. Quai, R. Longo, F. Zanconati, G. Jaconelli, M. Tonutti, A. Abrami, F. Arfelli, D. Dreossi, G. Tromba, and M.A. Cova. First application of computed radiology to mammography with synchrotron radiation. *Radiol. Med.*, (118(1)):89–100, 2013.

R. Ramani, S. Russell, and P. O'Brien. Clinical dosimetry using mosfets. *Int. J. Radiat. Oncol. Biol. Phys.*, (37 (4)):959–64, 1997.

L. Rigon and et al. Breast computed tomography with the picasso detector: a feasibility study. *NIM A*, (628):419–22, 2011.

A. B. Rosenfeld, M. G. Carolan, G. I. Kaplan, B. J. Allen, and V. I. Khivrich. Mosfet dosimeters: role of encapsulation in mixed gamma-neutron and megavolatage x-ray fields. *IEEE Trans. Nucl. Sci*, (42 (6)):1870–77, 1995.

P. Scalchi and P. Francescon. Calibration of a mosfet detection system for 6-mv invivo dosimetry. *Health Phys.*, (40):987–94, 1998.

I. Sechopoulos, S. Suryanarayanan, S. Vedantham, C. D,ÄôOrsi, and A. Karellas. Computation of the glandular radiation dose in digital tomosynthesis of the breast. *Med. Phys.*, (34):221–32, 2006.

I. Sechopoulos, S. Si Jia Feng, and J. C. D,ÄôOrsi. Dosimetric characterization of a dedicated breast computed tomography clinical prototype. *Med. Phys.*, (37):4110–20, 2010.

I. Sechopoulos. A review of breast tomosynthesis. part i. the image acquisition process. *Med. Phys.*, (40):014301–014312, 2013.

I. Sechopoulos. A review of breast tomosynthesis. part ii. image reconstruction, processing and analysis, and advanced application. *Med. Phys.*, (40):014302–014317, 2013.

L. Shi, S. Vedantham, A. Karellas, and A. M. O' Connel. Thecnical note: skin thickness measurements using high-resolution falt-panel cone-beam dedicated ct. *Med. Phys.*, (40):031913, 2013.

T. B. Shope, R. M. Gagne, and G. C. Johnson. A method for describing the doses delivered by transmission x-ray computed tomography. *Med. Phys.*, (8):488–95, 1981.

R. Siegel, J. Ma, Z. Zou, and A. Jemal. Cancer statistic 2014. *Cancer J. Clin.*, (64):9–29, 2014.

P. Skaane and et al. Comparison of digital mammography alone and digital mammography plus tomosynthesis in a population-based screening programm. *Radiology.*, (267(1)):47–56, 2013.

A. Snigirev, I. Snigireva, V. Kohn, S. Kuznetsov, and I. Schelokov. On the possibilities of x-ray phase contrast microimaging by coherent high-energy synchrotron radiation. *Rev. Sci. Instrum.*, (66(12)):5486–92, 1995.

K. Taguchi and J. S. Iwanczyk. Vision 20/20: Single photon counting x-ray detectors in medical imaging. *Med. Phys*, (40):100901–19, 2013.

T. Takahashi and S. Watanabe. Recent progress in cdte and cdznte detectors. *Nuclear Science, IEEE Transactions*, (48 (4)):950–59, 2001.

T. Takeda, A. Momose, E. Ueno, and Y. Itai. Phase-contrast x-ray ct image of breast tumor. *J. Synchrotron Radiat.*, (5(Pt 3)):1133–35, 1998.

S. C. Thacker and S. J. Glick. Normalized glandular dose (dgn) coefficients for flat-panel ct breast imaging. *Phys. Med. Biol.*, (58):7921–36, 2004.

N. Tomic, S. Devic, F. DeBlois, and J. Seuntjens. Reference radiochromic film dosimetry in kilovoltage photon beams during cbct image acquisition. *Med. Phy.*, (37):1083–92, 2010.

N. Tomic, C. Quintero, B. R. Whiting, S. Aldelaijan, H. Bekerat, L. Liang, F. DeBlois, J. Seuntjens, and S. Devic. Characterization of calibration curves and energy dependence gafchromictm xr-qa2 model based radiochromic film dosimetry system. *Med. Phy.*, (41):062105–1 062105–9, 2014.

M. Tominaga, Y. Kawata, N. Niki, N. Moriyama, K. Yamada, J. Ueno, and H. Nishitani. Measurements of multidetector ct surface dose distributions using a film dosimeter ad chest phantom. *Med. Phy.*, (38):2467–78, 2011.

A. van der Sluis and H. A. van der Vorst. Simulaneous algebraic reconstruction technique (sart): A superior implementation of the art algorithm. *Ultrasonic Imaging*, (6):81–94, 1984.

A. van der Sluis and H. A. van der Vorst. Sirt and cg-type methods for the iterative solution of sparse linear least-square problems. *Linear Algebra and its applications*, (130):257–302, 1990.

S. Vedantham, L. Shi, A. Karellas, A.M. O'Connell, and D.L. Conover. Personalized estimates of radiation dose from dedicated breast ct in a diagnostic population and comparison with diagnostic mammography. *Phy. Med. Biol.*, (58(22)):7921–36, 2013.

A. Vincenzi, P. L. De Ruvo, P. Delogu, R. Bellazzini, A. Brez, M. Minuti, M. Pinchera, and G. Spandre. Energy characterization of pixirad-1 photon counting detector system. *J. Instrum*, (10):C04010, 2015.

B. Wang, X. X. George, and K. Chan-Hyeong. Monte carlo study of mosfet dosimeter characteristics: dose dependence on photon energy, direction and dosimeter composition. *Rad. Prot. Dos.*, (113 (1)):40–46, 2005.

S. A. White, G. Landry, G. P. Fonseca, R. Holt, T. Rusch, L. Beaulieu, F. Verhaegen, and B. Reniers. Comparison of tg-43 and tg-186 in breast irradiation using a low energy electronic brachytherapy. *Med. Phy.*, (41(6)):061701, 2014.

L. Wilkinson and J. Heggie. Glandular breast dose: potential errors. *Radiology*, (213):1, 2001.

X. Wu, E.L. Gingold, G.T. Barnes, and D.M. Tucker. Spectral dependence of glandular tissue dose in screen-film mammography. *Radiology*, (179):143–8, 1991.

X. Wu, E.L. Gingold, G.T. Barnes, and D.M. Tucker. Normalized average glandular dose in molybdenum target-rhodium filter and rhodium target-rhodium filter mammography. *Radiology*, (193(1)):83–89, 1994.

M. J. Yaffe, J. M. Boone, N. Packard, O. Alonzo-Proulx, S. Y. Huang, C. L. Peressotti, A. Al-Mayah, and K. Brock. The myth of the 50-50 breast. *Med. Phys.*, (36(12)):5437–43, 2009.

Y. Zhao and et al. High-resolution, low dose phase contrast x-ray tomography for 3d diagnosis of human breast cancers. *PNAS*, (109(45)):18290–4, 2012.

B. Zhao, X. Zhang, W. Cai, and D. Conover et R. Ning. Cone beam breast ct with multiplanar and three dimensional visualitation in differentiating breast masses compared with mammography. *Eur. J. Radiol.*, (84(1)):48–53, 2015.